INFLUENCE OF ELASTIC MISMATCH AND NATURE OF INTERFACIAL BONDING ON TOUGHNESS OF PARTICULATE COMPOSITES

by

ARUP K. KHAUND, B.Sc. (Gauhati), M.Sc. (Saskatchewan)

A Thesis

Submitted to the School of Graduate Studies

In Partial Fulfilment of the Requirements

For the Degree of

MASTER OF ENGINEERING.

McMaster University, Hamilton, Ontario.

May 1978

INFLUENCE OF ELASTIC MISMATCH AND NATURE OF INTERFACIAL BONDING ON TOUGHNESS OF PARTICULATE COMPOSITES

MASTER OF ENGINEERING (1978) McMASTER UNIVERSITY
(Metallurgy and Materials Science) Hamilton, Ontario

TITLE: Influence of Elastic Mismatch and Nature of Interfacial Bonding on Toughness of Particulate Composites

AUTHOR: Arup K. Khaund,

B.Sc. (Gauhati),

M.Sc. (Saskatchewan)

SUPERVISOR: Dr. P. S. Nicholson

NUMBER OF PAGES:

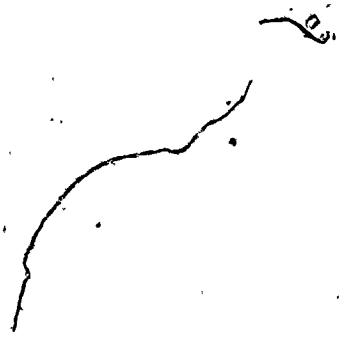

ABSTRACT

This work involves the study of crack-particle interaction in model brittle particulate composites where,

i) the interfacial bonding strength between second phase and matrix was continuously varied (glass - partly oxidized Ni system) and

ii) the presence and absence of elastic mismatch between second phase and matrix which gives rise to stress concentration around the particle was monitored. An ultrasonic fracture surface modulation technique was used which imprints the details of local crack-particle interaction on fracture surface.

The important results of this study are:

i) Both the interfacial strength and elastic mismatch play important roles in improving the toughness of a particulate composite; optimum bond strength alone; without consideration of elastic mismatch may not improve toughness of a composite by a significant amount.

ii) For optimum toughening, second phase particles with a high intrinsic toughness which are well-bonded to the matrix and whose elastic moduli are equal to or less than that of matrix should be used.

iii) Due to the presence of elastic stress concentration, for second phase particles whose elastic moduli exceeds that

of the matrix, a rather weak interfacial bonding is preferred to a strong interfacial bonding for effective crack particle interaction which will improve the toughness of a composite.

In summary, this work provides some guidelines for choice of proper second phase particles and matrix in the design of brittle particulate composites for optimum toughness.

ACKNOWLEDGMENTS

I express my thanks to my supervisor Dr. P. S. Nicholson for his continued interest in this work and those members of the faculty who offered constructive criticisms from time to time during the period of this work. My sincere acknowledgment to my colleague Mr. V. D. Krstic with whom I had countless discussions to clear our understandings of fracture mechanical behaviour of brittle materials.

LIST OF FIGURES

TABLE OF CONTENTS

CHAPTER I

INTRODUCTION

1.1 Importance of Composite Brittle Materials:

It has long been recognized that highly brittle ceramic materials possess many attractive properties such as hardness, chemical inertness, low thermal and electrical conductivity and high temperature stability. The serious drawback of these materials is their proneness to catastrophic failure under thermal shock and mechanical impact. The addition of a second phase influences the resistance to crack propagation (or toughness) of the ceramic. The following treatment shows that the production of tough ceramics may not be possible from single phase homogeneous materials but may follow from the development of multiphase composites.

According to Griffith [1], the energy balance for fracture of an ideal homogeneous brittle material containing an elliptical flow of major axis 2a, perpendicular to a uniform tensile field can be represented by the curve shown in Figure 1 (from [2]). The energy demand curve is a straight line represented by $W_d = 4a\gamma$ where γ is the surface energy. The energy release curve is a second power parabola given by $W_r = \frac{\gamma\sigma^2 a^2}{E}$ where E is the Young's modulus

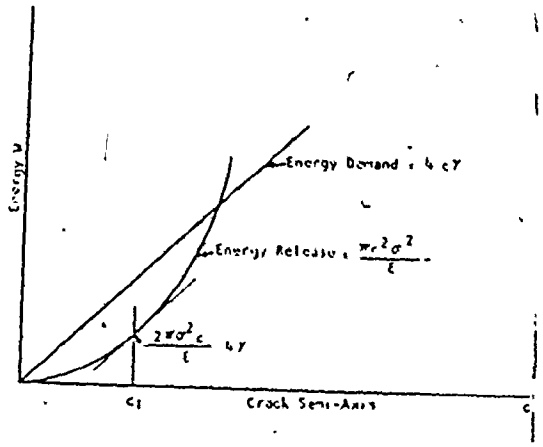

Figure 1: Crack Propagation in Ideal Griffith Material

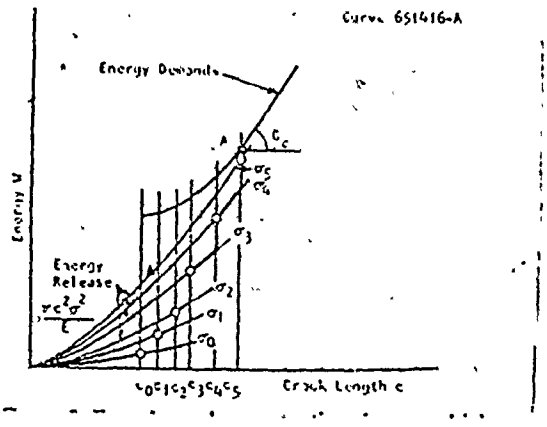

Figure 2: Schematic of Crack Propagation Behaviour in Multiphase Material (after 3)

of the material. Crack instability occurs when the slopes of the two curves are equal i.e.

$$\frac{\delta W_r}{\delta a} = \frac{\delta W_d}{\delta a} \qquad (1)$$

The implication of Equation 1 for an ideal Griffith material is that the 'instability' (propagation) is assured in advance, once the crack is initiated. The instability is thus 'built-in' in Griffith's criteria of brittle fracture. In a single phase homogeneous brittle material, since the energy demand is the same everywhere, the initiation and propagation of a crack therefore coincide and fracture is instantaneous, as in glass. In the development of 'tough ceramics' the objective is to promote a stage of stable crack propagation. This is denied to a single phase homogeneous brittle material irrespective of its strength [2]. The situation is different, however, for multiphase materials. When crack arrestors (which includes any second phase material) are present in a brittle matrix the energy demand curve is nonlinear [3] in contrast to the linear demand curve for the Griffith material. In multiphase ceramics there is a distinct division in energy demand between the various phases, so the stages of initiation and propagation are separate. A crack may exist in the weaker phase and whilst propagating may encounter a zone of tougher 'second phase'. To clear this obstacle, the crack

must cut through or detour around. In either case, the energy demand will increase and the propagation may be halted unless there is an increment in the "operating stress". Following the above concept Gluklich [3] proposed that the energy demand curve for a heterogeneous material is nonlinear in contrast to a linear curve for the homogeneous material, as shown in Figure 1(b). The nonlinerity arises from the ability of the secondary phase to stabilize a growing crack by requiring more energy to "clear" the obstacle. Figure 1(b) represents a highly idealized case of a tailored brittle material where the crack as it grows encounters an increasingly tougher medium. Crack propagation in real multiphase ceramic materials may differ in detail, but the overall crack growth mechanism will be similar to that illustrated in Figure 1(b).

It has long been recognized, [4, 5] that second phase inclusions (or pores) of different elastic moduli and thermal expansivity than the matrix give rise to local stress concentrations in a particulate composite. Also interfacial property differences between the second phase and matrix influence to a great extent the fracture mechanical properties of particulate composites [6, 7]. However no consistent and detailed study has been made of local crack-particle interactions and their influence on the overall toughening of the composite. It is the intention of this work to

study in detail such interactions when elastic mismatch exists between the inclusion and matrix and also when the interfacial bond strength between the inclusion and the matrix is continuously varied. Model particulate systems were chosen for this study i.e.

i) glass with partly oxidized Ni particles. (The elastic mismatch between glass and Ni is significant). The oxidation time of the Ni is varied to produce different NiO thicknesses and therefore varied interfacial bonding strength between the matrix and inclusion, and

ii) glass with partly oxidized aluminum spheres. In this case strong bonding exists and no elastic mismatch.

1.1.2 Definition of Basic Fracture Mechanical Parameters

The basic concepts and important parameters of fracture mechanics will now be summarized for reference in later chapters.

i) For an ideal brittle material (assuming no plastic deformation prior to fracture), the Griffith criteria [1] for unstable crack propagation is:

$$\sigma_a \geq \sigma_f = \sqrt{\frac{2E\gamma}{\pi a}} \qquad (2)$$

where σ_a is the applied stress, σ_f is the fracture stress, E the Young's modulus, 2a the crack length in the material and γ the surface energy per unit area of separated surface. The Griffith analysis is valid for Mode I type fracture where a tensile load is applied orthogonally to the plane of the crack. The Mode I type fracture test is the most common one. The Griffith expression is the outcome of an energy balance only and does not take into account the nature of the crack tip stress field.

ii) The stress intensity factor K_I (for Mode I) relates the applied stress to the stress concentration at the crack tip. For Mode I type fracture [8]

$$K_I = \sigma_a (Ya)^{1/2} \qquad (3a)$$

where Y is a geometrical factor dependant on the test geometry; $Y = \pi$ for uniaxial tension.

When a critical stress level K_{IC} is reached, unstable crack propagation will occur and catastrophic failure follows. The concept of a 'critical stress intensity factor' is the basis of the fracture toughness approach [8] to evaluating materials and can be taken as an intrinsic parameter of a material. For Mode I type fracture the following important relation holds:

$$K_{IC}^2 = EG_{IC} = 2E\gamma_I \qquad (3b)$$

where $G_{IC} \equiv$ critical strain energy release rate at unstable

propagation of existing flaws in the material and is termed the "fracture-toughness" of the material, γ_I is the effective surface energy which, apart from the thermodynamic surface energy, takes into account all irreversibly dissipated energy (including plastic deformation) at the crack tip. Obviously from (3)

$$G_{IC} = 2\gamma_I \tag{4}$$

Hence, the concept of modern fracture mechanics developed by Irwin can be interconnected with Griffith's original formulation through equations 3(a), 3(b) and (4).

When $K_I < K_{IC}$, stable crack growth may occur. The rate of crack growth is in turn, influenced by the microstructure or second phases present in the path of the crack front. A study of the crack-front velocity and crack front shape will yield useful information on the influence of second phase (or microstructure) on the overall toughening of particulate composites.

iii) For Mode I type fracture in brittle materials, the components of the stress field at a point (r, θ) near the crack tip are given by the continuum approach of linear elastic fracture mechanics [8], i.e.

$$\sigma_{xx} = \frac{K_I}{\sqrt{2\pi r}} \cos\frac{\theta}{2}\left[1 - \sin\frac{\theta}{2}\sin\frac{3\theta}{2}\right]$$

$$\sigma_{yy} = \frac{K_I}{\sqrt{2\pi r}} \cos\frac{\theta}{2}\left[1 + \sin\frac{\theta}{2}\sin\frac{3\theta}{2}\right].$$

$$\sigma_{xy} = \frac{K_I}{\sqrt{2\pi r}} \cos\frac{\theta}{2} \cos\frac{3\theta}{2} \sin\frac{\theta}{2} \qquad (5)$$

The component σ_{yy} is the crack driving stress and σ_{xx} is parallel to the crack-front. $\sigma_{xy} = 0$ at $\theta = 0$. The variation of these stress fields in front of an elliptical hole (which becomes a sharp crack as the radius of curvature goes to zero) along $\theta' = 0$, are shown in Figure 3.

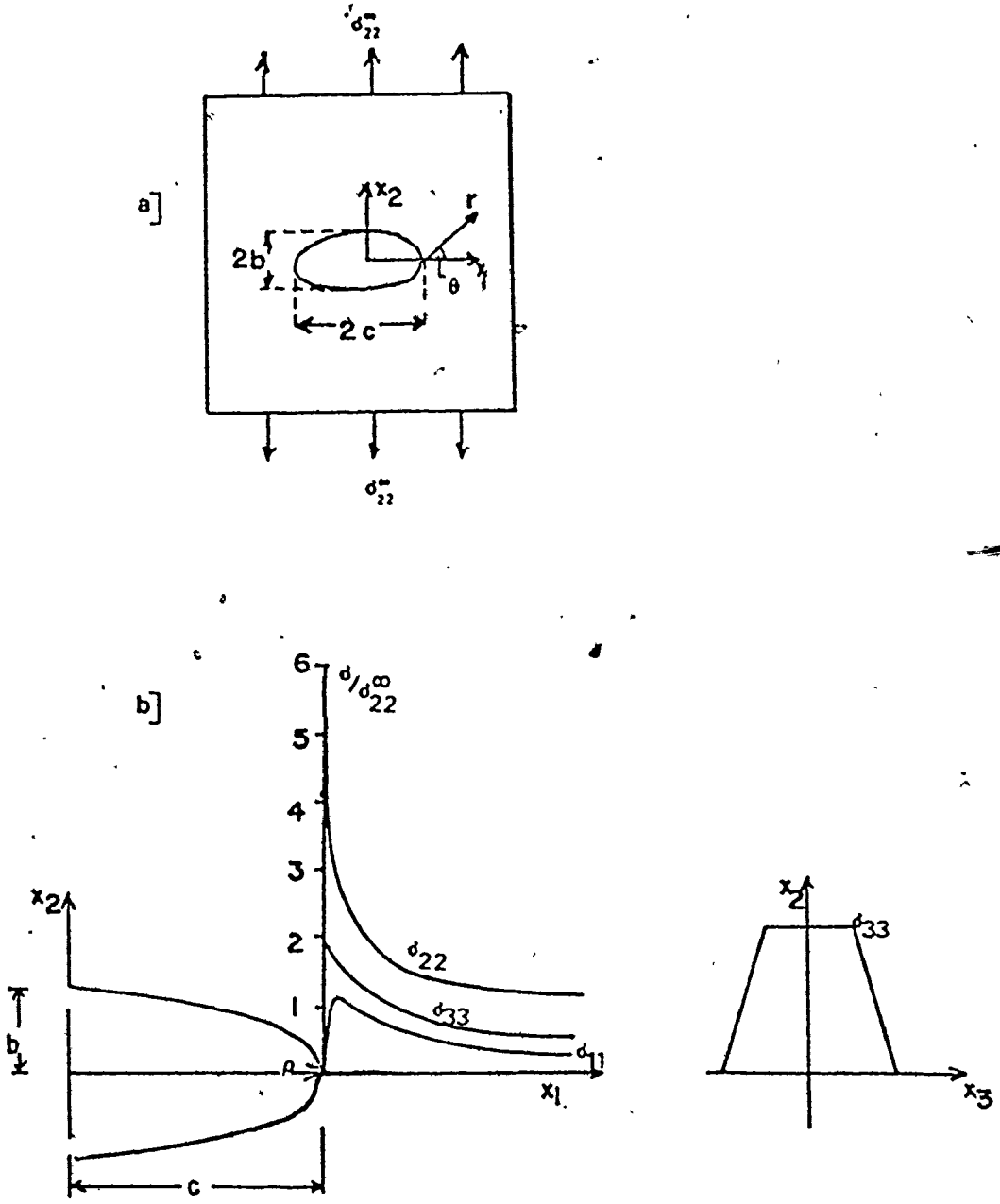

Figure 3. Variation of $\sigma_{22}(=\sigma_{yy})$ and $\sigma_{33}(=\sigma_{zz})$ in front of an elliptical hole (the behaviour of the stress component of a sharp crack is also similar to this kind of variation. This is the limiting case when radius of curvature approaches zero).

CHAPTER II

LITERATURE REVIEW

2.1 Energy Absorbing Processes in the Fracture of Brittle Materials

2.1.1 General Discussion:

For well developed cracks in highly brittle materials, such as covalent and some ionic-covalent solids at ambient temperatures, fracture will occur by bond rupture at an atomically sharp crack tip. The elastic stress field should describe the situation well though modification must be applied to account for any microstructural interactions. Defects such as dislocations are expected to be immobile. It is necessary to account for the energy expenditure in such systems in terms of the interaction of the crack tip stress field and the microstructural features. Such an understanding allows the characteristic fracture parameter of a material to be determined but more importantly it may suggest techniques to control the toughness by microstructural design. There are several energy absorbing processes in the fracture of brittle materials (apart from the expenditure of thermodynamic equilibrium surface energy in creation of new surface area) and these will now be discussed.[9]

i) Surface Roughness:

In many materials crack propagation does not proceed in a planar fashion. For example, in polycrystals the crack may tilt and twist as it follows the cleavage planes for transgranular failure. In particulate composites, the stress field around the particles may alter the crack path and lead to surface roughness. In absolute terms the increase in fracture resistance should be related to the increase in surface area [10].

Grain boundaries and other interfacial defects constitute locations of relative weakness in a polycrystal. This is particularly true in ceramic materials where the directionality and charge requirements of covalent-ionic bonds can lead to substantial reduction in interfacial cohesion. Such interfacial weakness may be further emphasized by the presence of internal stresses due to elastic mismatch between phases [11], phase transformations [12] or anisotropic thermal expansions [13]. Cracks tend to propagate along these interfaces. In a particulate composite there is a tendency for decohesion of the particles [12, 13]. Intergranular fracture is often characterized by a zig-zag crack path leading to greater variations in fracture energy than expected for transgranular failure. For intergranular failure, the fracture energy may be written (after Gilman) as [14]

$$2\gamma_{eff} = 2\gamma - \gamma_i \qquad (6)$$

where γ_i is the reversible interface energy and γ_{eff} the effective fracture energy. In ceramics γ_i values are usually high due to unsatisfied covalent or ionic bonds. Hence γ_{eff} is usually low. In polycrystalline ceramics, cracks usually propagate through the grain boundaries. A series of experiments by Class and Machlin [15] on KCl bicrystals clearly demonstrated the weakening effect of grain boundaries. However, though the grain boundaries may be inherently weak in highly brittle materials, the abrupt changes in crack path at each grain will lead to a substantial reduction in the local mechanical energy release rate and hence the zig-zag nature of the crack path will apparently increase the fracture surface energy. This problem may be accentuated at larger grain sizes for then a crack approaching an interface may lead to its decohesion. This problem has been discussed by Cook and Gordon [16] for the special case of an interface at right angles to a crack. Such a crack is locally blunted and the local stress distribution changed. Further propagation of such a crack requires an increase in stored energy before the sufficient criterion for failure is reached. It is clear from the above discussion that crack propagation in polycrystalline materials is a complex process involving a number of microscopic events. In particulate composites, the equivalent surface roughening process for the dissipation of mechanical energy could be the local plastic deformation of particles (ahead of the

crack tip) weaker than the breaking strength of surrounding matrix. In this case the bonding strength between the second phase and the matrix must be equal to or greater than the matrix strength.

ii) Microcrack Zones:

If weak interfaces exist in sufficient density within a single phase (grain boundaries) or a multiphase material, it is conceivable that the region ahead of a well-developed crack may consist of a decohesed zone. This will increase the fracture toughness of the material if the fracture area associated with such a zone is large. Furthermore its existence should lead to a period of slow stable crack growth as this zone develops. There is evidence of such behaviour in many brittle materials.

In polymers the production of a "crazed" zone is a related mechanism. In concrete, the formation of discrete cracks ahead of the primary crack has been observed [17]. In a study of the fracture of rocks, Rosenfield et. al [18] observed such behaviour and pointed out that the energy dissipated in the fracture of rocks is associated with the creation of a large amount of surface area. In ceramic materials, similar behaviour was observed in the calcia partially stabilized zirconia [19, 20] system. In this case the weakness was proposed to occur at the grain boun-

aries as a result of the phase transformation of pure ZrO_2 precipitated there. Anisotropic thermal expansion in some ceramics also leads to microcrack formation [21, 22]. More recently Claussen et. al [23, 24] have used this idea to design 'tougher' microstructures where effective use can be made of microcrack formation.

The formation of a large microcrack zone is unlikely in a glass-particulate composite; however, an equivalent mechanism of decohesion, namely that of weakly bonded particles, may be identified as an important energy absorbing mechanism for such composites. In particulate composites, the interface between the particles and the matrix may be a source of weakness when decohesion takes place. This is discussed in section 2.1.2.

iii) Crack Blunting:

A crack front will be locally blunted when it intersects pores, weak interfaces, grain boundaries etc. Such a process will alter the local stress distributions ahead of the crack. Berry [25] showed that, in terms of an energy criterion, the value of the critical applied stress changes by only 1% for most cases. However in terms of a limiting stress concept we have [26]

$$\sigma_f = \sigma_g \, (r/3a_o)^{1/2} \qquad (7)$$

where σ_g is the fracture stress in the absence of a pore of

radius r and a_o is the atomic radius. Using a value of $r \sim 3 \times 10^4 a_o$, $\sigma_f = 100 \sigma_g$ results, and hence a much higher stress must be applied to the body, leading to a higher value of the critical stress intensity factor. Hence the energy criterion of Berry [25] is insufficient to indicate the effect of pores, grain boundaries and weak interfaces in blunting an approaching crack.

2.1.2 Particulate Composites

For a simple model system where particles are dispersed in a glass matrix, several workers [27, 28, 29, 30] have observed that the effective fracture energy of the system is increased over that of glass. Several mechanisms could be involved with this increase in toughness. The energy dissipative mechanisms which may be opepative in these particulate systems are now summarized.

i) Particle Decohesion and Crack Blunting:

In a particulate composite, the interface between the particles and the matrix may be a source of weakness. Hence the stress component σ_{yy} ahead of the crack front may decohese such weak interfaces, and relieve some of its strain energy in doing so. Further, once the crack front meets the "decohesed-zone", blunting occurs and, as described in section 2.1.1, a higher operating stress is

necessary to extend the crackfront further.

The size of the decohesed zone can be estimated [9] assuming that the interface will fail when the stress normal to the interface exceeds a critical value. For the decohesion of spherical obstacles, there should always be part of the interface that is subject to the maximum normal stress so that all the particles within the zone should decohese to some extent. This approach assumes the particles are small compared to the zone size. It is also possible to estimate the effect of such a zone on the fracture energy. From a mechanistic viewpoint, the contribution to fracture surface energy of zone formation is [9]

$$\gamma_{zone} \simeq \frac{1}{2} N_A A_{TC}(\sigma_T a_o) \tag{8}$$

where, for the two dimensional case, A_{TC} is the area of the critical decohesed zone, N_A the number of particles per unit area, σ_T the critical stress needed to decohese the interfaces and a_o the interatomic distance. For a random distribution of uniform spheres of radius r, [31]

$$N_A = \frac{3V_v}{2\pi r^2} \tag{9}$$

where V_v is the volume fraction of particles.

From the treatment of the formation of microcracks in a ceramic matrix by Hoagland et. al. [32],

$$A_{TC} = 1.12\left(\frac{K_{IC}}{\sigma_T}\right)^4 \tag{10}$$

The variation of $\sigma_T(\theta)$ needed to break an interface and the variation of stress $\sigma(\theta)$ around a point for a weakly bonded inclusion are shown in Figures 4(a), 4(b) [9] for the case when the interface failed and also for the case where the interface remains intact.

Using Equations (10) and (9) in (8), it follows that,

$$\gamma_{zone} = .84 \frac{K_{IC}^4 a_o}{\pi \sigma_T^3} \left(\frac{V_v}{r^2}\right) \qquad (11)$$

It is obvious from Equation (11) that contributions from decohesed zones could be substantial for low values of σ_T as $\gamma_{zone} \propto \frac{1}{\sigma_T^3}$. The value of σ_T is difficult to determine experimentally but the form of Equation (11) is of importance. Hence, apart from completely nonbonded composites for which Equation (11) is not valid, the equation shows that for constant r and V_v, the contribution of the decohesed zone will be a maximum for the weakest interface. This concept will be tested in the present work for a glass/partly-oxidised-Ni composite where the oxidation time of the Ni particles is varied from 0 to 120 minutes in steps of 30 minu tes. The assumption made in this case is that the increasing thickness of oxide layer on the Ni increases the interfacial bond strength between the glass matrix and the particles. That this is the case was shown by Stett and Fulrath [11].

From this discussion it is clear that the formation

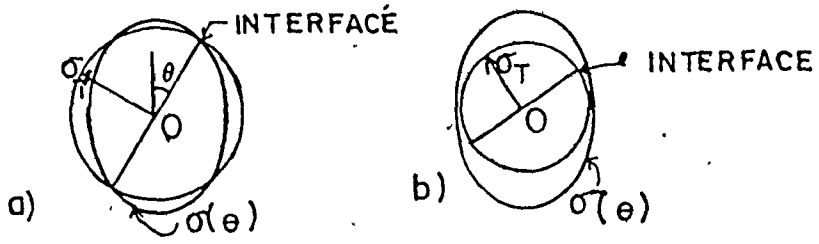

Figure 4(a) Schematic Representation of Stress Variation around a Point $O(\sigma(\theta))$ and the Stress Needed to Break an Interface (σ_T) that lies at an Angle θ to the Applied Stress. a) Interface Not Failed b) Interface Failed.

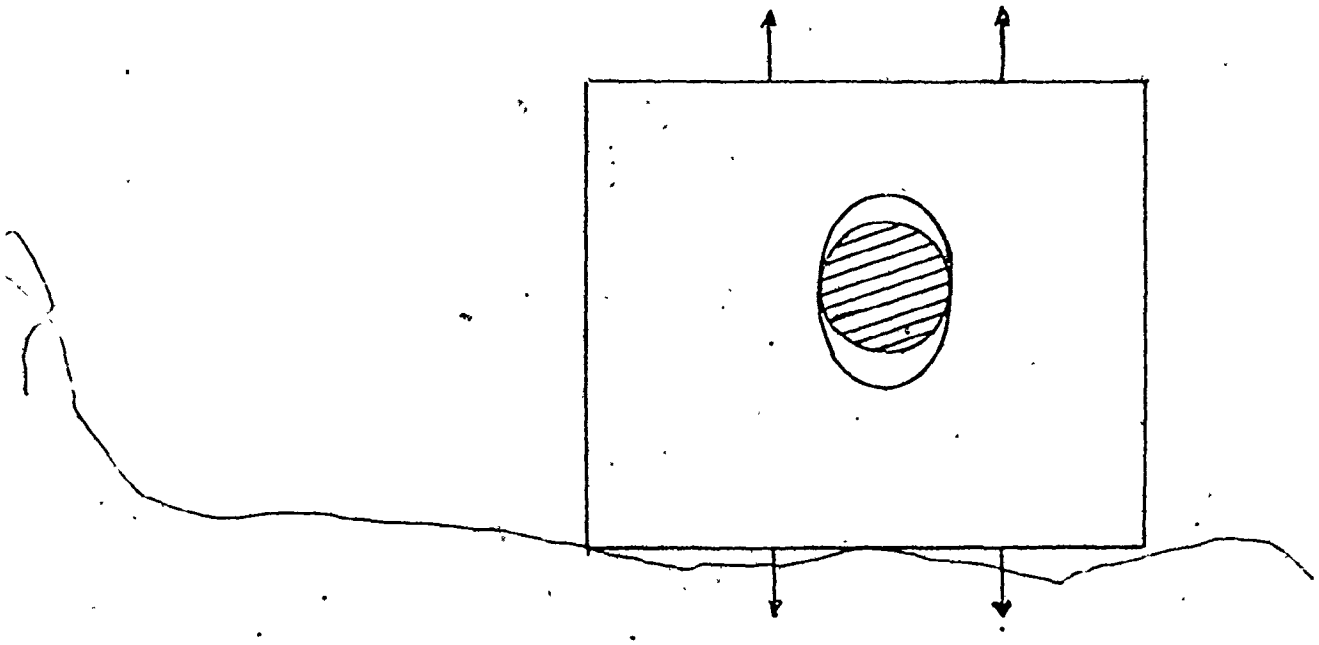

Figure 4(b) Formation of Pseudovoids around Non-bonded or Weakly-bonded Second Phase Particles in a Body Under Tension.

of weak bonding between particles matrix and hence a decohesed zone in front of a crack tip in brittle materials could be a useful way to increase the toughness of the material. It must be pointed out however, that this is likely to lead to a decrease in strength as weak interfaces will act as sites for crack nucleation.

ii) Crack Front Shape Changes in the Vicinity of Inclusions

There is substantial fractographic evidence in the literature [33, 34, 35] that indicate a tendency for a crack front to change shape as it approaches a second phase particle. The shape change may be the result of an increase in the elastic strain energy of the body as the crack circumvents the particle, especially if the particles act to momentarily pin the crack front. This interaction was first conceived by Lange [36] to explain increases in the fracture energy of glass-Al_2O_3 composites [35]. He proposed that the increase in crack length as the crack front changes shape, could contribute significantly to the fracture energy of a brittle, dispersed-phase composite. Lange's model is shown in Figure 5(a) wherein a portion of a crack front is shown to intersect a linear array of equally spaced pinning positions. Prior to stressing (and also whilst the crack is approaching the

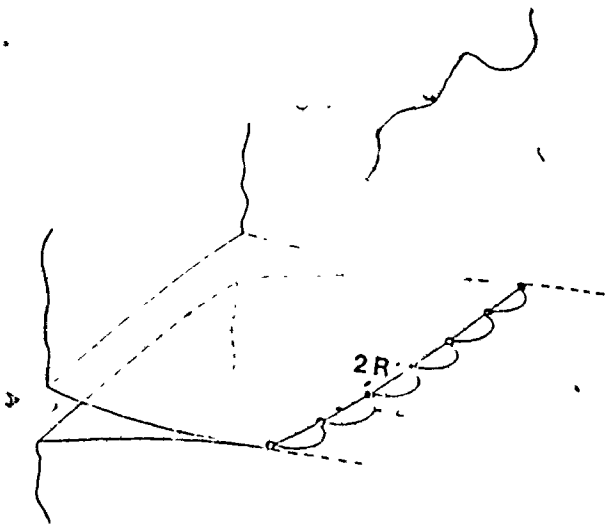

Figure 5(a) Model used by Lange to represent the interaction of a crack with a linear array of dispersed, dimensionless inhomogeneities equally spaced by a distance 2R. The straight line illustrates the crack front prior to stressing. The bowed position shows the situation just prior to breakaway and fracture.

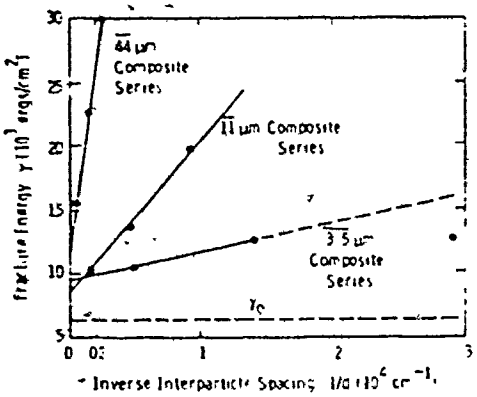

Figure 5(b) Fracture surface energy versus the inverse of mean free path for a sodium borosilicate glass containing 3 size dispersions (3.5, 11, & 44μm) of Al_2O_3. γ_o is the fracture surface energy of the glass without the dispersed phase.

obstacle), it was assumed that the crack front is straight. As the applied stress increases the crack front bows between the particles and so increases its length. Hypothesising the existence of a "line-energy", the increase in length can be related to an increase in elastic strain energy. Based on the assumption that the pinning positions are dimensionless points and that breakaway occurs when the crack front is semicircular, Lange [36] geometrically derived the following expression for the effective fracture energy of the composite

$$\gamma_{eff} = \gamma_0 + T/d \qquad (12)$$

where T is the crack line energy per unit length, d the interparticle spacing and γ_0 the fracture energy of the pure matrix. To determine the validity of his model Lange [35] investigated the fracture energy of glass-Al_2O_3 composites and his results are shown in Figure 5(b) for three different size dispersions. Though the experimental results verify the 1/d relationship, they also indicate that the increase in fracture energy depends on the particle size. This was not predicted by the original model. To overcome this difficulty Lange further postulated that the size of the particle may control its pinning ability. A value for line energy per unit length, T, was estimated by dividing the elastic strain energy associated

with a semicircular crack by its length:

$$T = \frac{2}{3\gamma_o d} \qquad (13)$$

The Lange Model suffers the following limitations:

i) the concept of associating the increased strain energy due to the crack with its peripheral length may be reasonable for a dislocation with its $\frac{1}{r}$ - dependent stress field but for a crack front stress field with a $(\frac{1}{r})^{\frac{1}{2}}$ dependence, it is not clear that integration results in a unique line tension. In a recent review, Thomson [37] points this out and states that the tension will depend critically on the crack shape. Therefore, although the line tension concept has been successful in modelling a pinned dislocation, an analogous treatment for a pinned crack may not be suitable.

ii) the effect of the stress field of the particle is ignored as also are any changes of crack shape as a result of this interaction. There is evidence that a crack changes its shape as it approaches a particle (Figure 4 and 5). The reason for this change is the elastic mismatch between the inclusion and matrix. This will be discussed in detail in Chapter III.

iii) the particles themselves must make some contribution to the fracture resistance and the mechanism of particle cleavage or interfacial decohesion must be included

to understand the fracture process in such composites. The problem of particle decohesion is often overlooked and it may be that for many systems, the crack front is intersecting a decohesed particle (i.e., a void) rather than well-bonded second phase particles. It was emphasized earlier that in many brittle systems, the interface between the particle and matrix can be a source of inherent weakness. Further, there will be a tendency for a crack front to avoid well-bonded particles of higher elastic modulus than the matrix due to the location of elastic stress concentrations, as discussed in Chapter III. Lange also ignores the problem of crack path.

Evans [38] modified Lange's treatment, taking a fracture mechanical approach to the problem. He relaxed the following assumptions implicit in Lange's treatment; (a) no interaction of the stress fields between different line segments 'bowing' between pairs of obstacles, (b) the line energy per unit length of the crackfront T is assumed to be constant and independent of the shape of the crackfront and (c) the maximum stress position for 'breakaway' is always at the 'semi-circular' condition of the crackfront. Evans [38] computed the elastic stored energy associated with different crack shape configurations and in particular compared the stress to move secondary cracks between the obstacles σ_A with that to move the primary crack in the

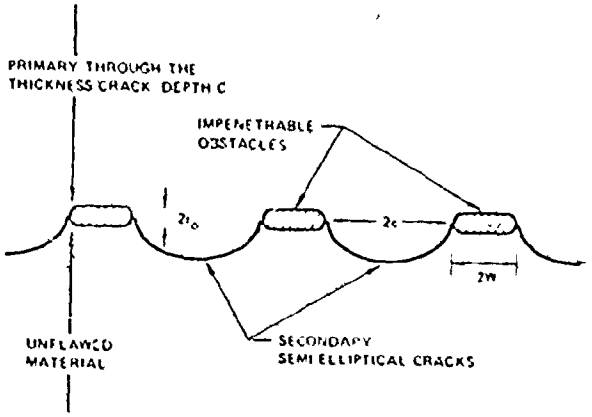

Figure 6(a) Model used by Evans to represent interaction of crack front with a linear array of impenetrable obstacles by considering the motion of secondary semi-elliptical flows in the stress field of the primary crack.

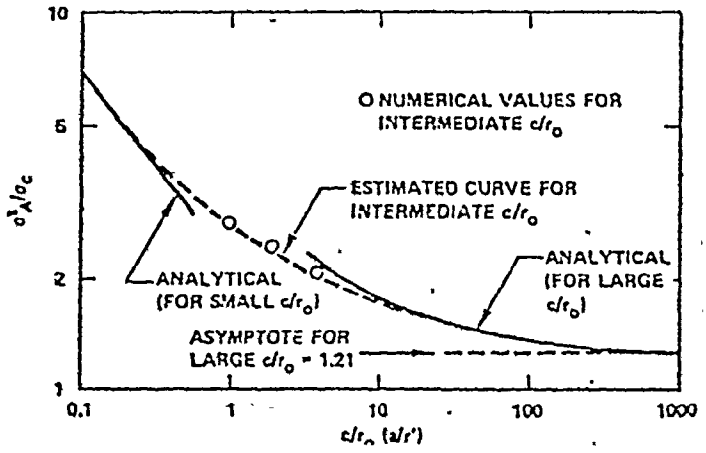

Figure 6(b) Plot of $\frac{\sigma_A}{\sigma_c}$ against c/r_o (after Evans(14)).

absence of obstacles σ_C [Figure 6(a)]. The significant conclusions of Evan's model pertinent to the present study are:

i) the ratio σ_A/σ_C is not constant but depends critically on the crack front shape at breakaway, Figure 6(b). Obviously the higher is the curvature of the crack-front, i.e. the larger is the angle of bowing, the higher is the ratio σ_A/σ_C i.e. the higher is the resistance to crack propagation.

ii) the shape of the semielliptical cracks at breakaway is always less eccentric than semicircular.

However, Evans also ignored the problems of the obstacle's elastic stress field, the obtacle's failure mechanisms i.e. cleavage or decohesion and the crack path.

iii) Plastic Deformation of the Second Phase at the Crack Tip

A second phase particle can only cause toughening if the particle is more resistant to crack propagation than the matrix. For a system in which the particle and matrix have comparable elastic and thermal expansion properties, a toughening can only be obtained if G_C for the particle exceeds G_C for the matrix. It is feasible that high stresses in the vicinity of a crack tip could induce plastic flow in second phase particles. Under

conditions of plain strain, the size of the plastic zone (r_g) in front of a crack tip is given approximately by [39]

$$r_y \simeq \frac{1}{6\pi} \left(\frac{K_{IC}}{\sigma_y}\right)^2 \qquad (14)$$

It is apparent that the size of the plastic zone will increase as the yield strength of the second phase particles decrease. Assuming reasonable values of σ_y = 170 M.P.a and $K_{IC} \simeq 1$ MN/m$^{3/2}$ for Ni particles in a glass matrix, a plastic zone size of $r_y \simeq 2.0\mu$ m results. However, when σ_y = 34 M.P.a and K_{IC} = 1 MN/m$^{3/2}$ (for Al particles in glass matrix), a plastic zone 50μ m in size results. For plastic deformation of the second phase particles, good bonding between the matrix and particles must exist to effectively transmit the high stress ahead of the crack tip. Further the stress field due to elastic or thermal mismatch between the particle and matrix should be negligible so as not to alter the crack path thereby causing it to avoid the particles. In the latter case the inherent toughness of the particles is not used. Plastic deformation of particles in a brittle matrix was observed by Mendelson and Fine [40] for Fe in magnesiowustite. However Hing and Groves [41] did not observe a significant increase in fracture energy in MgO crystals containing a ductile dispersed phase.

2.2 Crack Particle Interaction in Particulate Composites

The interaction of a crack front and an array of obstacles is influenced to a great extent by the nature of the stress field developed around the inclusion due to elastic and thermal mismatch between the inclusion and matrix, and the nature and strength of the interfacial bond between them. The importance of the contributions of such interactions to the overall toughening, though recognized for some time, has not been studied in detail. The available information on the nature of such stress fields and their influence upon the toughness of the particulate composites will now be summarized.

2.2.1 Effect of Elastic and Thermal Mismatch on Toughness

If elastic constants such as Young's moduli, Poisson's ratio and Rigidity moduli are different for the inclusions and matrix, elastic stress concentrations related to the applied stress will result. The stress concentrations in an infinite matrix due to the presence of a circular and spherical inclusion (well bonded to the matrix) were worked out by J. N. Goodier [42] using linear elastic theory. For simplicity, the radial (σ_{rr}) and

tangential ($\sigma_{\theta\theta}$) components of the stress field around a circular inclusion are: (in a polar co-ordinate system)

$$\sigma_{rr} = \frac{\sigma_a}{2}(1+\cos 2\theta) + 2\sigma_a[-A(\frac{r}{s})^2 + (B\frac{r^4}{s^4} - C\frac{r^2}{s^2})\cos 2\theta]$$

$$\sigma_{\theta\theta} = \frac{\sigma_a}{2}(1-\cos 2\theta) + 2\sigma_a[A(\frac{r}{s})^2 - B\frac{r^4}{s^4}\cos 2\theta] \qquad (15)$$

where r is the radius of the bonded inclusion and s the distance from the centre of the particle. The coefficients A, B, C are related to the elastic properties of the matrix and inclusion in the following manner [42]:

$$A = \frac{(1-2V_i)G_m - (1-2V_m)G_i}{4[(1-2V_i)G_m+G_i]} \; ; \; B = \frac{G_m - G_i}{4[G_m+(3-4V_m)G_i]}$$

$$C = \frac{G_m - G_i}{2[G_m+(3-4V_m)G_i]} \qquad (16)$$

In Equation (16) G_m, G_i are the modulus of rigidity of the matrix and inclusion and V_m, V_i the Poisson's ratio of the matrix and inclusion respectively. For a pore, $G_i = 0$ which simplifies Equation (15) to

$$\sigma_{rr} = 2\sigma_a[-\frac{r^2}{4s^2} + (\frac{3}{4}\frac{r^4}{s^4} - \frac{r^2}{s^2})\cos 2\theta] + \frac{\sigma_a}{2}(1+\cos 2\theta)$$

$$\sigma_{\theta\theta} = 2\sigma_a[\frac{r^2}{4s^2} - \frac{3}{4}\frac{r^4}{s^4}\cos 2\theta] \qquad (17)$$

Lange [37] investigated the fracture mechanical

behaviour of glass-Al_2O_3 particulate composites. A significant increase in fracture energy was observed and the increase was attributed to an increase in crack front length due to bowing. No attempt was made to include the effect of the elastic mismatch between glass and Al_2O_3. This, however, is significant as $E_{Al_2O_3} \simeq 6\ E_{glass}$. In work on the glass-partly-oxidized-Ni system, Stett and Fulrath [11] indicated that the stress concentrations developed due to the elastic mismatch, may give rise to Griffith flaws of length such as to degrade the composite strength on linking up to form a crack of critical length. However the interaction between this elastic field and the crack tip stress field was not studied. Also not considered was the effect of this interaction on local crack shape, crack path and the consequent overall toughening of the composite. These interactions and their effect on the overall toughening will be studied on the present work for model composite systems.

If the thermal expansion coefficients of the two phases are different, hydrostatic stresses will result in the particles [5] and shear stress around the particle as the body cools from its fabrication temperature. The elastic stresses developed by this thermal contraction were calculated by Selsing [5]. He considered a spherical inclusion of radius r in an elastic matrix and showed that the stresses expressed as

radial and tangential components are given by:

$$\sigma_{rr} = - \frac{\Delta\alpha.\Delta T}{\frac{1+V_m}{2E_m} + \frac{1-2V_i}{E_i}} \left(\frac{r}{s}\right)^3$$

and $$\sigma_{\theta\theta} = \frac{1}{2} \frac{\Delta\alpha.\Delta T}{\frac{1+V_m}{2E_m} + \frac{1-2V_i}{E_i}} \left(\frac{r}{s}\right)^3 \qquad (18)$$

where $\Delta\alpha[=(\alpha_m-\alpha_i)]$ is the difference of thermal expansion coefficient of the matrix and the inclusion, ΔT the temperature difference, and E_m, E_i the Young's moduli of the matrix and inclusion respectively. Now if $\alpha_i > \alpha_m$, from (18), σ_{rr} is tensile whereas $\sigma_{\theta\theta}$ is compressive. When $\alpha_m > \alpha_i$ on the other hand, σ_{rr} is compressive and $\sigma_{\theta\theta}$ is tensile. With good bonding between the inclusion and matrix, the internal stress will be stored in the matrix as "residual stress". When a pre-existing crack approaches a "residual stress" zone, the crack stress field σ_{yy} (for Mode I opening) is influenced by this residual stress. As a result a microcrack zone might form ahead of the main crack. For example, Davidge and Green [13] observed in the glass-thoria system that cracking occurs around the inclusion when the inclusion size is greater than a critical size, though the magnitude of thermal stress is independent of particle size. Lange [45] pointed out that for a crack

to develop around an inclusion as a result of an internal stress, $\sigma_{total}\ r >$(constant), where the constant depends on the nature of the composite. Hence for a given system when σ_{total} is fixed r has to have a certain value. In the present work the effect of thermal stress is eliminated by matching the thermal expansion coefficients of the glass and the inclusions. In this way the influence of the elastic mismatch and interfacial bonding on toughening of the composites is studied exclusively.

2.2.2 The Effect of Interfacial Bonding:

The influence of interfacial bonding on toughness has received the most attention in polymeric particulate composites. In these materials the degree of bonding is controlled by pretreating the particulate phase with coupling agents. Sahu and Broutman [43] made a detailed study of an epoxy-glass sphere system. They found that the strength of these systems decreases with increasing volume fraction glass spheres with a larger decrease for poorly bonded systems. It has already been pointed out (Section 2.1.2) that in weakly bonded systems decohesion of the particles may occur and, for these polymeric particulate systems, a drastic decrease in modular ratio will also occur. Hence the strength behaviour is similar to that associated with porosity. Stett and Fulrath [11] investigated the mechanical

strength of glass-nickel sphere systems. By oxidizing the nickel, they formed a good bond and so increased the strength of the composites dramatically for given volume fractions of nickel. They also reported that the optimum bond strength depends upon the thickness of the oxide layer. In the present work it is also assumed that increasing the thickness of the oxide layer is reflected by increasing bond strength between the nickel and the glass. This is demonstrated via polished sections in Chapter IV. In the Stett-Fulrath studies, [44, 11] the effect of the continuously varying bond strength on the fracture properties of the particulate composite was not studied in detail nor was its effect on the local crack-particle interactions.

CHAPTER III

THEORETICAL ANALYSIS

3.1 The Nature of Elastic Stress Concentration in Brittle Composites

It is known that [4, 3] second phase inclusions with different elastic moduli than the matrix give rise to stress concentrations when a load is applied to a particulate composite. The form of this stress concentration was described in section 2.2.2 for a well bonded circular inclusion. Based on Equation (15), the two dimensional form of the isostress contours for both the radial and tangential components of stress (σ_{rr} and $\sigma_{\theta\theta}$) are plotted in Figure 7 and Figure 8 for Ni particles in a glass matrix. Figure 9 shows the isostress contours for the tangential component, $\sigma_{\theta\theta}$, for a pore in glass. From these plots and the equations for stress concentration around an inclusion, the following points can be noted:

i) for the glass-well bonded Ni particles, the maximum stress concentration does not occur at the particle/matrix interface but at a point in the glass slightly away from the interface (assuming the Ni particles to be well bonded). For this case, the rigidity modulus for the Ni, (Gi) is greater than that of the glass (G_m). The stress

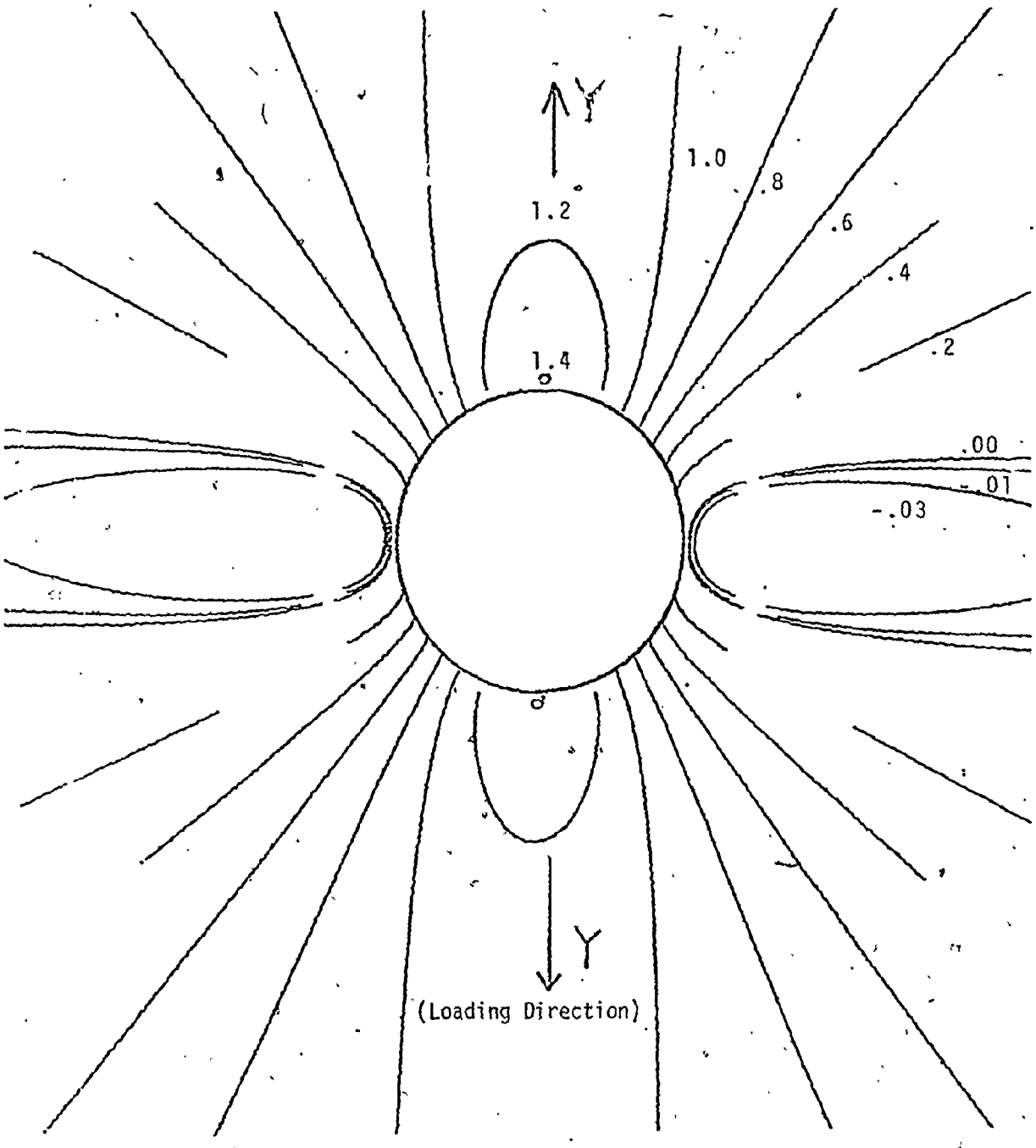

Figure 7 Isostress Concentration Lines for σ_{rr}/σ_{app} around inclusion in glass. The digits represent the value of a given σ_{rr}/σ_{app}.

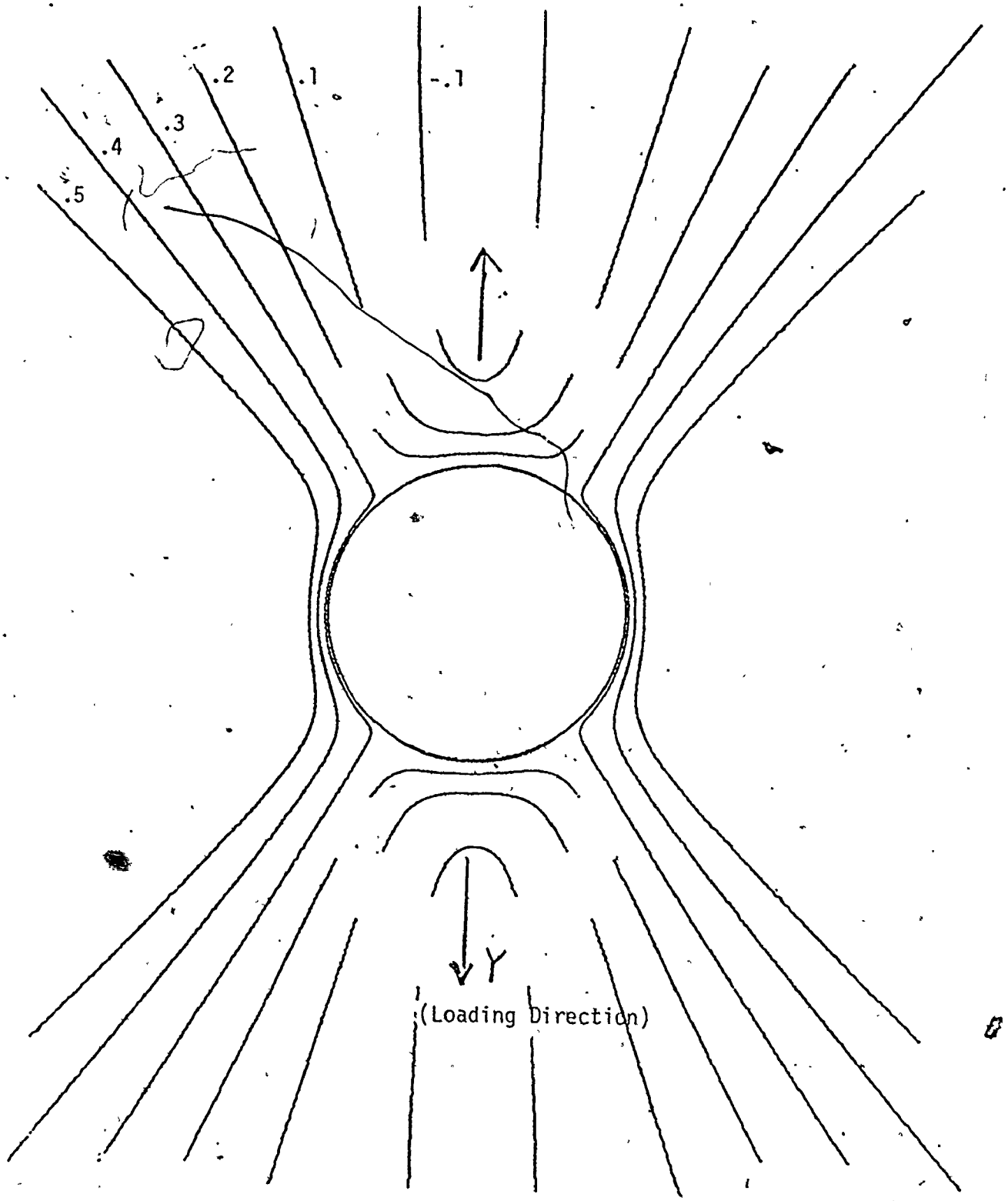

Figure 8 Isostress Concentration Lines for $\sigma_{\theta\theta}/\sigma_{app}$ around inclusion. The digits represent the value of a given $\sigma_{\theta\theta}/\sigma_{app}$.

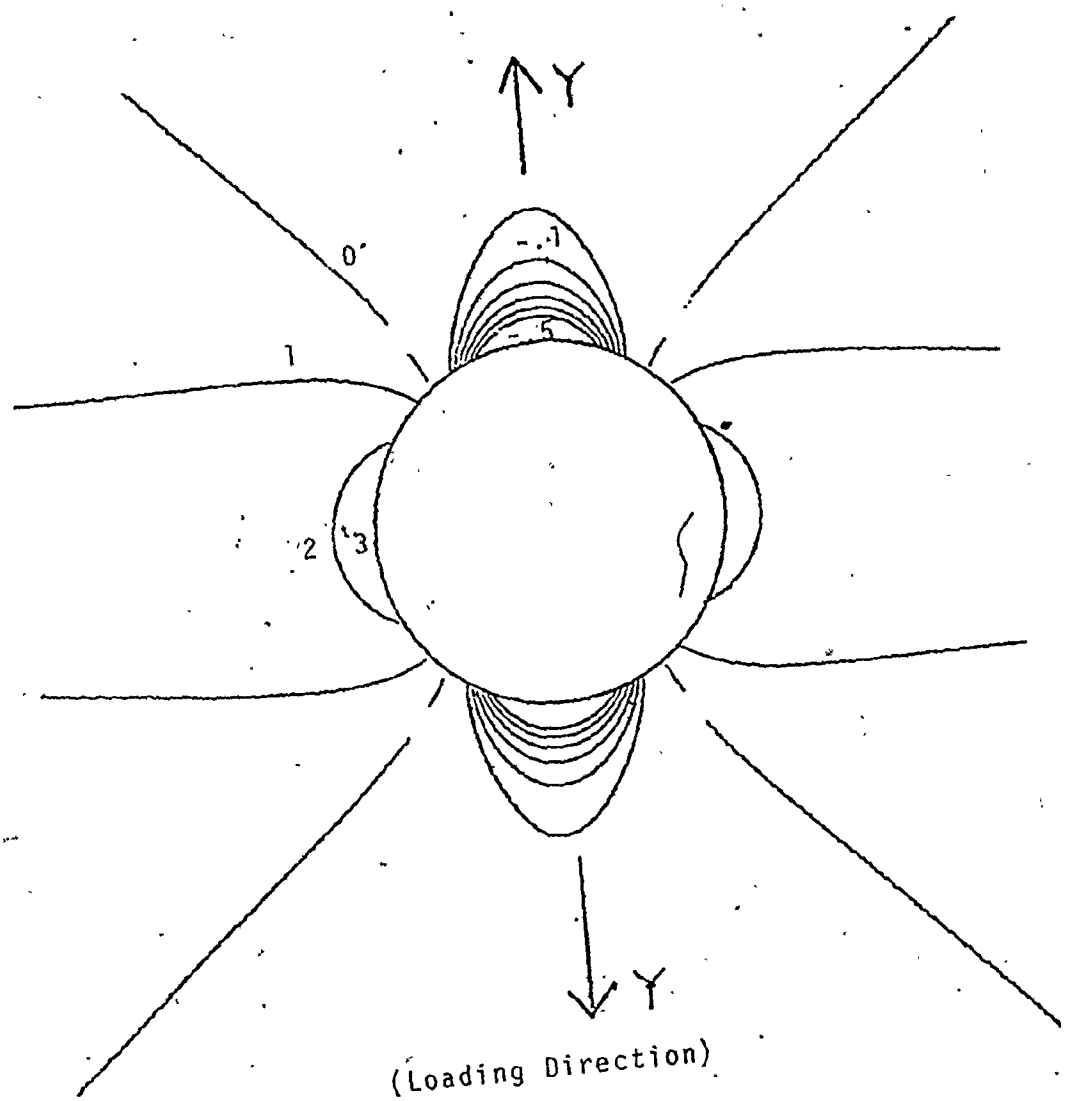

Figure 9 Isostress Concentration Lines for $\sigma_{\theta\theta}/\sigma_{app}$ Around Pore (E_i=0). The digits represent the value of a given $\sigma_{\theta\theta}/\sigma_{app}$.

maximum occurs in the radial component of the stress field along the $\theta = 0^0$ direction (Figure 7). The tangential component $\sigma_{\theta\theta}$ is tensile along $\theta = 90^0$ but less than σ_{app}. This may however influence the velocity and shape of a crack front approaching the second phase particle.

ii) For a pore, the maximum stress concentration occurs in the tangential component ($\sigma_{\theta\theta}$) of the stress system (Figure 8) along $\theta = 90^0$. The maximum value of $\sigma_{\theta\theta}$ for a pore is greater than the maximum value of σ_{rr} for an inclusion.

iii) If $G_i < G_m$, Equation (15) indicates that $\sigma_{\theta\theta} >> \sigma_a$ and is tensile in nature for the $\theta = 90^0$ orientation. For the orientation $\theta = 0^0$, $\sigma_{\theta\theta}$ is compressive and becomes tensile further into the matrix (Figure 9). In the case of $G_i > G_m$ Equation (15) also indicates that $\sigma_{\theta\theta}$ is always smaller than σ_a for any direction (Figure 8). $\sigma_{\theta\theta}$ is tensile along both $\theta = 90^0$ and 0^0. There is a compressive region in the radial component σ_{rr} near $\theta = 90^0$ for $G_i > G_m$ (Figure 7); however the value of this compressive field is small, although it may retard the local velocity of an approaching crack front to a limited extent.

Hence, depending on the value of the elastic properties of the second phase and the glass, the crack front velocity, shape and crack path will change. This is studied in detail for the glass - partly oxidized nickel system using an ultrasonic fracture - surface modulation technique discussed

in Chapter IV.

3.2 Model to Calculate the Change of K_I Value of a Moving Crack in the Presence of an Elastic Mismatch:

Using the complex variable approach and the elastic solutions given by Muskhelishvilli [44], Tamate [45] and Tirosh and Tetelman [46] showed that numerical solutions can be obtained for the change of local stress intensity factor for a crack approaching a cylindrical inclusion. However an estimate of the change of local K_I values for a crack, due to the presence of stress fields around cylindrical as well as spherical inclusions, can be made by adopting the concept of an "image stress" on the crack front due to the inclusion it is approaching [47]. This approach gives a simple analytical solution for the change of local crack driving force caused by elastic and thermal stresses around inclusions. In the present analysis the influence of thermal stress in not treated as the model composites investigated were designed to minimize these stresses.

Considering a crack moving on an infinite plane coincident with the equatorial plane of an inclusion (Figure 10); a biaxial stress condition exists along this plane. If σ_a is the applied stress in a body containing

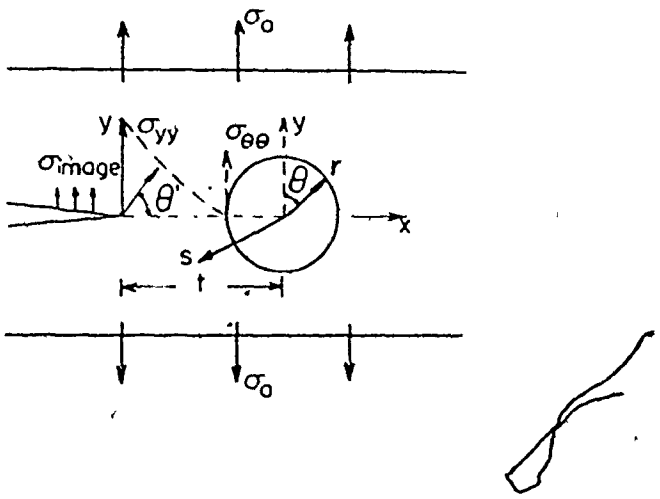

Figure 10 The interaction between an inclusion and a crack in the matrix in the near vicinity of the inclusion.

no inhomogenitics, the introduction of a second phase of different elastic properties will change the stress condition of the body i.e.

$$\sigma_{new} = (\sigma_i)_{\text{due to } \sigma_a} - \sigma_a \qquad (18)$$

where σ_i is the stress concentration due to the presence of the inclusions in the applied stress field, σ_a, in the absence of a crack. When a crack front is very near the inclusion, σ_i will mostly result from the σ_{yy} component of the crack field and the effect of σ_a will be negligible in this case. Hence under this condition

$$\sigma_{new} = (\sigma_i)_{\text{due to } \sigma_{yy}} - \sigma_{yy} \qquad (19)$$

The σ_i along the equatorial plane of a circular and spherical inclusion due to an applied stress (in this case the biaxial crack front stress $\sigma_{yy} = \sigma_{xx}$ along $\theta = 0$ orientation) can be found from Goodier's solution [49] for the tangential component of the stress field around a circular inclusion (Equation 15; rewritten for convenience):

$$\sigma_{\theta\theta} = \frac{\sigma_a}{2}(1-\cos 2\theta) + 2\sigma_a\left[A\left(\frac{r}{s}\right)^2 - 3B\left(\frac{r}{s}\right)^2 \cos 2\theta\right] \qquad (20)$$

and around a spherical inclusion:

$$\sigma_{\theta\theta} = \frac{\sigma_a}{2}(1-\cos 2\theta) + \frac{\sigma_a}{2}\left[\left(-A'\frac{r^3}{s^3} - \frac{2V_m C'}{1-2V_m}\frac{r^3}{s^3} - \frac{3B'r^5}{s^5}\right)\right.$$

$$\left. + \left(3C'\frac{r^3}{s^3} - 21B'\frac{r^5}{s^5}\right)\cos 2\theta\right] \qquad (21)$$

In Equations (20) and (21), r is the radius of the inclusion, s is the distance from the centre of the inclusion (Figure 10) and A, B, A', B' and C' are constants whose value depend on the elastic mismatch:

$$A = \frac{(1-2V_i)G_m}{4(1-2V_i)G_m+G_i} ,$$

$$A' = \frac{G_m - G_i}{2(7-5V_m)G_m+(8-10V_m)G_i} \times \frac{(1-2V_i)(6-5V_m)2G_m+(3+19V_i-20V_mV_i}{(1-2V_i)2G_m+(1+V_i)G_i}$$

$$+ \frac{[(1-V_m)(1+V_i)/(1+V_m)-V_i]G_i-(1-2V_i)G_m}{(1-2V_i)2G_m + (1+V_i)G_i} ,$$

$$B = \frac{G_m - G_i}{4[G_m+(3-4V_m)G_i]} , \quad B' = \frac{G_m - G_i}{2(7-5V_m)G_m+(8-10V_m)G_i}$$

$$C' = \frac{5(1-2V_m)(G_m-G_i)}{2(7-5V_m)G_m+(8-10V_m)G_i}$$

For $\theta' = \theta + \pi/2$ it follows, from Equation (20), that for a circular inclusion:

$$(\sigma_{\theta\theta})_{\theta+\pi/2} = \frac{\sigma_a}{2}(1+\cos 2\theta) + 2\sigma_a[A(\frac{r}{s})^2 + 3B(\frac{r}{s})^4 \cos 2\theta]$$

Hence in any direction, the biaxial tangential component of stress due to the inclusion is [by addition of equations (20) and (22)];

$$(\sigma_{\theta\theta})_{biaxial} = \sigma_a + 4A\sigma_a\left(\frac{r}{s}\right)^2 \equiv (\sigma_i)_{\text{due to } \sigma_a} \quad (23)$$

When the crack front is very close to the inclusion and is running in the $\theta' = 0^o$ direction (Figure 10), Equation (23) modifies to;

$$(\sigma_{\theta\theta})_{biaxial} = (\sigma_{yy})_{\theta=0} + 4[(\sigma_{yy})_{\theta'=0^o}]A\left(\frac{r}{s}\right)^2 \equiv (\sigma_i)_{\text{due to } \sigma_{yy}} \quad (24)$$

as $\sigma_{yy} >> \sigma_a$

Hence the "new stress" acting along the crack front when it is close to the inclusion is [from Equations (19) and (24)];

$$\sigma_{new} = (\sigma_{\theta\theta})_{biaxial} - (\sigma_{yy})_{\theta'=0^o}$$

$$= 4A\left(\frac{r}{s}\right)^2 (\sigma_{yy})_{\theta'=0}$$

$$= 4A\left(\frac{r}{s}\right)^2 \frac{K_I}{\sqrt{2\pi t}} \qquad \text{as } (\sigma_{yy})_{\theta'=0} = \frac{K_I}{\sqrt{2\pi t}} \quad (25)$$

where t is the distance of the crack front from the centre of the inclusion and K_I the stress intensity factor (Mode I) at the crack tip in the absence of the inclusion. This σ_{new} will change the value of the crack intensity factor K_I of the crack front by "ΔK" under the restriction of the following boundary condition for the crack shown in Figure 10:

$$\Delta K - \int_{s=\alpha}^{s=t} \sigma_{image} \sqrt{\frac{2}{\pi(s-t)}}\, ds = 0 \qquad (26)$$

where σ_{image} is equal to σ_{new} given in Equation (25) but is acting in the opposite direction so as to satisfy the condition given in Equation (26). Hence from (26);

$$\Delta K = \sigma_{new} \int_{s=\alpha}^{s=t} \sqrt{\frac{2}{\pi(s-t)}}\, ds$$

$$= \frac{4Ar^2 K_I}{\pi\sqrt{t}} \int_{s=\alpha}^{s=t} \frac{ds}{s^2(s-t)^{\frac{1}{2}}} = -\frac{2Ar^2}{t^2} K_I \qquad (27)$$

For circular inclusion therefore, the effective stress intensity factor for the crack front as it approaches the inclusion, is:

$$(K_{new})_{\text{elastic mismatch}} = K_I - \Delta K = K_I\left(1+\frac{2Ar^2}{t^2}\right) \qquad (28)$$

Similarly for a spherical inclusion, using Equation (21) for $\sigma_{\theta\theta}$ and the same procedure from Equations (22) to (28), the effective stress intensity factor for the crack front as it approaches a spherical inclusion is,

$$(K_{new})_{\text{elastic mismatch}} = K_I\left[1-0.39A'\frac{r^3}{t^3} - \frac{0.78V_m C'}{(1-2V_m)}\frac{r^3}{t^3} - 0.820B'\frac{r^5}{t^5}\right] \qquad (29)$$

From the foregoing analysis (Equation 29), it is

evident that the nature of the influence of an inclusion and a pore on the crack driving force K_I(Mode I) of an approaching crack front is clearly different and characterized by the value of the elastic mismatch coefficients A', B' and C'. If the values of A', B' and C' are such that $K_{new}<K$, then the velocity of the crack front will decrease as it approaches the inclusion. On the other hand, if the value of A', B' and C' are such that $K_{new}>K$, then the velocity of the crack front will increase as it approaches the inhomogeneity. For example, in a glass/well-bonded Ni composite, A'=0.458, B'=-0.166 and C'=0.50, so that, $K_{new}<K$ (from Equation (29)) and the velocity of the crack front should locally decrease as it approaches a spherical well-bonded nickel inclusion in a glass matrix. In fact the velocity will be decreased for a spherical inclusion for which $G_i>G_m$. On the other hand, for a pore $G_i=0$ ($<G_m$) so that $K_{new} > K$ (from Equation 29) and an approaching crack front will be locally accelerated towards a pore. However these changes in the K_I values are small for example ≃12% well-bonded Ni particles and ~25% for a pore in glass. This kind of local deceleration or acceleration of the crack front near an inclusion or pore will change the shape of the crack front as it approaches. Hence from the experimental observation of whether the crack front is repelled or attracted or unaffected, the extent

and nature of the interaction between the crack front and a second phase particle can be inferred. In the case of a well-bonded inclusion with $G_i >> G_m$, the influence of the radial stress concentration σ_{rr} at the poles of the inclusion (Figure 7) may alter the crack path, influencing the crack to avoid the particle and minimizing the interaction in such composites.

3.3 Summary of the Possible Consequences of Elastic Mismatch and Varying Interfacial Bond Strength:

i) For elastic stress concentrations to develop as a result of elastic mismatch between inclusion and matrix, good bonding is a prerequisite. If stress concentrations do develop and the stress field ahead of an approaching crack front cannot decohese the interface, the crack may alter its path and thus totally avoid interaction with the second phase. In this case the inherent toughness of second phase is not utilized and the improvement in toughness may be insignificant. In this case the only contribution to fracture energy will be due to the creation of additional surface as the crack avoids the particle. This is given by:

$$\Delta\gamma_t = \gamma_o \cdot \Delta A = \gamma_o \cdot f \cdot \Delta S = \gamma_o f \pi r^2$$

where, for a spherical particle of radius r is the areal fraction of such particles on the fracture surface and ΔS the increase in area ($= \pi r^2$).

ii) For particles which are unbonded to the matrix, there may be some toughening due to the local blunting of the crack front, as discussed in Section 2.1.2. For weak interfaces, decohesion may occur due to the stress field ahead of the crack and the crack may then interact with these 'pseudopores'. This may be an interesting toughening mechanism if the elastic mismatch between inclusion and matrix cannot be eliminated. The decohesion mechanism of toughening particulate composites is also discussed in Section 2.2.2.

iii) The system where the elastic and thermal mismatch between the matrix and second phase are minimized, and the bonding between the matrix and inclusion is higher than the yield strength of second phase, will give optimum toughness.

These aspects of fracture and of local crack-particle interaction are studied in the present work using fracture toughness data, S.E.M. fractography and ultrasonic fractography on model composite systems. The bonding strength between matrix and inclusion is continuously varied with fixed elastic mismatch. Thermal stresses are eliminated.

The glass well-bonded partially-oxidized aluminum composite was studied to check the experimental findings for optimization of the toughness of a brittle particulate composite.

3.4 Theoretical Basis of the Experimental Methods:

3.4.1 Measurement of G_{IC} in Brittle Materials:

In fracture mechanics testing, a crack of known length is introduced into a sample and from a knowledge of the applied load at failure, the values of G_{IC} or K_{IC} can be determined. For brittle materials, it is usually assumed that fracture occurs when the normal stress in the vicinity of the crack tip reaches the critical value for bond rupture. There will be a critical value of K_{IC} corresponding to this condition and this is a material parameter. The measurement of stress intensity for fast fracture, K_{IC}, has shown this to be the case when fracture occurs by Mode I opening under plane strain conditions. For very brittle materials the lateral constraint along the crack front generally ensures the plane strain condition. In less brittle materials, plastic flow can relax this constraint producing larger plane stress regions. To ensure plane strain conditions in the present case, the sample thickness is chosen to be greater than $2.5(\frac{K_{IC}}{\sigma_y})^2$ [8]. The thickness constraint is often satisfied for

highly brittle materials though the sample must be thick enough to be microstructurally representative. The limited plasticity generally allows fracture mechanics to be used in an ideal way.

The specimen geometry chosen for this work was the double cantilever beam (Figure 11). This specimen geometry was first adopted for brittle materials by Gilmann [48]. An expression for the stress intensity factor was worked out by Weiderhorn et al [57]:

$$K_I = 3.45 \frac{Pa}{bh^{3/2}}[1 + .66\ h/a]$$

Evans [56] pointed out that the use of the DCB test for opaque samples is difficult as the crack length is difficult to measure and also because of slow crack growth before the onset of critical failure. To remove these difficulties, Kannien [49] and Hoagland [50] suggested that the G_{IC} values can be obtained by compliance measurements. The strain energy release rate G_I is related to K_{IC} through the following Equation [8]:

$$G_I = \frac{K_I^2}{E} = \frac{P^2}{2} \frac{d\phi}{dA} \qquad (30)$$

where ϕ is the compliance of the sample $\equiv \frac{Y}{P}$, Y being the deflection at load P, dA the change of area due to crack extension i.e. the change of crack length 'da' for unit

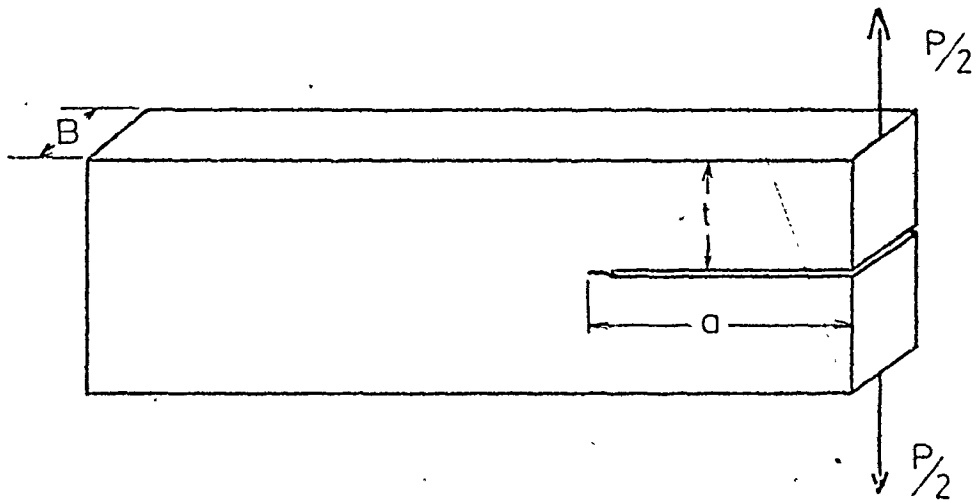

Figure 11 Specimen Geometry for Double Cantilever Beam Fracture Toughness Testing.

thickness of the sample. From expression (30) for G_I, for unit thickness,

$$\phi \equiv \int_0^a \frac{2}{P^2} G_I \cdot da \cdot b$$

The bending moment of a cantilever beam rigidly attached at one end is given by [58];

$$Y \equiv \frac{2Pa^3}{3EI} \qquad (31)$$

where Y is the total deflection of both beams, I the moment of inertia of the beam about its neutral axis ($\equiv \frac{bh^3}{12}$) and E the Young's modulus of the beam.

Expression (31) does not account for shear deformation in the beams. Further, for double cantilever beam specimens, the ends of the beams are not rigidly fixed but are attached to the rest of the sample. Recently, using the beam on elastic foundations approach, Kannien [49] gave the following expression for the deflection of the beam as a function of crack length 'a';

$$Y_c \equiv \frac{2P_c}{3EI}\left(1 + .64\,\frac{h}{a_c}\right)^3 \qquad (32)$$

From Equation (30) therefore;

$$K_{IC} = \frac{2\sqrt{3}P_c a_c}{bh^{3/2}}\left(1 + .64\,h/a_c\right) \qquad (33)$$

It is clear from Equations (33) and (30) that load-deflection measurements can be used to determine K_{IC} and consequently G_{IC}. Hence the difficulty of measuring the crack length in opaque materials can be circumvented. However the deflection Y_c of brittle ceramic materials prior to fracture is very small (<.010") and its accurate determination requires the use of ultra-sensitive resistance strain gauges. This method of obtaining G_{IC} through load-deflection data is more advantageous than the method involving measurement of crack length because the slow crack growth that may occur before critical crack propagation even in the most brittle ceramic materials is irrelevant. When G_{IC} is obtained from the load-deflection curves, the onset of critical propagation is characterized by the sudden drop in the load and the deflection Y_c at this point is related to the critical crack length, a_c, through Equation (32). Since the displacements are measured directly via a strain gauge and the loads for fracture are usually small (<50 lbs.), the stiffness of the testing rig does influence the fracture toughness values.

Another important aspect to consider in DCB testing for fracture toughness is a tendency for an unconstrained crack to turn from the desired plane of extension and break off one beam, [59]. To promote planar extension,

it is a common practice to introduce side-grooves in the specimen to guide the crack path. These side grooves require two corrections to the earlier expression to G_{IC} i.e.:

i) a width correction must be applied to account for the reduced fracture surface area.

ii) a moment of inertia correction to account for the reduction in strain-energy stored in the specimen beams. This correction is usually small and often neglected.

Hoagland [50] introduced the correction for reduced fracture surface area and gave the following expression for fracture toughness G_{IC} of a brittle material tested in the DCB loading configuration with side grooves, using Kannien's expression [49] for deflection, Y, of a beam and Equation (30),

$$G_{IC} \equiv \frac{P}{b}\left(\frac{9P_c^4 Y_c^2}{4EI}\right)^{1/3} \qquad (34)$$

where P_c and Y_c are correspondingly the critical load and deflection of the beams at the initiation of critical propagation of the sharp crack.

Finally in the DCB testing of brittle materials, care must be taken in the design of the loading fixture because of the low loads required for fracture. Proper alignment is critical and the loading fixture must minimize

the Mode II and Mode II stress components.

The elastic constant E appears in the expression for strain energy release rate G_{IC} (Equation 34). The elastic moduli of the composites were determined by static tests in which relatively large loads were applied to the bend specimens and the resulting deflections measured. A value of the Young's modulus can be determined from the four point bend strength tests [described in the next section] using the relationship [9]

$$E = \frac{7P}{32\ \delta w^3} \qquad (35)$$

This is considered however, to give only approximate results and the deflection δ was measured from load time graph. These experimentally determined values are less accurate than the values determined by ultrasonic methods [9] but can be utilized nevertheless in G_{IC} calculations because a slight error in the measurement of E (e.g. 10%) gives rise to an overall error of ±3.3% in G_{IC} as G_{IC} varies as $E^{-1/3}$.

3.4.2 Fracture Strength Measurements by Four Point Bend:

Strength measurements are generally used for two purposes; to compare the relative merits of different

materials and to provide data for adequate design of engineering structures. The strength testing of brittle materials can be a difficult process as imperfections in the test apparatus and specimens give rise to undesirable and unaccountable stresses, accommodatable only in ductile materials. The direct uniaxial tension test appears to be the simplest for strength testing but gripping problems with brittle materials make the experimental details difficult. In this respect, bend tests are often used to obtain strength data as elasticity theory shows that the outermost fibres of a bend specimen experience uniaxial tension. Comparison between bend and direct tension test results show that less energy is stored in the system in a bend test. The bend-test is thus a "harder" test. In particular, the four-point-bend test is usually adopted in the testing of ceramic materials as it provides a maximum constant moment over a substantial length of specimen. The idealized moment and loading conditions are shown in Figure 12. Failure occurs between the inner load points. Any strength data arising from failure outside this region are rejected. Assuming the material to be homogeneous and linear elastic, simple beam theory [58] yields the longitudinal stress $\sigma_{\parallel}$ as:

$$\sigma_{\parallel} = \frac{M_I}{I}$$

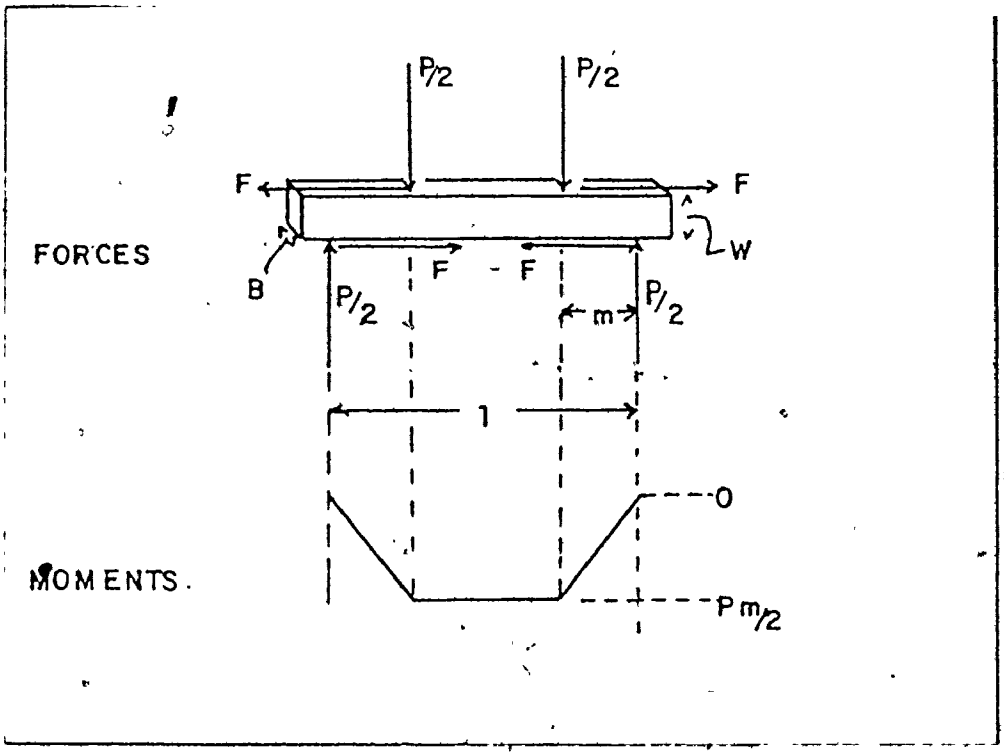

Figure 12 Specimen Configuration and Idealized Moment and Loading Distribution for a Four Point Bend Fracture Test.

where I is the moment of inertia of the section and M is the bending-moment. It can be shown that [61] $\sigma_{\parallel}$ gives rise to a maximum outer fibre stress of

$$\sigma_{max} \equiv \frac{PXW}{4I} \qquad (36)$$

or $\sigma_{max} \equiv \frac{3PXW}{bh^3}$ where $I = \frac{bh^3}{12}$

The major sources of error in this configuration are:

i) friction forces at the load points

ii) incorrect spacing of the load points and unequal distribution of the loads

iii) twisting and wedging.

To eliminate this, a special testing rig was used (designed by Hoagland [50]) which has a self-aligning mechanism.

3.4.3 Ultrasonic Fractography:

It is well-known that Wallner lines are produced on glass fracture surfaces [62] when a distortional stress wave interacts with the crack front. These lines can be used to determine the crack velocity. Kerkhoff [51] developed a technique for producing artificial Wallner lines on fracture surfaces. This gives ripple markings in a systematic way rather than in a naturally occurring fashion. The markings are produced by sending a transverse shear wave

of ultrasonic frequency through the sample at the same time as a crack is propagating through the material. The fracture path is therefore, modulated leaving permanent 'ripple' markings on the fracture surface. Crack velocities can be obtained easily from the ripple spacing and the known frequency of the shear wave i.e.

$$V_{local} = d \times n \qquad (37)$$

where d → is the ripple spacing and n is the frequency of the imposal wave.

The ultrasonic method is better than 'cine' techniques for measuring crack velocities as it leaves a permanent record of the fracture process on the fracture surface. Another aspect of ultrasonic ripple markings is that they also serve as a record of the shape of the crack front. This aspect has been exploited recently by Green [9] in studying crack-particle interactions in brittle glass porous inclusion systems. A brief account of the theoretical aspects of formation of ripple markings is given below.

According to the normal stress hypothesis [51C] the crack front will always propagate in a direction perpendicular to the maximum principal stress present at any given moment. In this way the crack is guided by the principal stress at any given moment and the elastic processes are 'documented' onto the fracture surface. The interaction

of the fracture stress and the elastic events can be used to investigate crack propagation. In his treatment of the problem, Kerkhoff [51b] assumes that the transverse stress components are small and considers only those stress components in a plane perpendicular to the crack front and hence the crack direction is altered only in the plane perpendicular to the crack front.

For simplicity, consider tensile shock loading situations where the maximum principal stress σ_1 that was originally in the direction of the applied stress σ_A is altered (Figure 13a). The superposition of the applied stress and the shock wave stress changes the magnitude and direction of the principal tensile stress momentarily and it will now act at a different angle γ. The change of direction will be defined by same angle (Figure 13a).

For a mathematical treatment, the direction of the shockwave is defined by the positive x' direction (Figure 13a) of the right-angled coordinate system (x',y'). This system is rotated against the body fixed system (x, y) depending on the incidence of the impressed wave. (α, β) represents the angle between the wave normal (in x' direction) and the positive x axis for a longitudinal and transverse wave respectively. After the action of a modulated stress, the fracture surface subtends an angle

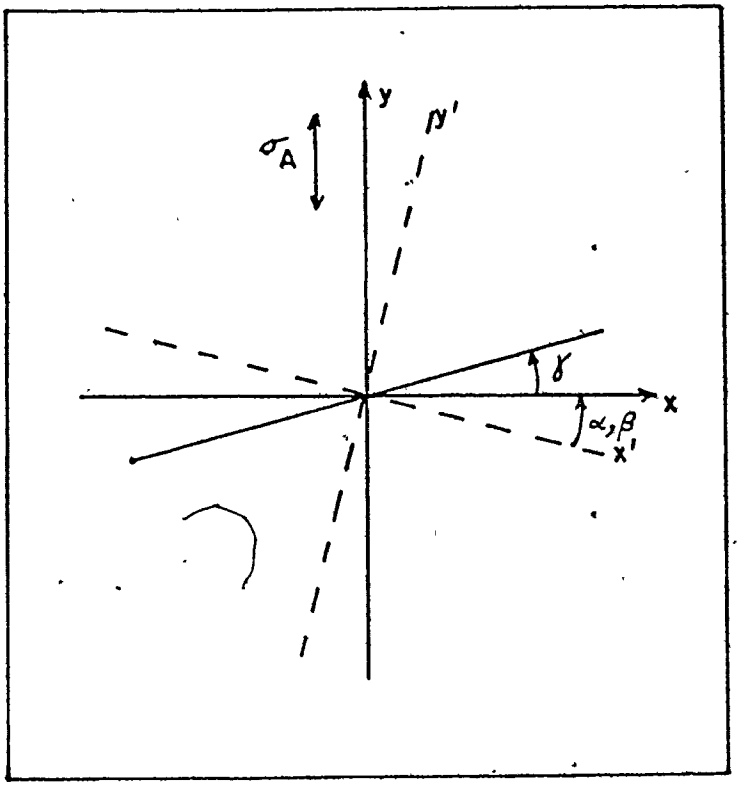

Figure 13(a) Co-ordinate System for the Theoretical Discussion of Interaction of Elastic Waves with a Crack Front. σ_A denotes the Quasi-static Applied Tensile Stress in the y Direction. The Normal of the Modulating Wave is in the x' Direction. The Change in Crack Direction is denoted by the Angle γ.

γ with the original direction. For a shear shock in the x' direction the stress components in the (x', y') stress tensor are:

$$\begin{pmatrix} 0 & -\tau \\ -\tau & 0 \end{pmatrix}$$ where $\tau \equiv$ magnitude of imposed shear stress.

which transforms to (x, y) system as [Kerkhoff, 51(b)];

$$\begin{pmatrix} -\tau \sin 2\beta & \tau \cos 2\beta \\ -\tau \cos 2\beta & \sigma_A + \tau \sin 2\beta \end{pmatrix}$$

The quasi-static stress σ_A is simply superimposed on the transformed σ_{yy} component. The principal stress axis is given by:

$$\tan 2\gamma \equiv \frac{2\tau \cos 2\beta}{\sigma_A + 2\tau \sin 2\beta}$$

For a weak shear wave this gives:

$$\gamma \equiv \frac{\tau}{\sigma_A} \cos 2\beta \qquad (38)$$

Hence, from Equation (38), the change in crack direction depends on the stress ratio τ/σ_A and the angle of incidence of the shear shock. For a weak transverse wave there will be no modulation for angles of incidence of $\beta \equiv \pm \pi/4$. Optimum modulation will occur for $\beta=0$ or $\pm \pi/2$. However, in shock loading, determination of the local velocity change is not possible as the ripple mark-

ings on the fracture surface are not repetitive. If a continuous ultrasonic wave modulates the crack surface and the frequency interval of the wave is used, it is possible to calculate the change of crack front velocity as it approaches an elastic disturbance through Equation (37). Such ultrasonic ripple markings on a plain glass surface are shown in Figure 13b.

The most suitable method for photographing an ultrasonically modulated fracture surface was found to be the incident-light shadow method [9]. This is based on a defocussed image of the fracture surface and an example is shown in Figure 14. The ripple markings are very shallow (<0.1 micron) but can act as parabolic cylindrical mirrors to focus the light on reference planes R_o and R_u as line foci. The magnification may be in slight error in this technique since the surface (O_b) does not coincide with R_u or R_b; however, this error will be 'systematic' for all velocity measurements and will not interfere with the overall picture of the change of velocity of crack front as it approaches a disturbance. Interference microscopy is also useful for studying the surface topography; however rough surfaces make interpretation difficult sometimes. For electron microscopy (SEM), larger surface deflections are needed to obtain acceptable image contrast. Improved

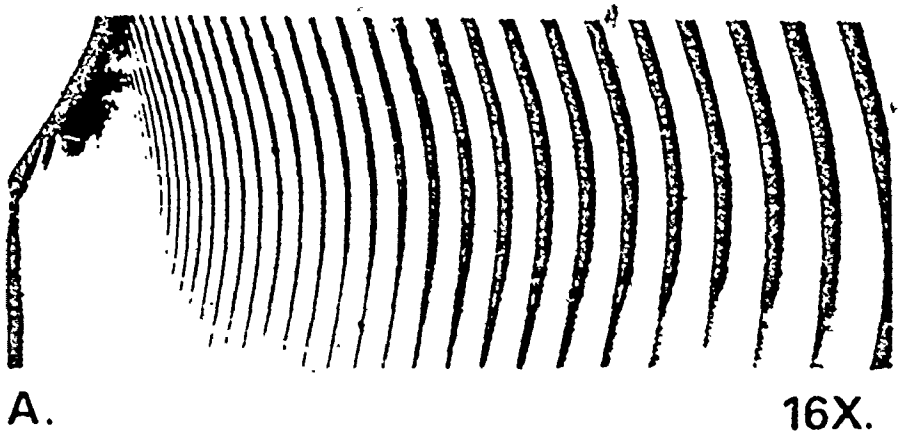

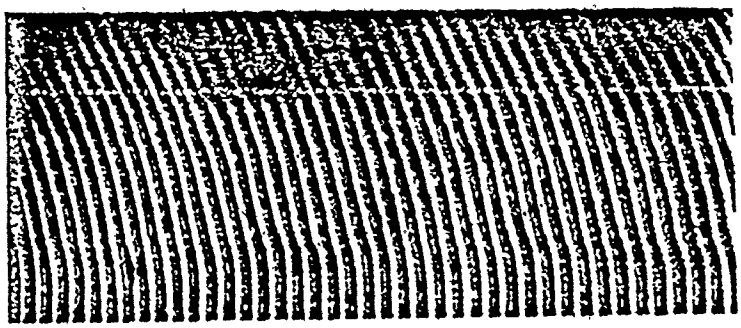

Figure 13(b) Ultrasonically-modulated Fracture Surfaces for Two Samples broken under Tension. Specimen a) courtesy of Dr. F. Kerkhof, Freiburg, b) courtesy of Dr. J. E. Field, Cambridge.

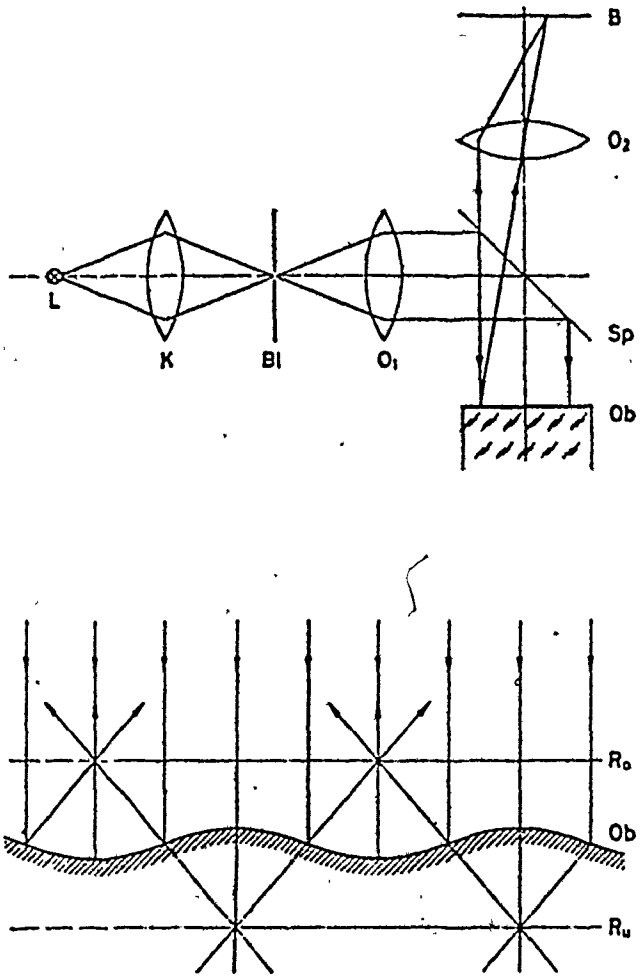

Figure 14 Principle of Viewing the Ultrasonic Lines using a Defocussed Optical Image.

resolution was obtained in the present study using a Nomarski interference technique [64].

For crack velocity determinations, good photographic reproductions of the fracture markings and accurate measurements of the ultrasonic wave frequency are necessary. The error in frequency measurements is generally <1% for commercial frequency counters in this high frequency range and so it is important to measure, d, the ripple spacings, accurately.

CHAPTER IV

EXPERIMENTAL AND RESULTS

4.1 Overview of the Experimental Programme:

4.1.1 Formulation of Model Composite Systems:

Since the elastic mismatch between the inclusion and matrix and the extent of interfacial bonding between them, will influence the crack propagation behaviour in a particulate composite, an experimental project was undertaken using glass/nickel, glass/aluminum and glass/alumina composites. Table IVA gives the composition of the glasses used with the relevant elastic and thermal coefficients. The elastic and thermal properties of the inclusions are also listed in Table IVA for comparison. The thermal expansion coefficients of the glass matrix and the inclusions were closely matched in all systems to minimize the effect of thermal stress on the crack propagation behaviour. This matching faciliates clear identification of the effect of elastic mismatch upon the crack propagation behaviour. Glass was chosen as the matrix material because it is an ideal "Griffith material" with no internal surfaces. Also, as the physical properties of glass can be tailored by variations of chemical composition (see for example, the thermal expansion coefficient

TABLE IV (A) (Abbreviations used are defined in Text)

Composite Systems	Glass Compositions (%WF)	Second Phases	Volume fraction (Λ)	Particle Size	α_m $X10^{-6}$ (per ^0c)	α_i $X10^{-6}$ (per ^0c)	E_m $X10^6$ (P.S.I.)	E_i $X10^6$ (P.S.I.)	Vm	Vi	ρ_m	ρ_i
I	55% SiO_2 15% Al_2O_3 30% Na_2O (S glass)	Partly oxidized Ni particles; oxidation time: 0, 30, 60, 90, 120 mins.	7% and 3% at 30, 60, 90, 120 mins. 0%, 7%, 15%, 20% at 30 mins.	-100, + 140 mesh size	13.8	~13.9	9.8	30	.2	.40	2.47	8.9
II	50% SiO_2 37% Na_2O 7% Al_2O_3 6% Li_2O (M glass)	Partly oxidised Aluminium; oxidation time: 180 mins.	0%, 7%, 15%, 20%	-100, + 140 mesh size	~16.0	~16.0	9.1	~9.0	.2	.40	2.47	2.74
III	70% SiO_2 16% Na_2O 14% B_2O_3 (D glass)	Al_2O_3 sphere (porous)	0%, 7%, 15%, 20%	-100, + 140 mesh size	~8.0	~8.0	11.7	60	.2	.257	2.47	3.9

values in Table IV(A)), it is an ideal matrix material.

Table IV(B) summarizes the purpose of investigating the chosen systems. The glass/Ni system was chosen because of reported work on the effect of interfacial bonding on the mechanical strength of this particulate system [11]. The nature of the interfacial bonding in this system can be controlled by varying the oxidation time of the nickel particles [11]. The system also allows examination of the effect of elastic mismatch on crack propagation behaviour; moreover, the Ni particles being ductile, have a high inherent toughness.

The glass/aluminum system was chosen because the elastic mismatch between inclusion and matrix is minimized. Hence, the crack will not follow any preferrential path in the matrix as it is undisturbed by any elastic stress field due to elastic mismatch. Here the toughness of the Al particles may be effectively used, provided satisfactory bonding between the glass and the inclusion can be induced. This was ensured by partially oxidizing the Al particles for three hours at 450°C.

The glass/Al_2O_3 system was studied to elucidate crack-particle interactions in a brittle-brittle composite wherein the elastic mismatch between the inclusion and matrix is large i.e. $E_{Al_2O_3} \simeq 6\ E_{glass}$. However spherodi-

TABLE IV (B): Short Summary of Purposes of Investigation

Composite Systems	Purposes
I	In this system the interfacial bond strength was varied by varying the oxidation time of Nickel particles to study the effect of varying bond strength on local crack particle interaction in a particulate composite. In this system Ei ≈ 3Em and hence considerable elastic stress concentrations occur in presence of good bonding. This also gives an opportunity to study the effect of elastic stress concentrations on the fracture mechanical behaviour.
II	In this system, E_{Al} ≈ Eglass and hence no elastic or thermal stress concentrations exist in this system. The bonding between the matrix and inclusion was not varied but kept fixed. The effect of increasing the volume of fraction dispersion of aluminum particles is studied in the absence of elastic stresses.
III	Here Ei ≈ 6Em and also the dispersion is absolutely brittle. The bonding between the Al_2O_3 particles and matrix is adequate. However due to occurrence of porosity in the Al_2O_3 while spherodizing, this system represents a glass-well-bonded highly porous particle system.

zation of the Al_2O_3 particles was a problem as this process gave rise to internal porosity reducing the effective elastic modulus. Hence, the purpose of this aspect of the study was not fulfilled and detailed study was abandoned. Also many fractographic and fracture toughness results are already available in this system [33, 36].

4.2 Preparation of Composites

The preparation of the model composites involved a series of fabrication steps.

4.2.1 Making of Glasses From Raw Materials:

The compositions of S glass, M glass and D glass are given in Table IV(A). The raw materials for the respective glasses were dry mixed in a tumble mill and then melted and fired in a fireclay crucible in an electric globar furnace at ~ 1450°C for the S glass, ~ 1400°C for the D glass and ~ 1050°C for the M glass. During heating, the powders were first calcined at 700°C for eight hours before the temperature was raised to the respective melting temperatures. This calcination procedure was suggested by Lange [33] to reduce excessive water and gas absorption during melting which subsequently influences the hot pressing behaviour of the powder. The melts were kept at their

respective temperatures for ten hours to "fine" [removal of bubbles] and each was then cast into a graphite mold.

The coarse fractured glass was then ground by passing it through a jaw crusher followed by a pulverizer. The resultant glass powders were characterized by density and chemical analysis to determine the level of Fe and C contamination of the glass. Neglegible amounts were detected.

4.2.2 Second Phase Particles:

The nickel powder was purchased in smooth spherical form from Sherrit-Gordon Limited (OSF 100x150 grade powder). The particle-size-distribution was determined by Green [9] using projected diameter measurements from SEM micrographs (Figure 15a). Chemical analysis and density measurements were also made on these powders (Green [9]).

The aluminum particles (purity > 99.9%) were purchased from Alcan Aluminum Corporation at Berkeley, California (Lot No. SP-276, Grade M.D. x -85) and had a particle size distribution of (-100, +140 mesh). Though the manufacturer stated the particles to be nearly spherical, they were mostly oraloid. Attempts were made to spherodize them by passing them through a carbon arc. This did not improve their shape.

Pure Al_2O_3 particles (purity > 99.9%) were purchased from Fisher Scientific Company with a size distribution (-120, +140 mesh). These particles were not spherical.

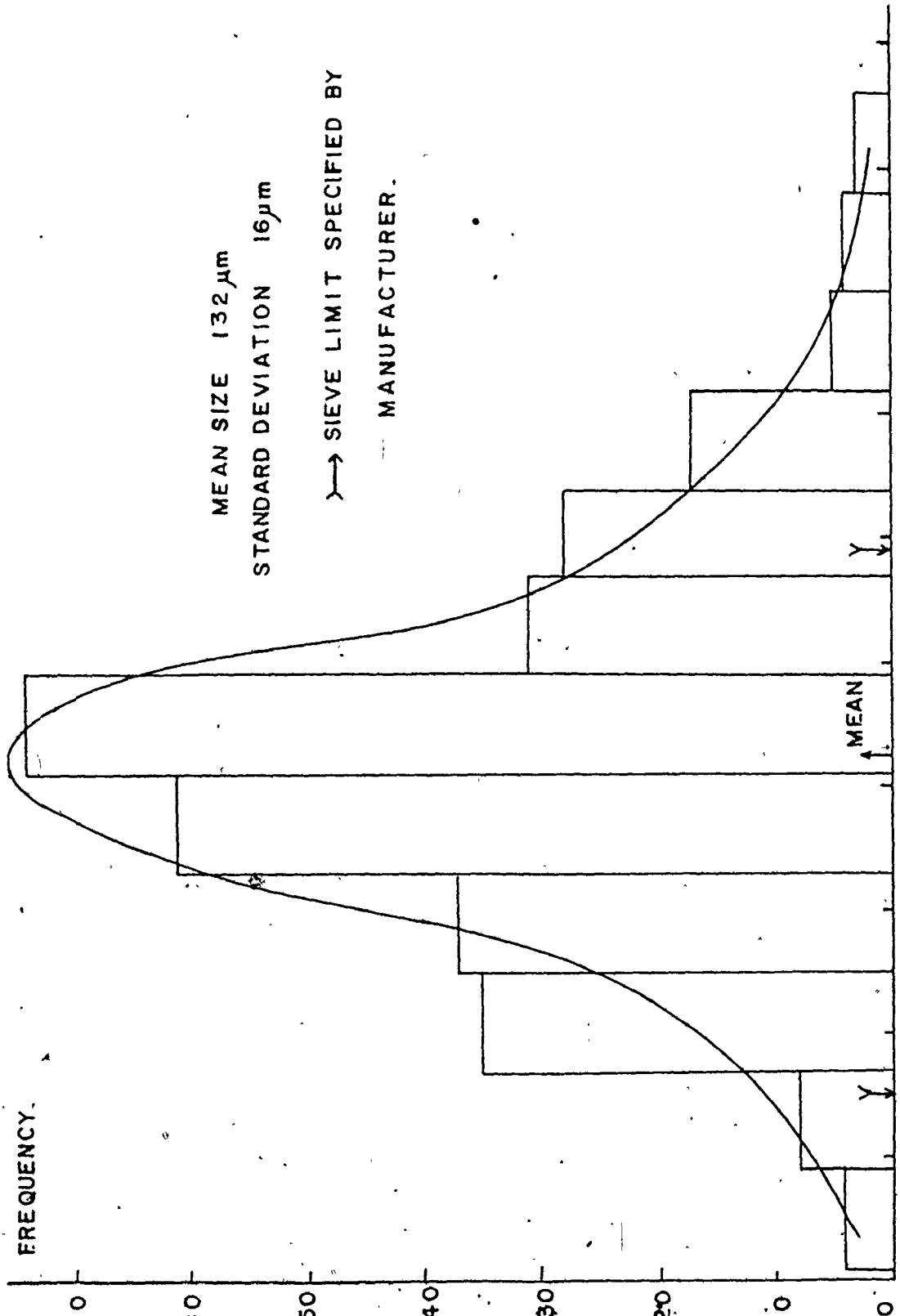

Figure 15(a) Particle size Distribution of As-received Nickel Spheres.

Attempts to spherodize by passing them through a carbon arc in a neutral atmosphere, produced porous Al_2O_3. This is a common problem in producing spherical alumina particles [58]. This porous Al_2O_3 has a low elastic-modulus.

4.2.3 The Oxidation of the Nickel Particles:

Nickel particles were sieved to (-100, +140) mesh and then oxidized 10 grams at a time at 750°C using a wide-bottom alumina crucible. This procedure provides quick maintenance of temperature equilibrium and hence, uniform oxidation. The particles were weighed before and after oxidation to determine the percentage weight gain. The procedure was repeated for all batches and the average weight gain calculated. A plot of average % weight gain versus oxidation time is given in Figure (15b).

Al particles were also oxidized in a similar fashion but in this case, the oxidation time was fixed at three hours and the oxidation temperature at 450°C. An average % weight gain of 0.57% was recorded. The reduced oxidation of the Al particles in comparison with the nickel results from the passive layer of Al_2O_3 which forms on the surface of the particles hindering further oxidation of the Al particles.

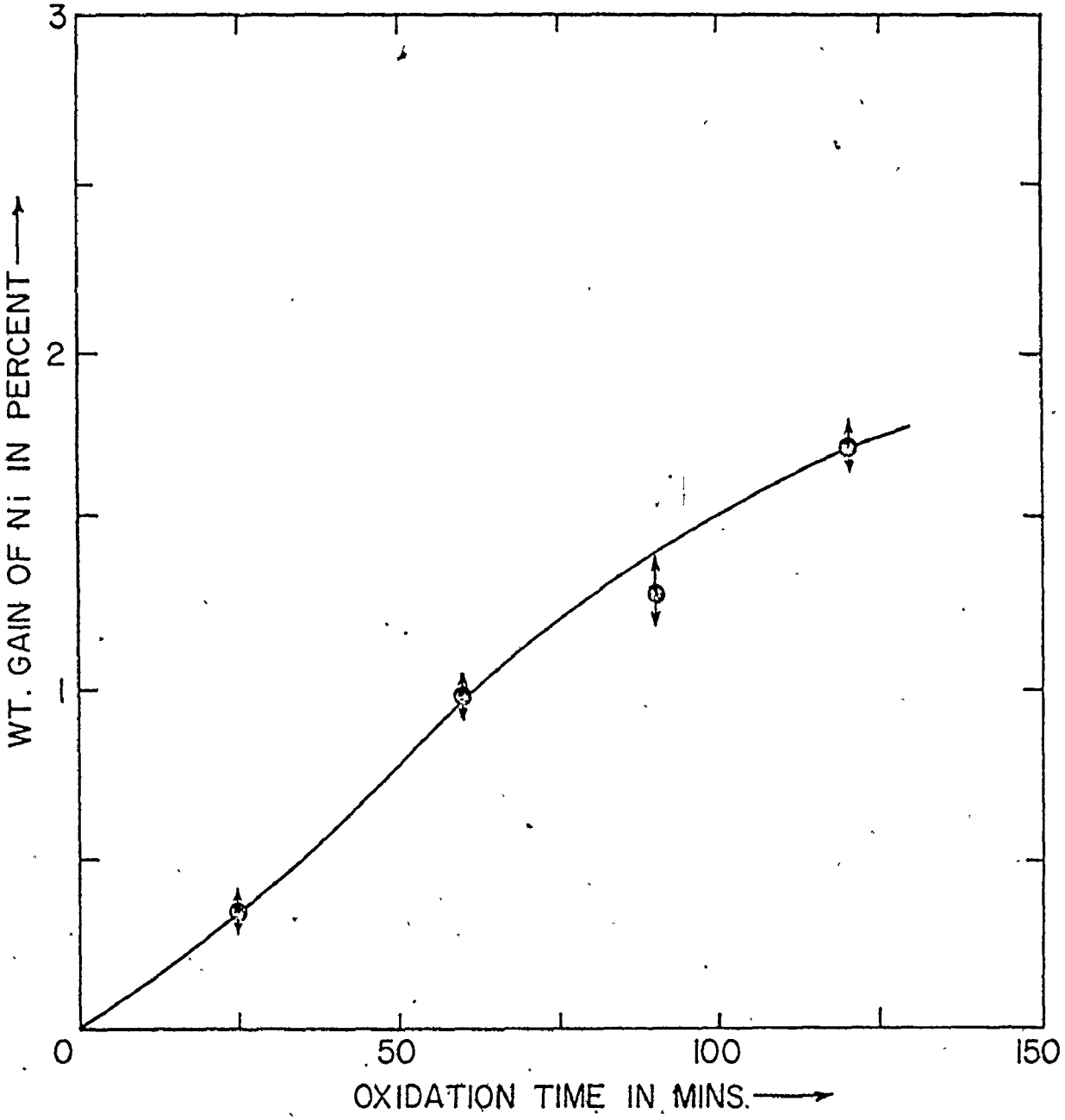

Figure 15(b) Weight gain as a function of oxidation, time for Nickel particles.

4.2.4 Hot Pressing of the Glass Composites:

Appropriate fractions of the glasses and second phase particles were mixed in a glass bottle and rotated for 24 hours. These mixtures were placed in a graphite mold/plunger arrangement and vacuum-hot-pressed to form the composite discs. Figure (16) shows the hot pressing arrangement. The die was positioned between the steel plungers in the vacuum chamber. A Pt - Pt 10% Rh thermo couple was inserted in the mold body (by drilling a small hole at the top of the mold) to measure the temperature and the system was evacuated to less than 0.2 Pa. Induction heating was employed using a 62 mm diameter copper coil attached to a Tocco RF generator. An LVTD attached to the upper plunger was used to indicate the sample shrinkage. The temperature was raised slowly to about 300^{o}C for S glass and D glass composites and then a small pressure of 0.3 MPa was applied. The application of this small load was found helpful in preventing evolution of absorbed gas which gives serious problems in hot pressing glass [9]. The temperature was then raised to 675^{o}C (for S glass and D glass composites) and densification under the small load ceased. The final densification pressure of 8 MPa was applied slowly (to prevent extrusion of viscous glass around the graphite spaces). The pressure was applied for

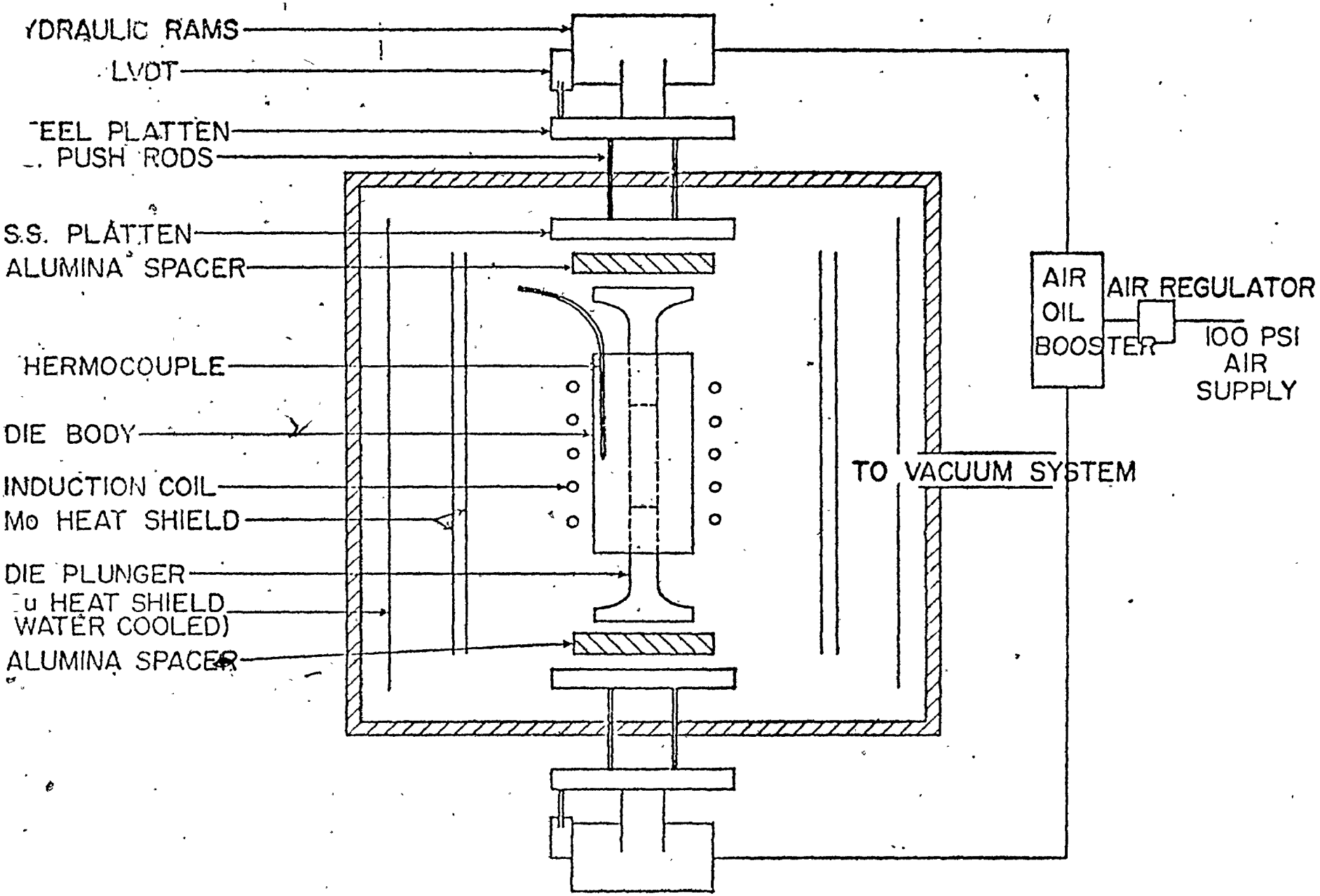

Figure 16 The Hot Pressing Arrangement.

~ 30 minutes to allow final densification. The furnace was then turned off slowly allowing the sample to cool. The slow cool was aided by the high vacuum maintained inside the hot pressing chamber. Usually removal of the hot pressed composite disc without breaking posed a serious problem due to a partial sticking of glassy phase to the graphite mold. This problem was overcome by coating the mold surfaces with a boron nitride lubricant.

The hot pressed samples were annealed at 520^{o}C for four hours to remove residual fabrication stresses. The discs were dark because of graphite contamination of the surface. The inside of the disc had a green tint due to slight iron contamination during the grinding process.

The hot pressing temperature for the M glass composite was 500^{o}C. Here the initial load of 0.8 MPa was applied at ~ 200^{o}C.

The theoretical aspects of hot pressing will not be discussed as this was discussed by Green [9].

4.3 Sample Characterization:

The hot pressed composite discs were characterized with respect to density and microstructural detail. Hot pressed samples less than 95% theoretically dense were rejected.

4.3.1 Density Measurements:

The bulk or apparent density of the samples was measured by the Archimedes water displacement method. A clean dry sample was weighed in air to give its unsaturated weight (W_d). The sample was then placed in a beaker of boiling distilled water to remove untrapped air and fill the open pores. The sample and water were cooled to room-temperature and the saturated weight of the sample was determined. The sample was then suspended in a beaker of distilled water so that it is totally submerged. The weight (W_{ss}) of the submerged and saturated sample was determined and the water temperature noted. The density ρ_L of the water at that temperature was found in a handbook [59]. The bulk density and apparent density were then calculated from;

$$\rho_b = \frac{W_D \rho_L}{W_S - W_{SS}}$$

$$\rho_a = \frac{W_D \rho_L}{W_D - W_{SS}}$$

4.3.2 Microstructural Characterization of Hot Pressed Samples

i) Polished Sections:

Typical polished sections of the hot pressed S glass

partly oxidized Ni systems for oxidation times between 0 and 120 mins in steps of 30 mins, are shown in Figures 17(a, b, c, d, e). The polished sections clearly show that as the oxidation time increased, the oxide layer thickness increased. The extent of bonding with the glassy matrix was assumed to increase accordingly (Figure 13). Figure (18) shows that polished sections of the M glass - Al system. A considerable bond has developed between the glass and the second phase Al. Figure (19) shows a magnified SEM fractograph of the D glass - Al_2O_3 composite. The striking feature of this micrograph is that, apart from good bonding between the glass and Al_2O_3, the latter is highly porous. This reduces the effective elastic modulus of the Al_2O_3 particles considerably.

ii) Quantitive Microscopy:

Since the main objective of this study is to investigate local crack-particle interactions in detail rather than to explore the influence of interparticle spacing and particle size etc. on the fracture toughness, these parameters were not investigated in detail. Only a brief summary of these parameters and contiguity problems in two phase systems is given here; a detailed account of the use of quantative microscopy to determine particle size distribution - interparticle spacing etc. is given elsewhere [9].

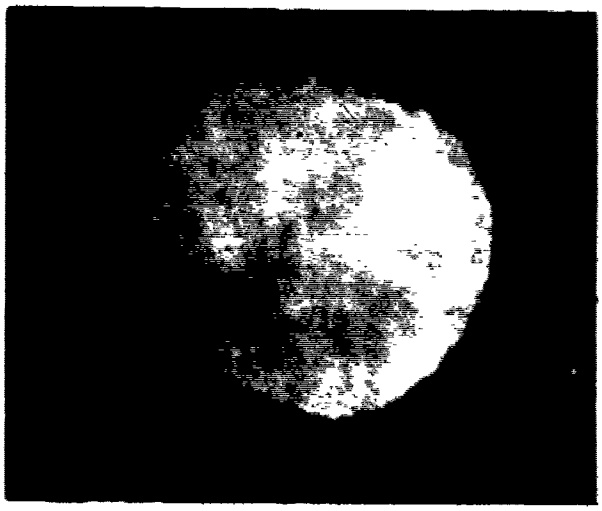

Figure 17(a) Polished section of 0 min. oxidized Nickel particles in Nickel - S glass composite,

Figure 17(b) Polished section of 30 min. oxidized Nickel particles in Nickel - S glass composite,

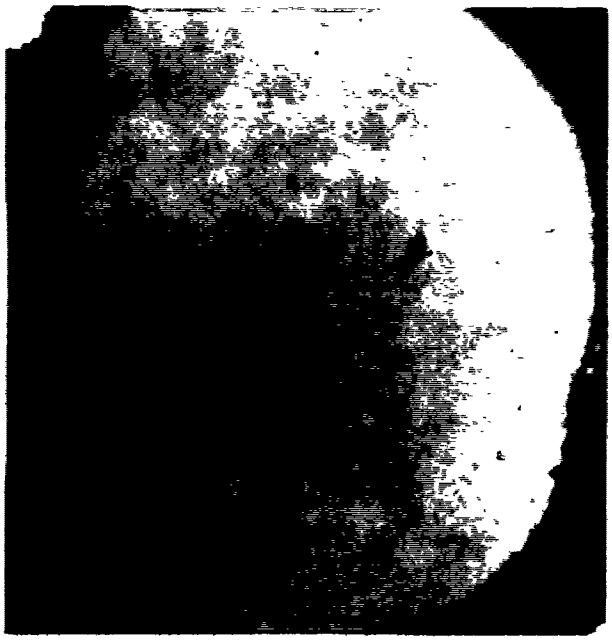

Figure 17(c) Polished section of 60 min. oxidized Nickel particles in Nickel - S glass composite, (X680).

Figure 17(d) Polished section of 90 min. oxidized Nickel particles in Nickel - S glass composite, (X680).

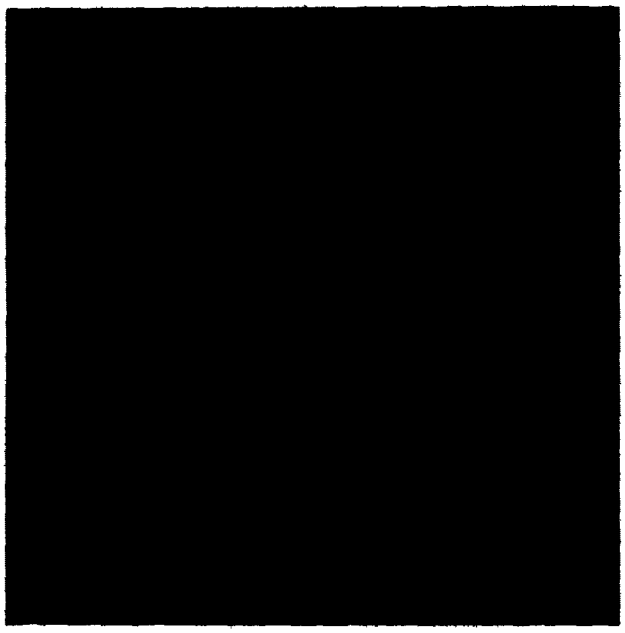

Figure 17(e) Polished section of 120 min. oxidized Nickel particles in Nickel - S glass composite, (X680).

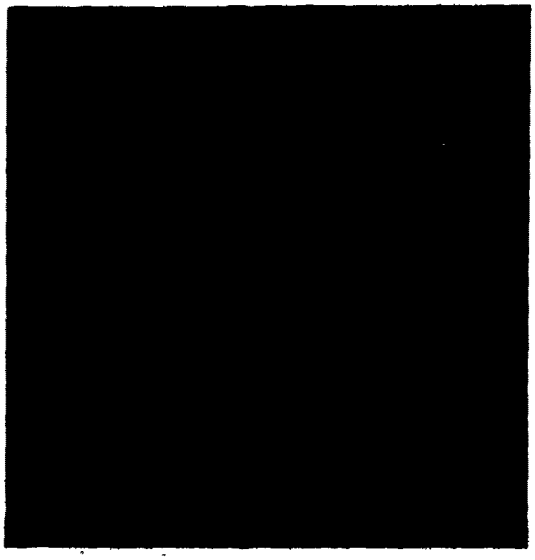

Figure 18 Polished section of 2 hour oxidized Al particles in M glass - Aluminum composite, (X580).

Figure 19 Fracture section of Al_2O_3 particles in D glass - Al_2O_3 composite. Note the parosity in Al_2O_3, (X600).

The interparticle spacing, d, for each volume fraction of a second phase can be determined considering the nearest neighbour distance between two finite size spherical particles using the following expression (after Kocks [67]).

$$d \equiv r\left(\frac{2\pi}{3V_f}\right)^{1/2} - \frac{\pi r}{2} \qquad (39)$$

where r is the radius of the particle and V_f their volume fraction. The second term in Equation (39) accounts for the finite size of the particles. Equation (39) can be rewritten as

$$d \equiv \Delta - \frac{\pi r}{2} \qquad (40)$$

where $\Delta = N_A^{-\frac{1}{2}}$, N_A being the number of intercepts on unit test area determined by quantitive microscopy. From Equation (39) it is clear that d can also be calculated from initial particle size distribution and volume fraction.

Table IV(C) summarizes the particle parameters such as particle diameters D, mean free paths and interparticle spacing, 'd' of glass - nonbonded Ni system calculated and measured respectively before and after fabrication of the composites (see [9]). It is clear that there is a difference between the interparticle spacing d obtained before and after fabrication due to contiguity of particles in the two phase systems; this difference however, is unimportant

V_v	$\bar{D}_o$ (μm)	$\bar{D}$ (μm) *#	λ(μm)**	λ(μm)#	d (μm)**	d(μm)#
0.06	132(±16)	157(±13)	1380	1430	286	291
0.10	"	160(±10)	790	805	198	196
0.15	"	165(±21)	500	536	118	118
0.20	"	167(±13)	350	336	110	90.6

$\bar{D}_o$ is average particle diameter as measured on nickel powder
* assumed distribution of mono-sized spheres
\# from quantimet results
** calculated from $\bar{D}_o$ assuming a random distribution of mono-sized spheres

Table IVC Comparison of Particle Parameters Before and After Fabrication (after [9]).

in the present study which does not consider the influence of interparticle spacing on the fracture mechanical behaviour of the composites. It is also possible to compare particle size distributions before and after fabrication, but this too was not investigated in the present study. The volume fraction of second phase considered here is that calculated from the mixing with glass powders before hot pressing i.e.

$$V' = \frac{W'\rho}{W\rho'} V \qquad (41)$$

where V', W' and ρ' are the volume fraction, weight fraction and density of second phase particles respectively.

4.4 Measurement of Fracture Toughness and Strength:

4.4.1 Measurement of G_{IC} by D.C.B. Method

The D.C.B. testing method discussed in Section 3.3.1 was used in the present study to determine the G_{IC} values of the glass composites. The loading rig used for this study is shown in Figure (20). A counter-balance weight minimizes the effect of sample weight and a hinged lower grip ensures vertical alignment. The top and bottom grips were aligned prior to testing with a template. The load was applied via steel pins inserted into the holes of steel loading tabs glued to the arms of the sample. Ultra-

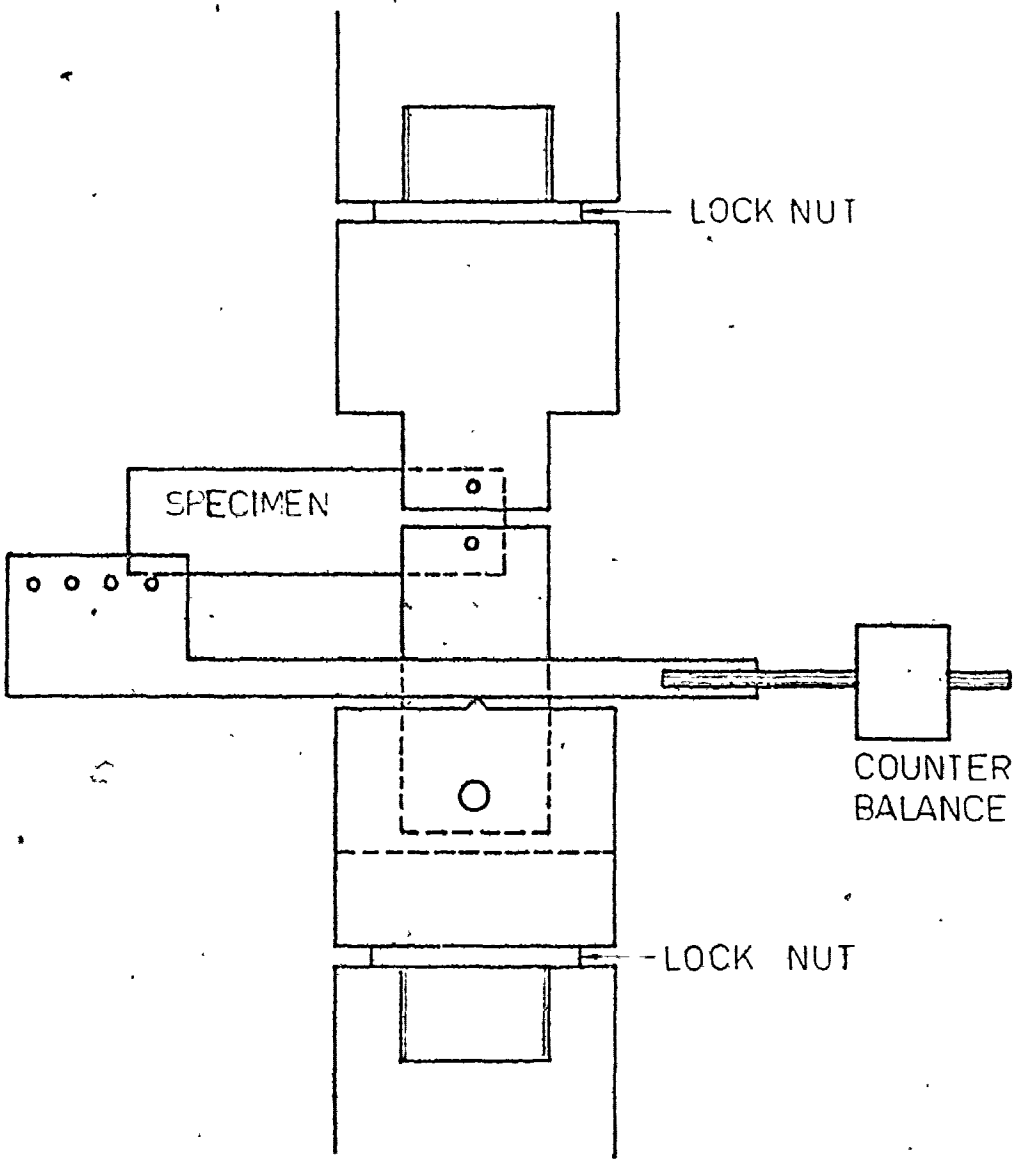

Figure 20 Design for DCB Loading Fixture.

sonic drilling of holes into the specimen arms was avoided because these often result in failure of the brittle composites.

The G_{IC} values were calculated from the following formula [see Section 3.3.1] first suggested by Hoagland et. al. [50] for a side grooved specimen;

$$G_{IC} = \frac{1}{b}\left(\frac{9P_c^4 Y_c^2}{4EI}\right)^{1/3} \qquad (42)$$

where b is the width of the fracture surface in the side grooved DCB specimen, P_c and Y_c are respectively the critical load and critical total deflections of the beam, E the Young's modulus of the composite and I the moment of inertia of the beam about its neutral axis. The deflection Y_c was measured using a transverse strain sensor* with a maximum opening of .020". The load at failure was measured using using a conventional load cell.**

Prior to testing the samples by the DCB method, G_{IC} values for standard Corning 7740 pyrex glass samples were determined. The G_{IC} values for this material are well documented in the literature [60]. The G_{IC} values obtained were within 10 percent of the literature values and considered acceptable. Caré was taken to calibrate the strain gauge for each sample width as the calibration varies

---

* Instron Model #G57-11 * Instron Model #I355CT.

for different sample widths. The errors involved in these measurements are discussed in Appendix II. The respective elastic moduli of the composites were determined from four-point-bend data where the elastic modulus is given by:

$$E = \frac{7P}{32\delta w^3}$$

where P, δ are the load and corresponding deflections of the bond specimen.

4.3.2 Fracture Strength by Four Point Bend Method:

The fracture strength was determined on machined 6mmx10mmx40mm samples using the four point bend method, (discussed in Section 3.3.2) and using the following formula:

$$\sigma_{max} = \frac{3Pxw}{bh^3}$$

To eliminate possible sources of error such as friction forces at the load points, incorrect spacing of load points and unequal distribution of loads and twisting and wedging, a special testing rig (Figure 21) first designed by Hoagland [18] was used on the Instron. For each test point, a minimum of five samples were tested. The load-deflection curves from the four-point-bend tests were used to calculate the E values, as discussed above.

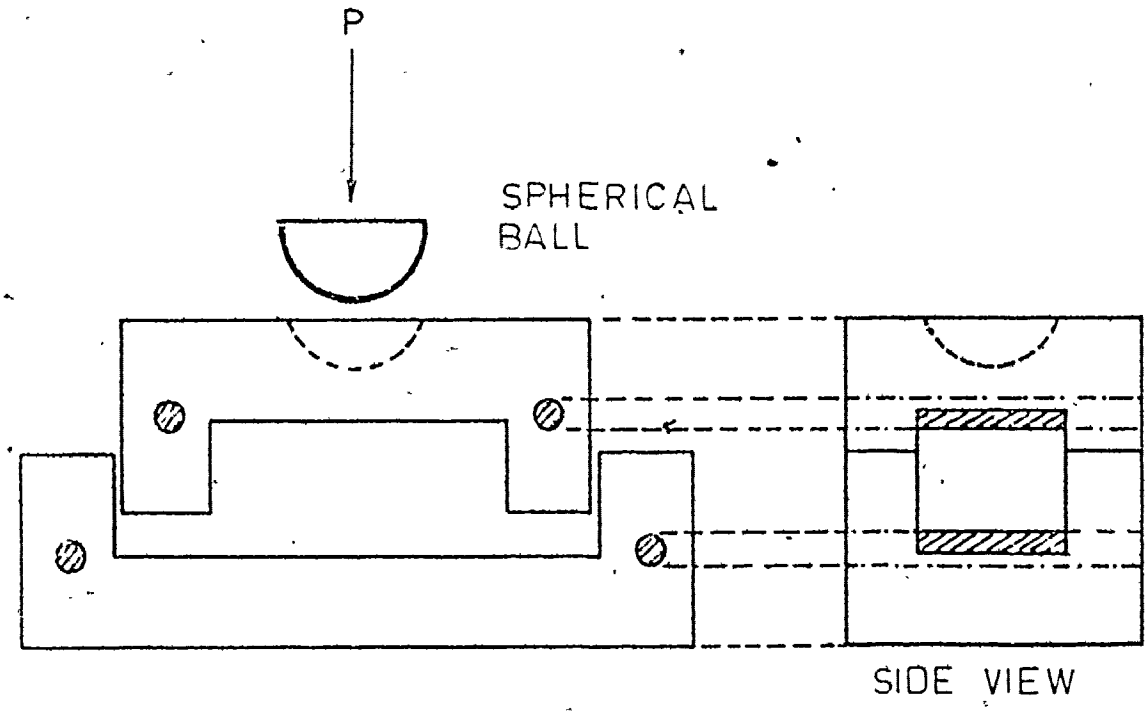

Figure 21 Design for Four Point Bend Strength Testing Rig.

4.5 Ultrasonic Fractography:

The theoretical aspects of the ultrasonic technique were discussed in Section 3.3.3. The experimental set-up is shown in Figure 22 [9] and the components of the quartz transducer used to generate the mechanical shear stress are shown in Figure 23. In order to drive the U.S. transducers, a transmitter of range 100-1000w was used. For glass samples an intensity of 0.1 W/m^2 ~ 0.2 W/mm^2 gave acceptable results, though in detail this depends on the material's properties i.e. elastic constants, ultrasonic attenuation etc. The transducer is water cooled and was cemented to the sample. It is important to maximize the power supply from the transmitter to the transducer and from the transducer to the sample. For this reason, care was taken to keep the thickness of the cement layer between the transducer and sample to as small as possible. In this way the ultrasonic wave is not impeded to any great extent at the boundary between the sample and transducer. Ultrasonic fractography is only applicable to fracture processes that give smooth fracture surfaces and for materials with low acoustic attenuation coefficients.

4.5.2 General Observation of Fracture Surfaces Using SEM

The fracture surfaces of the composite samples were

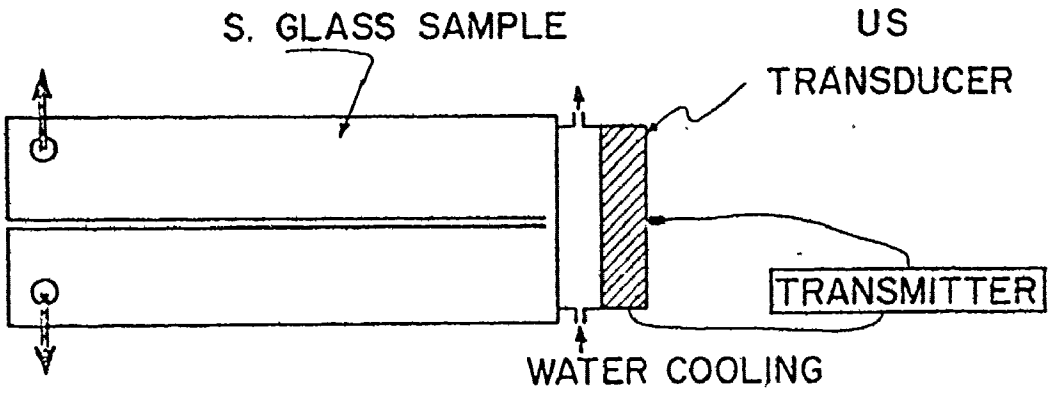

Figure (22) D.C.B. Fracture Test for Ultrasonic Fractography.

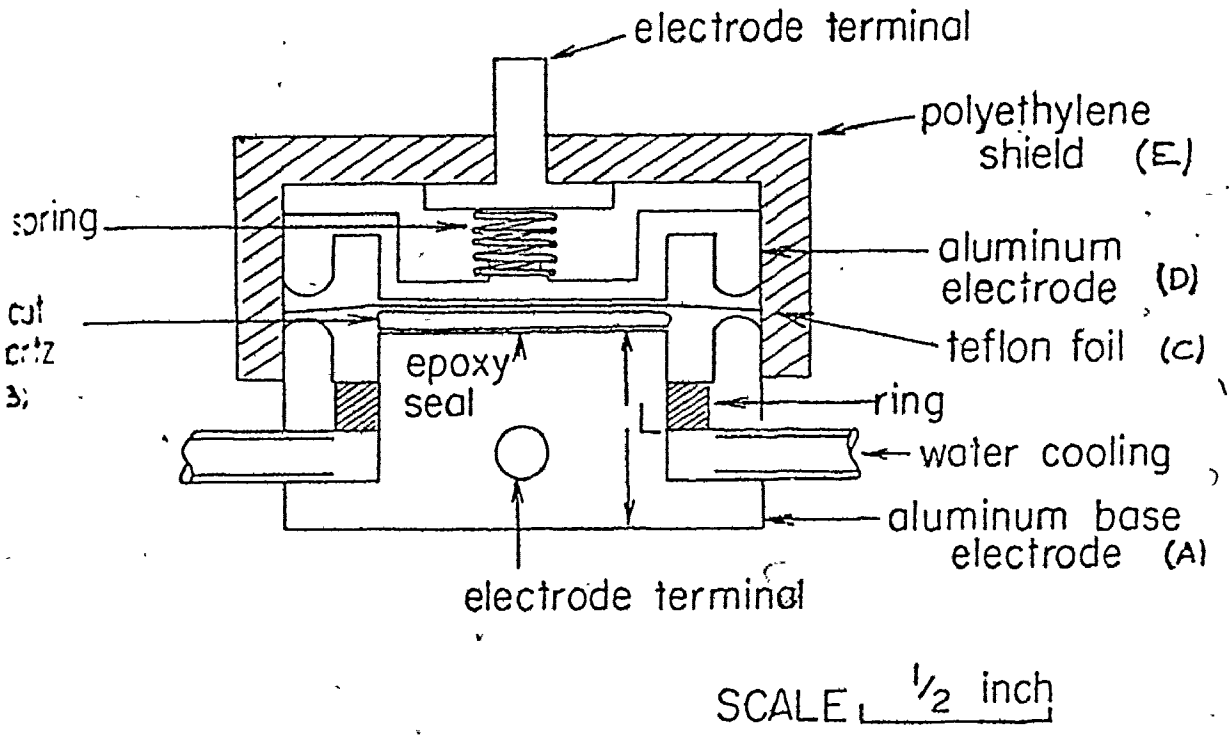

Figure (23) Design for Ultrasonic Transducer.

also studied on the SEM. The samples were coated with a thin film of gold. Some samples were viewed in the optical microscope for evidence of fracture mirrors and other features. The roughness of the fracture surfaces made these observations difficult except at low magnifications. In this case there were no distinct features except those observable in the SEM.

CHAPTER V

RESULTS AND DISCUSSION

1. Results:

5.1 The Fracture Toughness and Strength Results:

5.1.1 Fracture Toughness Results:

The fracture toughness ($G_{IC} = 2\gamma_F$) values of the S glass - nickel composites for varying oxidation times were determined from the DCB load-deflection curves and the results are shown in Figure 24 for a 7% vol fraction dispersion of partially oxidized nickel particles in S glass. Each G_{IC} value represents an average of 4 or 5 measurements. These results show a fracture toughness maximum for the 30 minute oxidized glass-Ni composite. The extent of the interfacial bonding in this case is shown in Figure 17(b) (Chapter IV) which indicates a very thin interfacial bonding 'region' between the Ni particle and glass matrix in comparison with composites of higher oxidation times (for example, see composite with 120 min oxidation time, Figure 17(c)). It is evident from Figure 25 that at the highest oxidation time (120 mins) where the 'region' of interfacial bonding is thickest, the fracture toughness values were slightly lower (even after experimental error) than the case where no

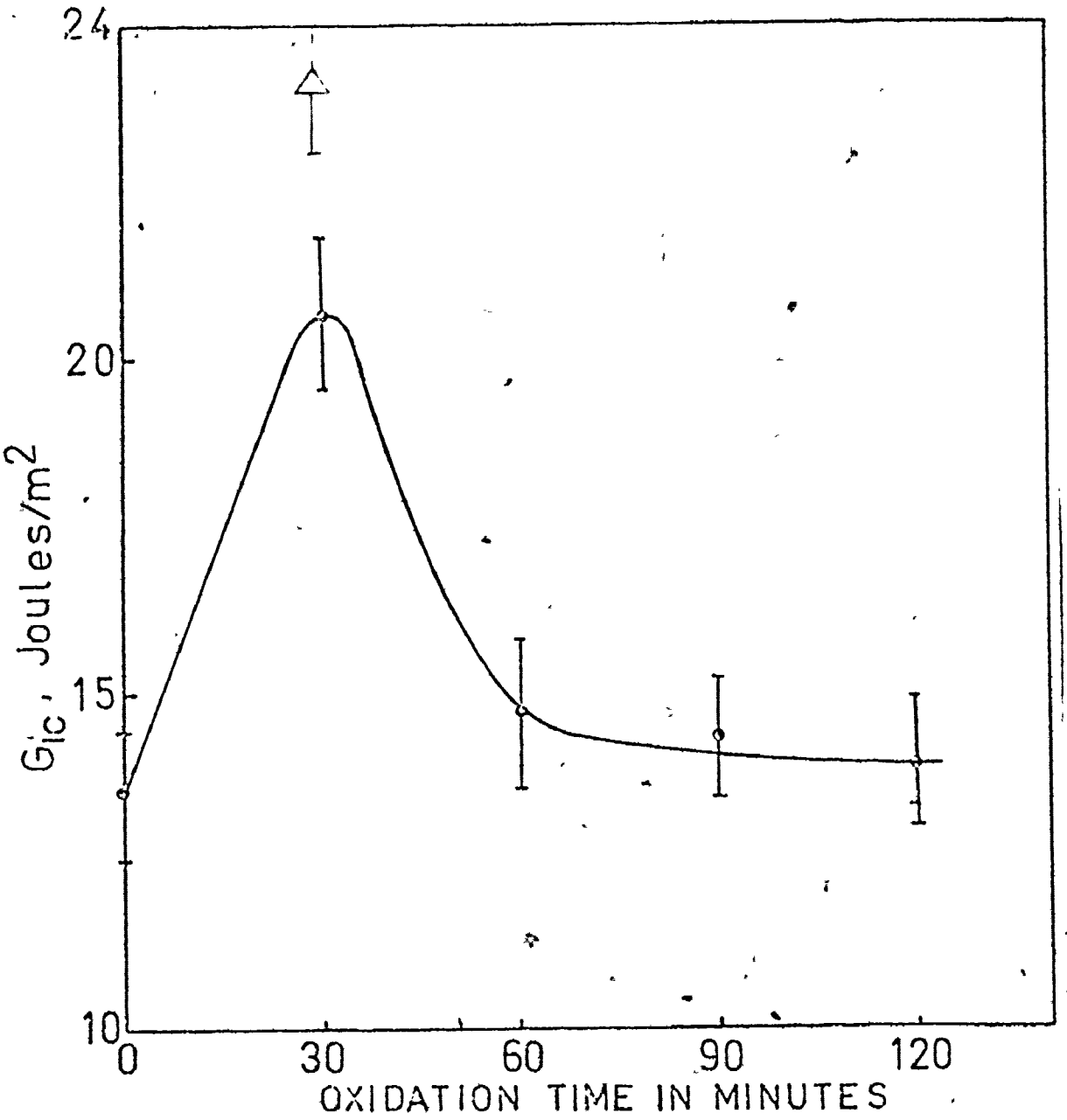

Figure 24 O → Plot of G_{IC} vs. Oxidation time for partially oxidized Ni (vol. fraction = 7%).

Δ → Plot of G_{IC} of 'special particulate composite', (see Chapter 5.2.3).

chemical bonding between glass and nickel exists at all (zero oxidation time). Figure 25 shows the fracture toughness values of the 3.5% vol fraction partially oxidized Ni-S glass composite as a function of oxidation time. A similar peak occurs in the G_{IC} values for the 30 min oxidation time composite. However, in the case of Figure 24 it cannot cannot be said definitely that the G_{IC} values decrease at 120 minutes below the 0 min. value, due to the experimental data scatter. This is thought to result from the small sampling of microstructure made by the crack front at this low volume fraction.

Plots of G_{IC} for glass - aluminum and glass - Al_2O_3 composites as a function of volume-fraction second phase are shown in Figure 26. Also included is a plot of G_{IC} values for the S glass - nickel system for the 30 minute oxidation time. The interesting feature of Figure 26 is the substantial increase of G_{IC} values for the glass - Al composites from about ~ 10 J/m^2 to about ~ 520 J/m^2 for the 20 volume percent composite. In comparison, the S glass - oxidized nickel composites showed an increase from ~ 10 J/m^2 to ~ 60 J/m^2 for the 15% volume fraction dispersion. This is interesting as the inherent toughness of nickel particles is much higher than that of aluminum. These results indicate that the inherent toughness of the

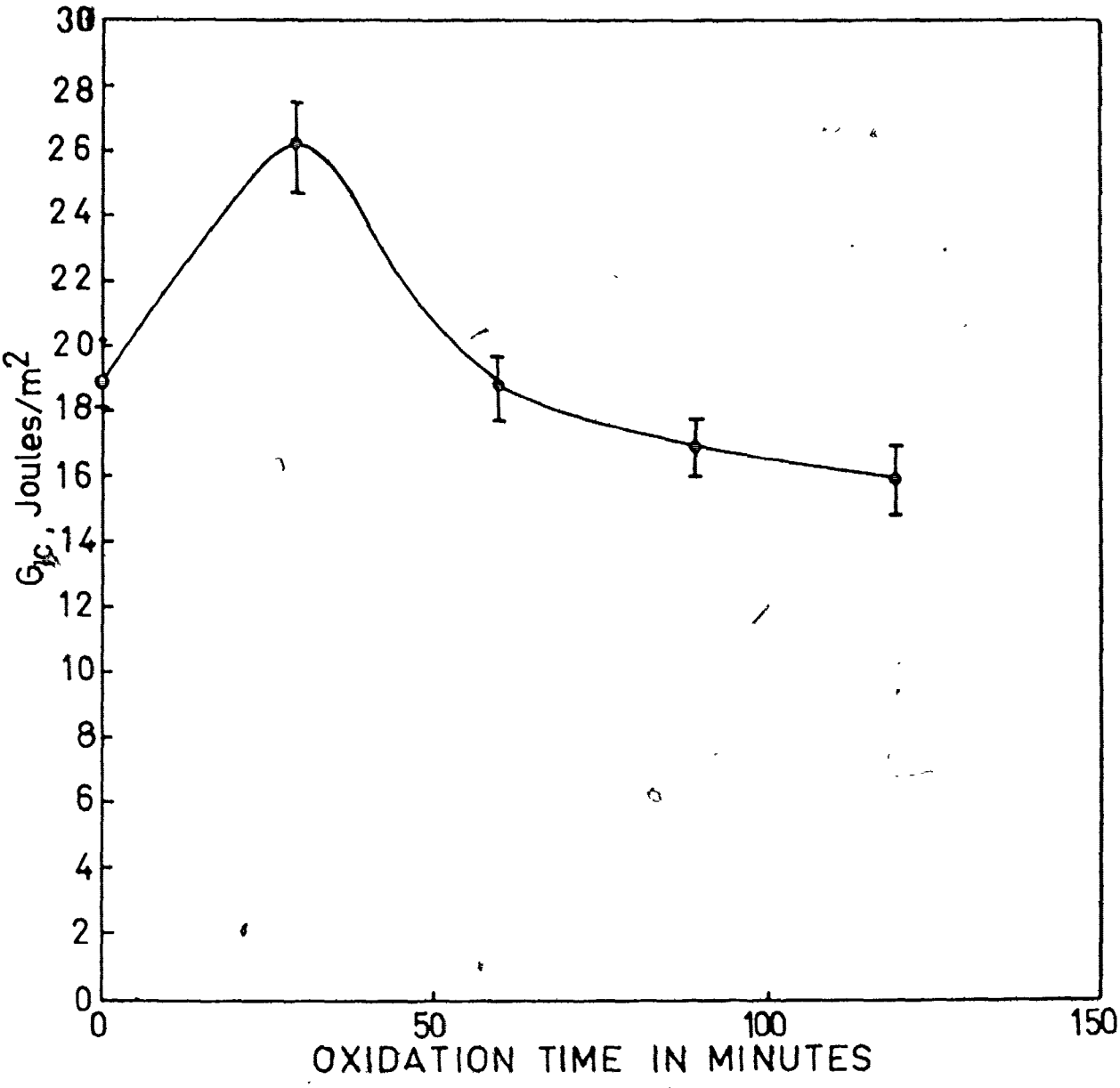

Figure 25 Plot of G_{IC} vs. oxidation time for S glass - partly oxidized Nickel (vol. fraction ~3.5%).

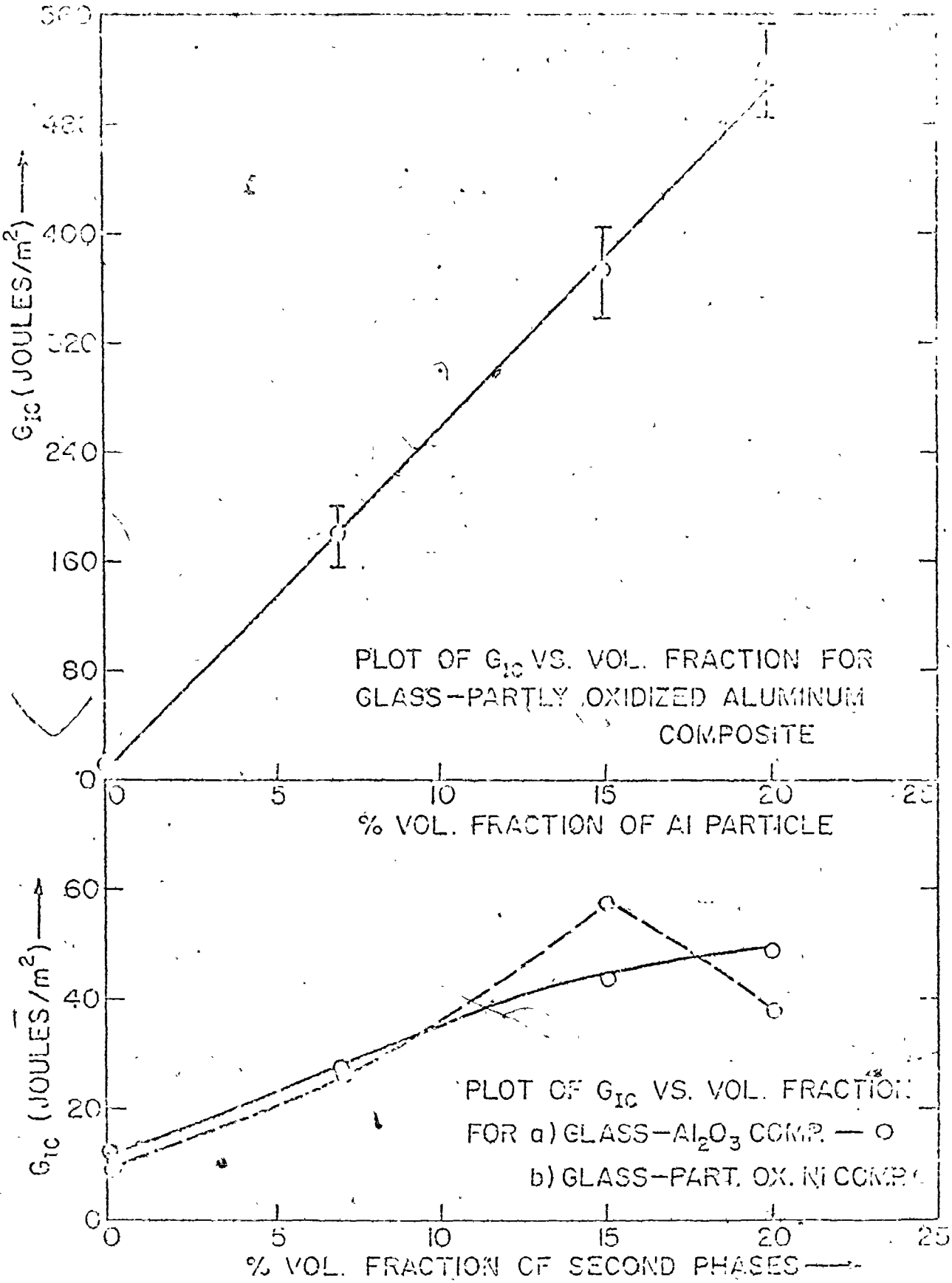

Figure 26 Plot of G_{IC} vs. volume fraction for Composites I, II & III at given oxidation times.

Ni particles could not be utilized whereas that of the aluminum was. General observation of fracture surface features for the S glass - nickel systems and the glass - aluminum systems provides insight into this markedly different behaviour. These results are presented in Section 5.2.1.

The occurrence of maxima in the G_{IC} values of the S glass - nickel system at the 15 vol % (Figure 26) is not new. This maximum fracture toughness at certain volume fraction second phase has been observed in several polymeric composite systems Broutman and Sahu [43] and is generally attributed to the linking of small flaws initiated at individual inclusions to form one single bigger flaw. This ultimately reduces the fracture toughness if the propagating crack follows this new path of least resistance. The exact reason for the maximum is not clear [43].

The graph of fracture toughness for the glass - Al_2O_3 system shows a gradual increase of G_{IC} (Figure 26) up to 20% volume Al_2O_3. The G_{IC} values are consistent with those of Lange [36]. However, since the Al_2O_3 particles were extremely porous (Figure 19), the effect of elastic mismatch between the inclusion and matrix could not be studied. The effective modulus of porous Al_2O_3 particles will not be significantly higher than that of the matrix

and stress concentrations capable of altering the crack path (see Chapter II) might not develop. In this system therefore, crack-particle interactions were not studied in detail. The gradual increase of toughness of this composite may be due to utilization of the toughness of the porous Al_2O_3 particles.

5.1.2 Fracture Strength:

A plot of fracture strength versus oxidation time for the 7 vol % S glass - nickel composite is shown in Figure (27). The values were measured by the four point bend method (Chapter IV) and each point represents the average result of 6 measurements. It is interesting to note that the strength values are lower than the strength values of pure glass when the bonding between the glass and inclusion is weak. This progressively increases towards the pure glass as the oxidation time of the nickel particles increases. This infers that, even when the strongest bond exists between the inclusion and matrix, the nickel particles do not improve the fracture strength of the composite. It could be that flaws were initiated in the matrix in regions of existing stress concentration and propagated through without interacting with the nickel particles. This suggestion is supported by the SEM fracto-

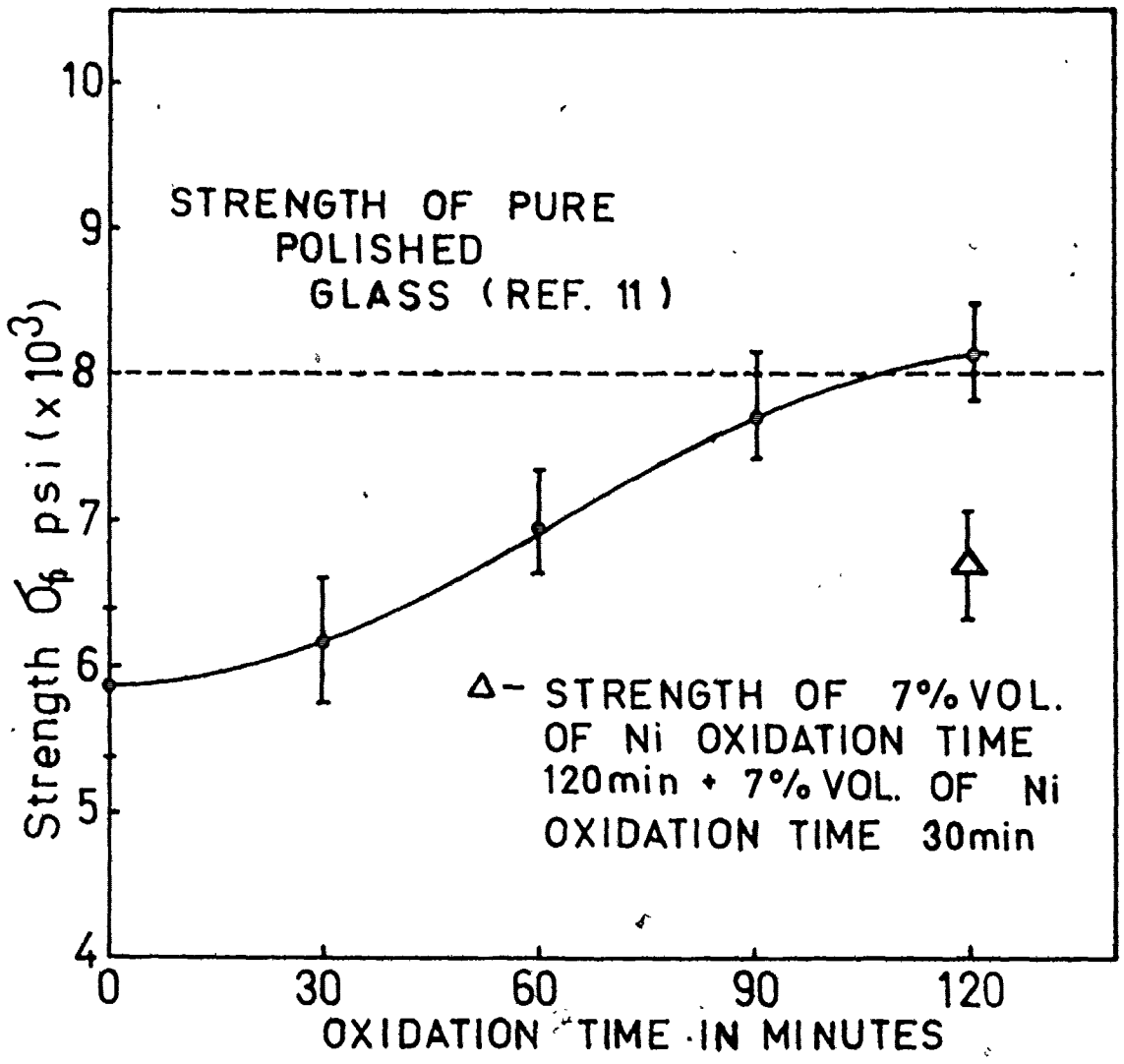

Figure 27 O - Plot of Fracture Strength of S glass - partly oxidized Nickel composite as a function of Oxidation Time.

Δ - Strength Value of 'Special Particulate Composite' (see Chapter 5.2.3).

graph in the next section (5.2).

The lowering of strength values when the bonding between the inclusion and matrix is weak can be attributed to [9] the weak interfacial bond giving rise to flaws in the composite when the load was applied.

5.2 Fractographic Results:

5.2.1 General Observation by SEM:

The fracture surfaces of DCB specimens were coated with a thin film of gold and observed on the SEM. Sometimes the sample was 'tilted' to distinguish the fracture surface features.

Figures (28) and (29) show the fracture surface of a 7 volume % Ni-composite for the cases of the strongest bond (oxidation time ~ 120 min) and the weakest bond (oxidation time ~ 30 minutes). In Figure (28) it can be seen that the crack avoids the nickel particles and passes through the matrix. This is the result of elastic stress concentrations at the particle poles (see Chapter III) resulting from the elastic mismatch between the nickel and glass. Such would alter the crack path. On the other hand, Figure (29) shows a completely decohesed interface. No deformation of the nickel particles occurs in either case. In the second case this means that the stress component

Figure 28 Observed Crack Path in glass - well-bonded Ni/NiO, Composite where effect of Stress Concentration is observed (120 min. oxidation time).

Figure 29 Fracture Surface when bonding between particle and matrix is weak. The stress concentration at poles of the inclusion did not effect crack path.

σ_{yy} at the crack front decoheses the interface before the crack reaches it. The stress concentration at the poles of the inclusion then reverts to its equator on decohesion, securing maximum interaction between the crack and the particle. Figure (29) corresponds to the maximum G_{IC} value (30 min oxidation time) shown in Figure (24). Figure (28) corresponds to the minimum G_{IC} value (120 min oxidation time). SEM fracture surface micrographs of the S glass - nickel composite at 60 min oxidation time are shown in Figures (30) and (31). Of interest here is that, although most of the particles were sufficiently bonded to the matrix to give rise to stress concentrations and alterations of crack path (small humps on the fracture surface), a few particles were insufficiently bonded and decohesed. This process differentiates G_{IC} values for the 60 minute oxidation composites from those of 120 minutes. In the latter case the crack totally avoids the nickel particles (Figure (28)). Figure (32) shows the fracture surface of a special composite of 7 vol % dispersion of 30 min oxidation time Ni particles (optimum bond for toughening) and 7 vol % dispersion of 120 minute-oxidation-time Ni particles (optimum bond for maximum strength) in S glass. A '50-50' mixed mode fracture was noted i.e. some nickel particles are decohesed and others altered the crack path. This mixed fracture mode slightly increased the G_{IC} value over the

Figure 30 SEM micrograph of 60 min. oxidation time Nickel - glass composite (X95) [7% vol. fraction].

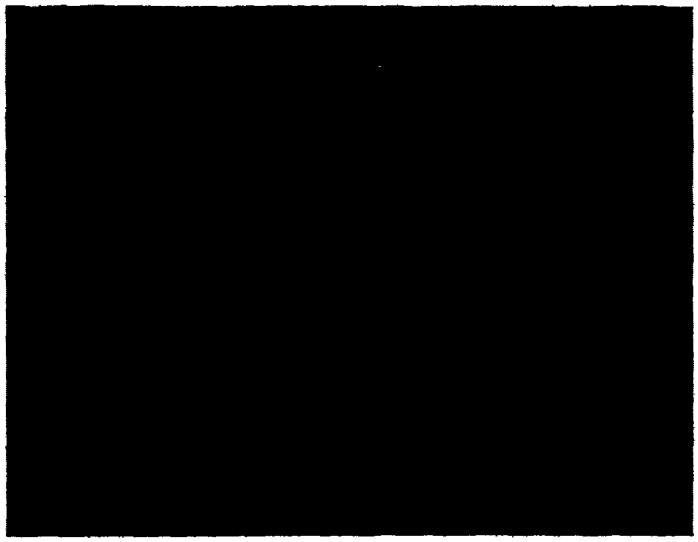

Figure 31 SEM micrograph of 60 min. oxidation time Nickel glass composite (X50) [7% vol. fraction].

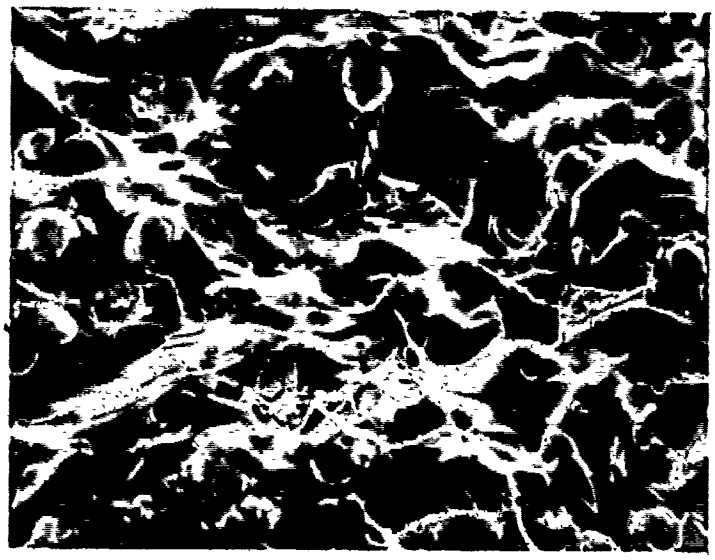

Figure 32(a) Mixed mode of fracture for well-bonded (120 min) and weakly bonded Ni particles (30 min) in the 'special composite' (Chapter 5.2.3) (X50).

Figure 32(b) Fracture surface of the same composite as Figure 32(a) at higher magnification (X95).

maximum value for the 30 minutes oxidation (Figure (24)). This is thought to result from the combined contributions of decohesion of the interfaces (30 min oxidized particles) and increased surface area (120 min oxidized) by crack path alternation. The contribution of the latter is usually small [9]. The strength values of this composite were increased above those of the 120 minute 7 vol % dispersion as shown in Figure (27). This means that though energy dissipating mechanisms contributing to the fracture toughness (G_{IC}) can be linearly combined, this is not the case for the strength values. The introduction of new flaws in the form of decohesed surfaces has significantly reduced the strength of this composite.

The fracture surface of the glass well-bonded aluminum composite is shown in Figures (33) and (34). The interesting feature to note is the large plastic deformation suffered by the particles (Figure 33(a) and 33(b)). The initiation and coalescence of voids in the aluminum particles is evident. Figure (34) shows a tilted view of the fracture surface and the necking of the aluminum particles. This plastic deformation is responsible for the large increase of fracture toughness observed in this case. The interfacial fracture around the deformed particles indicates that, after a certain amount of particle deformation, the interface reaches a critical stress level, causing

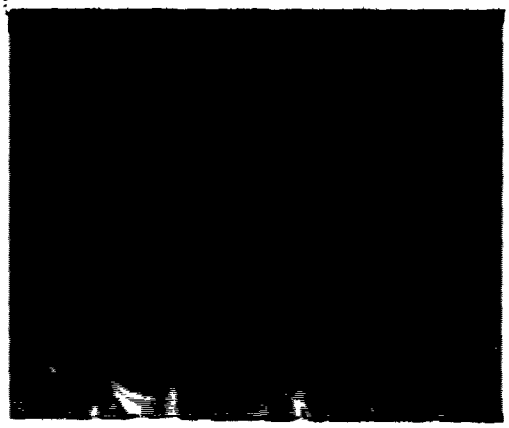

Figure 33(a) Ductile (Al) particle in a glass matrix. Note that in this case $E_i=E_m$. Inherent toughness of (Al) particle is utilized to some extent.

Figure 33(b) Ductile failure of (Al) particles in a glassy matrix. Here $E_i=E_m$ and crack did not avoid the (Al) particles (X500). Note cracking in the interface.

Figure 34 Tilted image of failure of ductile (Al) particles in a glassy matrix (X200).

fracture. This suggests that increasing the interfacial strength by increasing the oxidation time of the aluminum might further enhance the observed toughness by encouraging larger deformation of the aluminum particles. The important point to recognize here is the nonalteration of the crack front path and the lack of a preferred propagation path. This is the result of the absence of elastic stress concentrations in this composite ($G_1 \simeq G_m$).

5.2.2 Ultrasonic Fractographic Results:

The local crack-particle interactions were studied in S glass - partly oxidized nickel composites in which the bonding strength was continuously varied between inclusion and matrix. The technique of ultrasonic fracture surface modulation described in Chapter IV was utilized.

The crack-particle interactions for the 30 min oxidized composite are shown in Figure 35. Note the bowing of the crack front between two nickel particles. As the crack front breaks away from the particle, its local velocity suddenly increases (indicated by increased ripple spacing). This indicates a change of propagation mode. The extent of bowing is higher than for the unbonded composite, [9] as indicated by the maximum angle of bowing (θ_m) at breakaway. The θ_m value was determined as $\sim 25^0$. The

Figure 35 Crack bowing as shown by ripples between two (Ni) particles. Nickel particles were weakly bonded to the matrix (30 min oxidation time).

Figure 36 Crack bowing around weakly bonded Ni particles (30 min oxidation time).

value for the unbonded composite was $\sim 13^{o}$ [9]. This is indicative of a higher crack resistance in the weakly-bonded composite case. Figure (36) shows the crack bowing around a single particle for the 60 minute oxidation composite. A large increase of crack velocity is noted on crack breakaway values. The angle of bowing in this case was $\sim 32^{o}$. This value is larger than the 30 minutes oxidation case. This is because the crack bows more as the interface breaks slowly after initial fracture and reduction of stress concentration. Figure 37 shows the decohesion of the interface and concurrent crack front bowing. Figure 38 shows the crack bowing around Ni particle of 90 min oxidation time, $\theta_m \simeq 38^{o}$. It must be noted however, that for both the 60 min and 90 min oxidation time composites, the crack avoids the majority of particles (see Figures 30 and 31). In the 30 min oxidation time composite, the decohesion of the interface and crack bowing are the main sources of increased crack resistance. A plot of the angle of bowing (θ_m) as a function of the oxidation time is given in Figure 39.

The nature of interaction of the crack front with the inclusion changes completely when the interfacial bonding between the matrix and inclusion is sufficient to resist decohesion by the stress component (σ_{yy}) ahead of the crack tip. In this case, the crack approaches the particle

Figure 37 Crack bowing around a nickel particle intermediately bonded to glass (60 min).

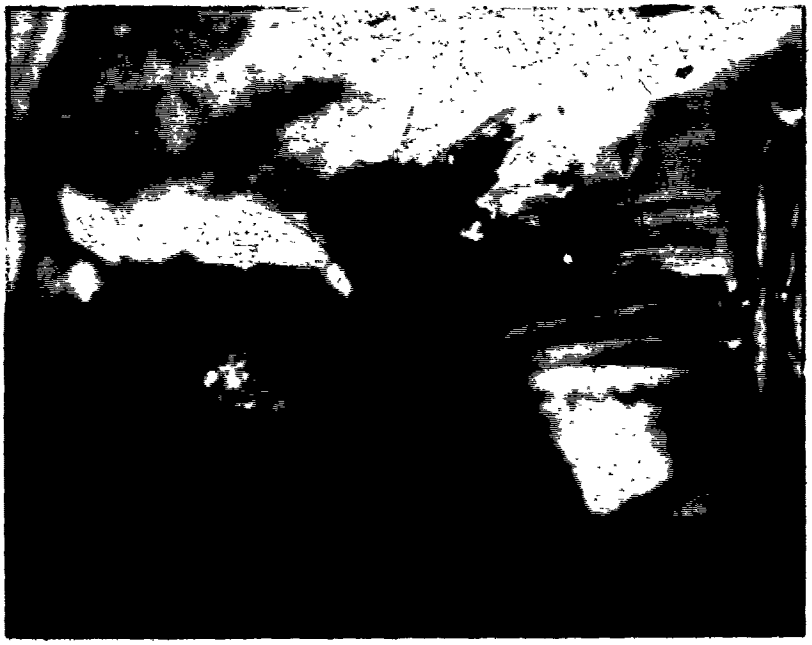

Figure 38 Crack bowing around a nickel particle intermediately bonded to glass (90 min).

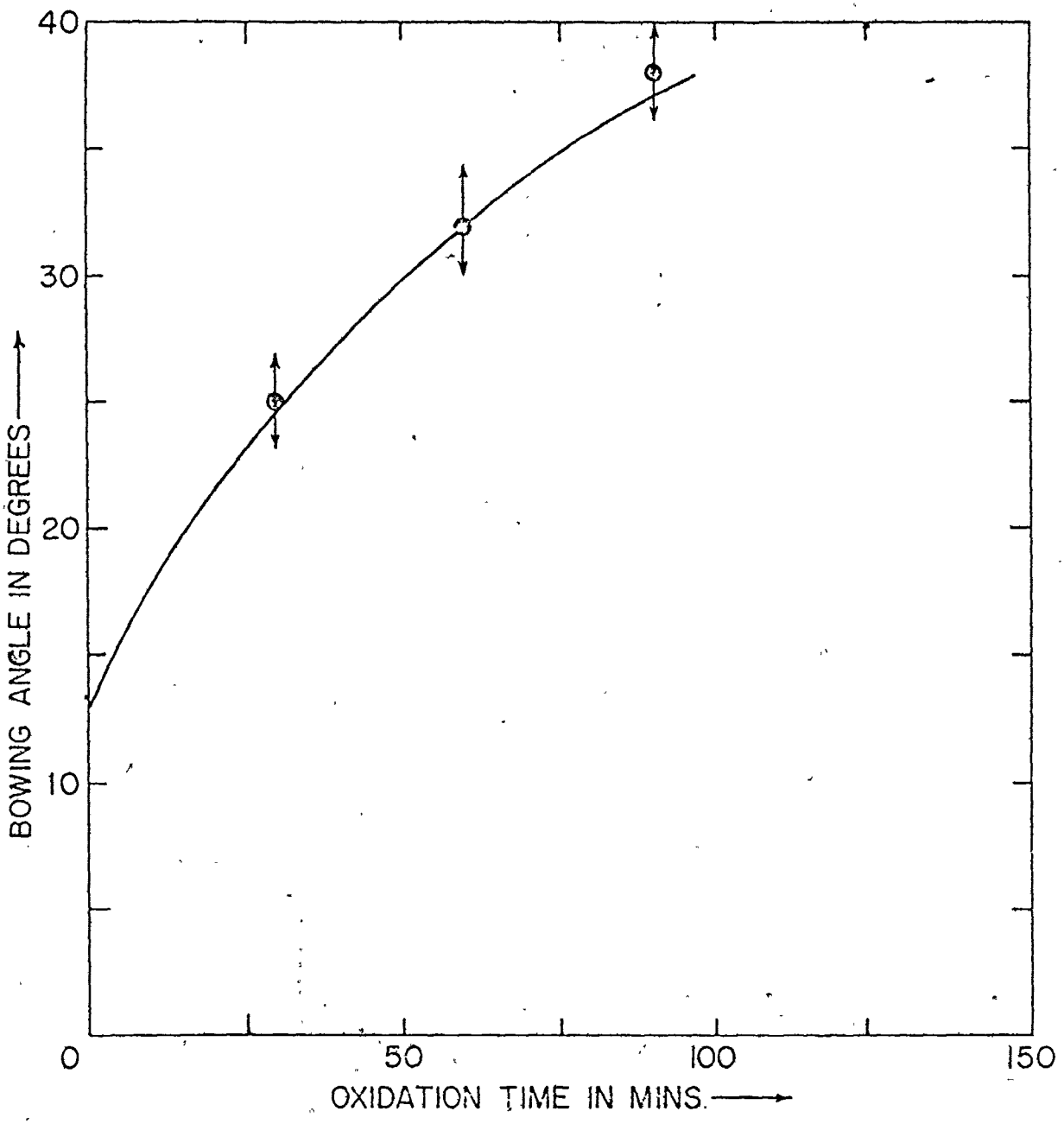

Figure 39 Plot of angle of bowing of crack front versus oxidation time.

and when very near it reacts to the radial stress concentration (σ_{rr}) at the poles of the inclusion so bypassing the inclusion and changing the plane of propagation. This phenomenon is shown if Figures 40, 41 and 42. Figure 40 shows the overall picture when the oxidation time was sufficient to give adequate bonding. Figure 41 shows a close-up view of the crack front near the pole of an inclusion. It is interesting to note the existence of ripple markings on the top of the particles in the glass matrix (Figure 41) and the shape of the ripples indicates that the crack front was virtually uneffected by the well-bonded nickel particle once the crack path altered towards the polar stress concentration. This signifies little interaction between the crack front and particle and hence, an insignificant contribution of this event to the toughening of the composite. The sudden increase of crack velocity under the influence of the polar stress concentration is clearly shown in Figure 42, i.e. the increase in ripple spacing when the crack front is at closest approach to the inclusion. Prior to this, the equatorial compressive stress decelerates the crack as evidenced by the ripple spacing. The change of crack velocity as a function of the apparent distance from the pole of the inclusion (measured from the ripple spacing) and the frequency of the U.S. waves through

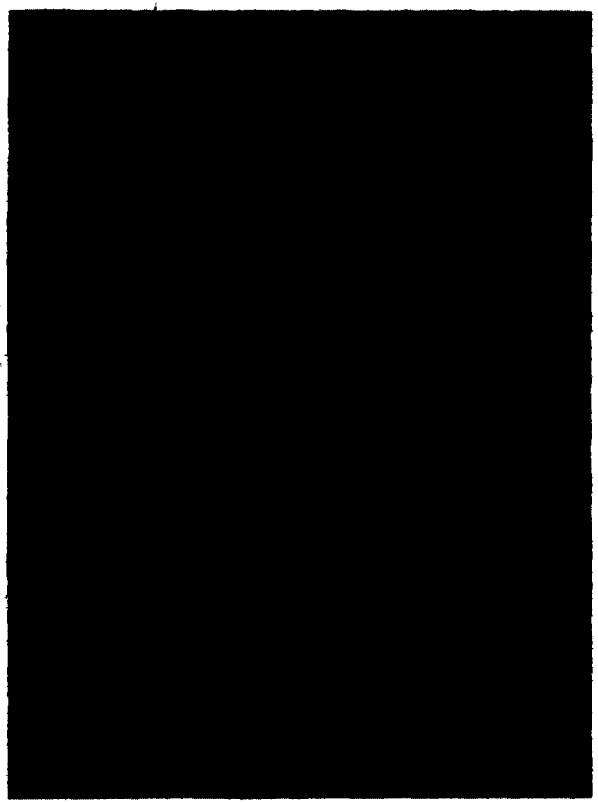

Figure 40 When bonding tetween particle (Ni) and glass was improved, crack avoided the particle, thereby producing no effective interaction (120 min oxidation time).

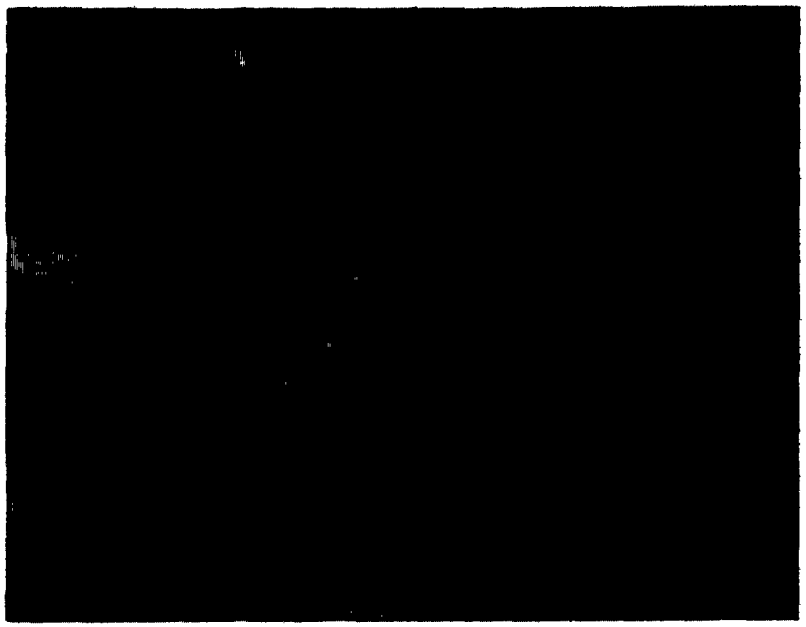

Figure 41 Local crack particle interaction in a glass - well-bonded Ni composite, (by ultrasonic modulation)(120 min).

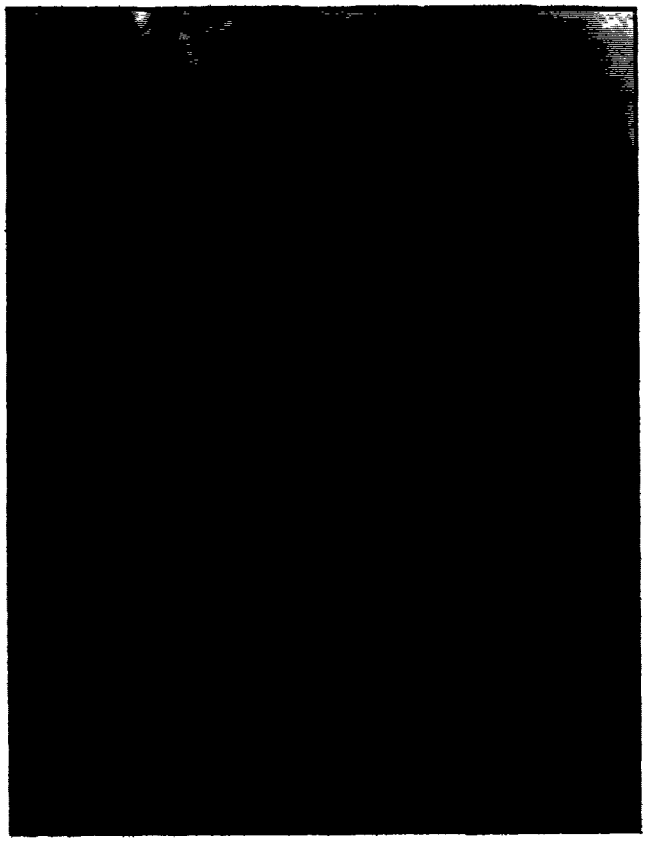

Figure 42 Attraction of crack front towards stress concentration in good bonding case (oxidation time ~120 min).

Equation (40) is plotted in Figure 43. The crack velocity decreases from 6 m/sec to about 0.8 m/sec as it approaches the particle and then suddenly jumps up to ~ 20 m/sec when the crack front is near the inclusion. The decrease of crack velocity on approach can be understood by considering the isostress contours of σ_{rr} and $\sigma_{\theta\theta}$ around the particle (Figures 7 and 8). These show equatorial compressive stress regions around the inclusion, a region where the effective stress is less than the applied stress for the σ_{rr} and $\sigma_{\theta\theta}$ components respectively. This will reduce the local crack driving force K_I as discussed by Khaund et al [47].

5.3 Discussion:

5.3.1 The Effect of Elastic Mismatch on Crack Path and Toughness:

The ultrasonic fractographic evidence of the crack-particle interactions and the general SEM fracture surface features indicate that elastic mismatch has a profound effect on local crack-particle interactions and in fact, may considerably influence the overall toughness of particulate composites. This is effected by directing the crack path. This was the case for the glass/well-bonded Ni composite as the Young's modulus of the Ni particle ~ 3 times that of the matrix glass. According to Equation

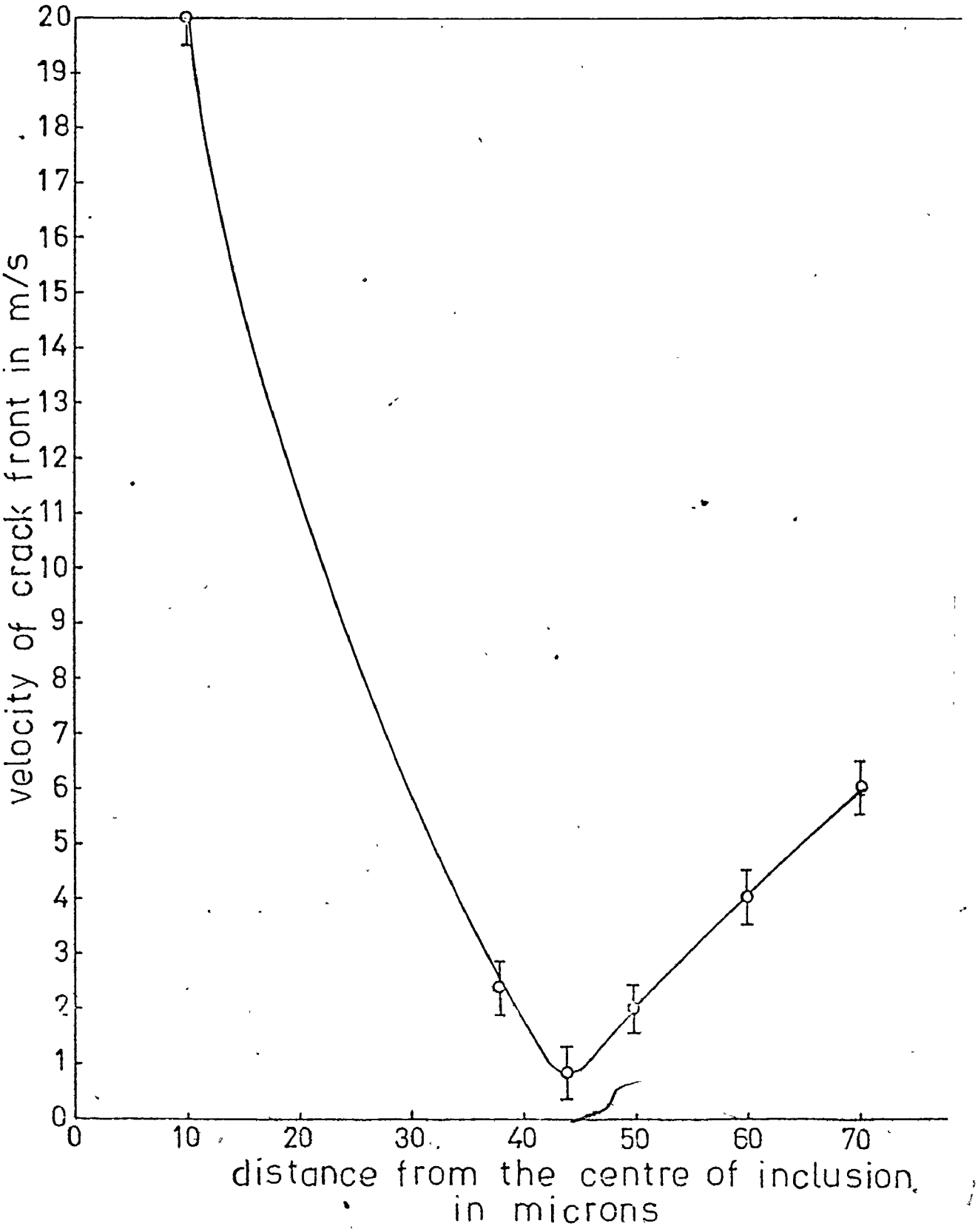

Figure 43 Plot of change of velocity of crack front in near vicinity of inclusion, when crack front approaches inclusion and finally avoids it.

(15), a stress concentration of 1.4 σ_a for the radial component σ_{rr} of the stress field occurs at the poles of the inclusion. The form of the isostress contours are shown in Figures 7 and 8 and it is clear that a crack will experience a retarding stress field as it approaches a well-bonded inclusion. On approaching a pore, however, the situation is entirely different as can be seen from Figure 9. The isostress contours for a pore are such that the crack feels a $\sigma_{\theta\theta}$ component along the equatorial plane of the inclusion ~ $3\sigma_a$ attracting it to the pore. For an inclusion with $G_i >> G_m$, the crack is repelled by the inclusion as it approaches and this will alter its path of propagation. In the latter case the crack avoids the particle totally and their inherent toughness is not utilized. This result is shown in Figure 28 and is reflected in the low fracture toughness values of the glass well-bonded nickel system for 7 vol % Ni (Figure 23). In the case of the glass - well-bonded nickel system, the only additional contribution to the fracture toughness is the increase of fracture surface area due to the alteration of crack path. This is given approximately, for spherical particles by

$$\Delta\gamma_t = \gamma_0 \Delta A = \gamma_0 d.\ \Delta S = \gamma_0 f\, \pi r^2$$

where f is the areal fraction of such particles on the

fracture surface and ΔS is the increase in area of πr^2 and γ_0 is the thermodynamic surface energy/unit area of glass matrix. It is obvious that this will not contribute significantly to the toughening as it is only a fraction of the toughness of the glass matrix.

The situation is different for the glass - aluminum composite. Here, due to the absence of elastic mismatch between the glass and aluminum, (as $E_{glass} \simeq E_{Al}$) no stress concentrations occur around the particles and the crack front is usually left undisturbed on approaching the inclusion In this case the crack meets the second-phase particle and, with a sufficiently strong interfacial bond, plastically deforms the aluminum particles thereby utilizing the toughness of the second phase. This result is of considerable interest as it shows for the first time that ductile dispersions in a brittle matrix do not necessarily increase the toughness of the composite even when the bonding between the inclusion and matrix is adequate. The elastic properties of the inclusions must be such that $G_i \leq G_m$. For $G_i < G_m$ the crack is attracted to the inclusion. Further the extent to which the particle can be deformed for a given interface strength will depend on the relative yield stress of the inclusion (Chapter 2, Equation (14)). As the yield stress of second phase goes down, the extent of plastic deformation at the crack tip will increase.

5.3.2 The Effect of the Interfacial Bond On Local Crack-Particle Interactions

The nature of interfacial bond between the inclusion and matrix has a pronounced effect on local crack-particle interactions and on the overall toughening of the composite. It has been shown that weak interfaces are more effective in improving the fracture toughness of particulate composites (Figure 24) when a positive elastic mismatch exists between the inclusion and matrix. In this case, if the interfacial bonding is strong, the elastic stress concentration deflects the crack front from the particle so eliminating effective local interactions.

When a crack front approaches a weak interface, the normal stress component σ_{yy} in front of the crack decoheses the interface creating a 'pseudopore' in front of the crack. In this case the crack is attracted towards this pseudopore by the increased $\sigma_{\theta\theta}$ components. Once the crack cuts the pseudopore, the section of crack front meeting the pore is locally blunted (see Chapter II) and a higher stress is required for breakaway from this pinning site. This will also contribute to the toughening of the composite and the crack blunting at nonbonded nickel particles was the suggested mechanism responsible for the observed increase of fracture toughness in glass - nonbonded nickel composites by Green [9]. When a weak but bonded interface is present,

there will be an additional contribution via the process of decohesion. Hence the total change in fracture toughness for such composite is composed of two parts i.e.;

$$(\Delta\gamma)_{\text{weak interface}} = (\gamma)_{\text{decohesion}} + (\gamma)_{\substack{\text{shape change because} \\ \text{of blunting}}} \qquad (42)$$

The contribution to $(\Delta\gamma)$ from decohesion can be calculated using Equation (11) in Chapter II which is cited here again:

$$\gamma_{\text{decohesion}} = .84 \frac{K_{IC}^4 a_o}{\pi \sigma_T^3} \left(\frac{V_v}{r^2}\right) \qquad (43)$$

where σ_T is the interfacial bond strength. The form of Equation (42) indicates that provided r and V_v are constant, the contribution from the decohesed zone will be a maximum for the weakest interface. This was found to be true in the present case, though the presence of elastic stress concentrations which may also deflect the crack negate unique proof of the hypothesis. Comparison of G_{IC} values at 30 min oxidation time with those for 0 min oxidation time [9] for 7% vol fraction yields a value of 5 J/m^2 for $\gamma_{\text{decohesion}}$. The value of σ_T, the interfacial strength is difficult to calculate analytically for the case where a chemical bonding exists between the oxide layer of the metal and glass. However an attempt was made by Weirauch [68] to calculate the bonding energy of the glass - metal interface when the

bonding is purely mechanical adhesion (i.e. frictional) and not chemical. His results show that, in the case of purely mechanical bonding between the glass and metal, the bonding energy is given by:

$$E \quad A_C DS \qquad (44)$$

where A_C is the total area of contact between glass and metal, D, the deformation of the metal and S, the yield strength of the metal.

For the glass - Ni interface, substituting characteristic values for D and S, the bonding energy is comparable with the fracture energy of glass ($\simeq 5$ J/m^2) even when the broken area of contact A_C = 25% of the total area. Hence, in case of weak adhesion, even after the crack front stress field partially decoheses the interface, there may be sufficient residual bonding to resist the motion of the propagating crack causing crack bowing and an additional contribution to the fracture energy. This kind of crack particle interaction was observed in Figure 37 where the unbroken part of the interface induced greater bowing of the crack front.

The extent of contribution of the second term in Equation (42) can be discussed in terms of local crack bowing. When a crack front intersects a void, the stress

distribution ahead of the crack is altered. It is experimentally observed that increasing the crack tip radius can increase the apparent value of G_{IC} [65]. Weiss et al [66] have described a useful expression for the reduced stress ahead of such a crack front, i.e.;

$$\sigma_{yy} = \sigma_A \sqrt{\frac{4c}{\rho+4r}} \qquad (44)$$

where r is the radius of the pore, ρ the crack tip radius, c the crack length and σ_A the applied stress. The expression reduces to that for the sharp crack extension for $\rho = 4r$;

$$\sigma_{yy} \quad \sigma_A \sqrt{\frac{c}{2r}}$$

For a crack interacting with a series of voids or decohesed particles, the value of σ_{yy} is locally reduced and this gives rise to a local variation in the fracture resistance. This process is reflected by a change of crack front shape as part of it is locally "hung up" as a result of the reduction of operating stress in that region. This is further reflected by the bowing of the crack front around and between nonbonded or decohesed particles. It is believed that the combination of these two processes in Equation (42) gives rise to the maximum value of G_{IC} for the 30 min oxidation time interface, the

weakest bond interface studied.

The presence of a weak interface is not desirable for improving the toughness of a particulate composite in the absence of elastic mismatch. In this case a high interfacial bonding strength between the inclusion and matrix is preferred so as to utilize the inherent toughness of the second phase. This was found to be the case for the M glass - aluminum composite, where considerable deformation of the aluminum particles occurred before interfacial fracture (Figure 33). The total toughness of the particulate composite with a dispersion of high-toughness second phase with matching elastic moduli can be expressed approximately as:

$$(G_{IC})_{total} = V_m(G_{IC})_m + KV_f(G_{IC})_i \qquad (45)$$

where $(G_{IC})_m$ and $(G_{IC})_i$ are the toughness of the matrix and inclusion and V_m and V_f are their respective volume fractions. The value of the coefficient 'K' depends on the strength of interfacial bond. A 'K' value of unity signifies optimum interfacial bonding. For the glass - aluminum composite, $(G_{IC})_{total} \simeq 520$ J/m^2 at $V_f = 0.2$ (Figure 26) and $(G_{IC})_i \simeq 9000$ J/m^2. This yields a value of $K \simeq 0.3$. This indicates that only partial utilization of the toughness of the Al particles was possible because of the limited bond strength achieved in the 2 hour oxida-

tion of the Al particles. It is believed that higher oxidation times would give higher bond strengths thereby allowing utilization of a higher percentage of the toughness of the Al particles. This conclusion is supported by the cracking of the glass interface around the Al particles as shown in Figure 33(b).

5.3.3 Crack front Bowing and its Contribution To the Toughness:

As discussed in Section 5.2.1, when good bonding exists between the inclusion and matrix, the crack front approaches the inclusion only when the modulus of rigidity $G_I \leq G_m$. Experimental verification of this conclusion is shown in Figure (28) for the glass - Ni composite. However crack bowing around obstacles was observed in the glass - Ni system with weak interfacial bonding. The stress field σ_{yy} ahead of the crack front decoheses the bond creating a pseudopore which attracts the crack front.

In the fracture process when the crack front apprpaches a particle and interacts with it, the following three stages of crack propagation can be delineated;

i) The initial approach of the crack front to the obstacle - the crack shape is influenced by the elastic mismatch between the inclusion and matrix

ii) the bowing of the crack front due to local pinning at the obstacle

iii) the final breakaway from the pinning position.

In considering i), the effect of stress field around inclusion generated due to elastic mismatch on the crack driving force K_I must be considered. In a recent treatment, Khaund et al [47] showed that the change in crack driving force due to presence of an elastic mismatch between a spherical inclusion and matrix, can be expressed in the analytical form:

$$\Delta K \equiv K_I\left(.39A' \frac{r^3}{t^3} + \frac{.78V_m}{1-2V_m} C' \frac{r^3}{t^3} + .820B' \frac{r^5}{t^5}\right)$$

where A', B', C' are coefficients whose values depend entirely on difference of elastic moduli between the matrix and inclusion and 't is the distance of the crack front from the centre of the inclusion. In the case of a pseudopore, A', B' and C' are position coefficients and ΔK is consequently positive, giving rise to an additional driving force which accelerates the crack towards the pore. Such an acceleration causes a crack shape change such as observed in a glass-pore system by Kerkhoff et al [51]. However, the change in 'ΔK' is usually small (- 25%) for the glass - pseudopore system and can be neglected to a first approximation.

Once the crack front reaches the particle, stage (II) starts. Any detailed model to estimate the contribution of the bowing of crack front segments (while it is pinned at the obstacle) to the overall toughening should include the effect of the crack acceleration towards an inclusion (with $G_i < G_m$). The models proposed by Lange [36] and Evans [38] neglect this initial stage of crack propagation. Lange approached the problem of estimating the contribution of the pinning process in terms of the amount of bowing between obstacles, thought to be dependent on the interparticle spacing only (i.e. volume fraction at given obstacle size). The basic assumptions in Lange's model are that the crack front has an unique "line-energy" per unit length and that the critical crack shape at breakaway is semi-circular. These are suspected; the existence of a unique line tension for a crack front is incorrect because the line energy per unit length of a crack front depends critically on its shape and is not a constant. Further, the breakaway crack shape is not semicircular but semielliptical as can be seen in the ultrasonic fractographs (Figures 35 and 36) with different semi-major axes.

Evans [38], using the variation principle, calculated the breakaway shape parameter ('a/2C' where a is the semi-

major axis of the semiellipse at breakaway and 2C is the interparticle spacing) as a function of the ratio of the interparticle spacing to particle size. For a given volume fraction and particle size, the interparticle spacing is defined and consequently the 'breakaway parameter" a/2C can be evaluated. The contribution of the "bowing" process to the fracture energy may be estimated using the following expression;

$$\frac{\gamma}{\gamma_o} \equiv \left(\frac{\sigma_A^E}{\sigma_C}\right)^2 (1 - \nu^2)^{-1} \qquad (46)$$

where $(\frac{\sigma_A^E}{\sigma_C}) \equiv f(a/2C)$, σ_A^E being the stress needed to move the secondary semi-elliptical crack between the obstacles and σ_C, the stress needed to move the primary crack in the absence of the "pinning" sites. The function f can be evaluated numerically. Hence Equation (46) can be written as:

$$\frac{\gamma}{\gamma_o} \equiv F(\frac{a}{2C})(1 - \nu^2)^{-1} \qquad (47)$$

where $F(\frac{a}{2C}) \equiv (\frac{\sigma_A^E}{\sigma_C})^2$

Equation (47) shows that the new value of γ (i.e. the increase in γ_o) depends directly on the depth of the bowed crack front for constant interparticle spacing c (i.e. at a given volume fraction). Hence if the crack front is

obstructed by an obstacle which has an 'impenetrable character' the contribution to γ, the fracture energy, will be a maximum. In the glass/well-bonded-Ni composite, this optimum condition of toughening by crack bowing did not take place since the crack front avoided the particles due to elastic mismatch and propagated entirely through the matrix, (as discussed in 5.2.1). For this case $F(\frac{a}{2C}) = 1$. In the weakly bonded Ni case, the crack front did interact with the pseudopore giving crack-bowing which yields $F(a/2C) > 1$ in Equation (47). This may be the reason for the toughness peak observed in the weakly bonded glass - Ni composite (Figure 24 and Figure 25).

An interesting point to note from Figure 39 is that, even in the strongly bonded composite, a few obstacles (such as shown in Figure 37) had bonding ruptured just enough to avoid the generation of peripheral stress concentrations and so presented a slightly stronger barrier to the crack front due to the partial adherence. The extent of crack bowing in these cases was larger than the 30 min - oxidation case. Though this increased crack bowing will contribute more to the toughening of the composite, the number of such interactions in the well-bonded composite was small, hence the contribution from these isolated cases is not reflected in the fracture toughness versus oxidation-time curves (Figure 24 and 25).

5.3.4 The Special Particulate Composite:

A final special particulate composite was fabricated of S-glass and 7 vol % dispersion of nickel particles of 30 minute oxidation (i.e. interface corresponding to optimum toughness) and 7 vol % nickel particles with 120 minutes oxidation time (corresponding to optimum fracture strength). The idea was to improve both the toughness and strength of the composite. The values of G_{IC} and fracture strength σ_f for this composite is represented as a triangle (Δ) on Figures 24 and 27 respectively. The fracture surface of this composite is shown in Figure 32. It is evident that mixed mode fracture occurred i.e. 'humps' and 'decohesed particles' are evident on the fracture surface. It is interesting to note that the G_{IC} value was slightly higher than that for the 7 vol % dispersion of 30 min particles indicating that an additional contribution to G_{IC} from the additional 7 vol % well-bonded Ni particles. This may be the result of the increase of fracture surface area when the crack avoids these well-bonded particles. However, the strength values were not improved to those of the well-bonded nickel case. This was attributed to the creation of flaws at the weakly bonded interfaces and the consequent reduction of strength irrespective of the presence of the well-bonded particles. It is evident that good bonding of

both dispersants is required if the strength is to be maintained. A mixed dispersion of well-bonded high strength Al_2O_3 particles and well-bonded partially oxidized high-toughness Al particles in a glass matrix could possibly improve both the strength and toughness of a glassy-matrix composite. However the "matching" of the 'α' (thermal expansion coefficient) values for both inclusions with the glass matrix would not be possible and thermal stresses may develop giving rise to flaws around the inclusions. If the 'α' the glass was chosen so that $\alpha_g < \alpha_i$ for both dispersions, compressive stresses would develop in the matrix around the inclusions (Chapter III) so avoiding flaw generation around interfaces.

CHAPTER VI

CONCLUSIONS

From this study of local crack-particle interactions in model particulate composites, following important points can be made:

i) For the toughening of a brittle particulate composite by dispersion of a second phase, the inherent toughness of the second phase must be utilized if significant toughening is to result.

ii) The elastic properties of the inclusion and matrix play an important role in the local crack-particle interactions and greatly influence the overall toughening of the composite. It was found that effective crack - particle interactions take place only when $G_i \leq G_m$ and when the interfacial bonding between the inclusion and matrix is strong. Otherwise the crack path is altered towards the maximum elastic stress-concentration positions, eliminating effective crack-particle interaction and their contribution to the toughening. Elastic mismatch also influences the local crack velocity on approaching an inclusion or pore.

iii) The interfacial bonding plays a dual role in

improving the toughness of particulate composites. When elastic mismatch is absent, stronger interfacial bonding effectively aids the utilization of the inherent toughness of the second phase. This is evident from the results for the glass - well-bonded aluminum composite. On the other hand, when elastic mismatch exists, good interfacial bonding only helps the crack front experience elastic stress concentrations and so alter its path to avoid the particles. In those composites where elastic mismatch was present, an improvement of toughness only results when weak interfacial bonding exists, leading to decohesion and crack-trapping before stress concentrations deflect the crack path.

The present study provides some guidelines for the design of brittle particulate composites of improved toughness by the proper selection of second phase particles.

APPENDIX I

EXAMPLE OF COMPUTER PROGRAMME TO DRAW ISO STRESS CONTOURS

σ_{rr}/σ_0:

```
      PROGRAM TST (INPUT,OUTPUT,TAPE5=INPUT,TAPE6=OUTPUT)
      DIMENSION SIG(50)
      REAL M
      CALL PLOT (2.,5.5,-3)
      CALL LETTER (11,.3,90.0,6.5,-1.35,11HARUP KHAUND)
      CALL DATE(DD)
      CALL LETTER (10,.3,90.0,7.5,-1.5,DD)
      CALL PLOT (14.0,0.0,-3)
      CALL PLOT (0.0,0.0,3)
      CALL PLOT (0.0,1.0,3)
      GNC=3.14159/500.
      TH=0.0
  100 X=SIN(TH)
      Y=COS(TH)
      CALL PLOT (X,Y,2)
      TH=TH+GNC
      IF (TH.LE.2.*3.1+159) GO TO 100
      CALL PLOT (0.0,0.0,3)
      DO 55 I=1,20
   55 READ(5,10) SIG(I)
   10 FORMAT(F10.4)
      I=1
    2 TH=0.0
    3 M=-SIG(I)+.5+.5*COS(2.*TH)
      IF (M.EQ.0.0) GO TO 20
      Z=.214+.712*COS(2.*TH)
      P=-.534*COS(2.*TH)
      A=(Z*Z)-(P*M*4.)
      IF (A.LT.0.0) GO TO 20
      R22=(-Z-(A**.5))/(2.*M)
      IF (R22.LE.1.0) GO TO 20
      R2=R22**.5
      X=R2*SIN(TH)
      Y=R2*COS(TH)
      IF (X.GT.4.0) GO TO 20
      IF (X.LT.-4.0) GO TO 20
      IF (Y.GT.5.0) GO TO 20
      IF (Y.LT.-5.0) GO TO 20
      CALL PLOT (X,Y,3)
   11 TH=TH+GNC
   12 M=-SIG(I)+.5+.5*COS(2.*TH)
      IF (M.EQ.0.0) GO TO 50
      Z=.214+.712*COS(2.*TH)
      P=-.534*COS(2.*TH)
      A=(Z*Z)-(P*M*4.)
      IF (A.LT.0.0) GO TO 50
      R22=(-Z-(A**.5))/(2.*M)
      IF (R22.LE.1.0) GO TO 50
      R2=R22**.5
      X=R2*SIN(TH)
      Y=R2*COS(TH)
      IF (X.GT.4.0) GO TO 50
      IF (X.LE.-4.0) GO TO 50
      IF (Y.GT.5.0) GO TO 50
      IF (Y.LE.-5.0) GO TO 50
      CALL PLOT (X,Y,2)
      IF (TH.LE.2.*3.1+159) GO TO 11
```

```
PROGRAM TST        73/73   OPT=0   TRACE

      CALL PLOT (0.0,0.0,3)
      I=I+1
      IF (I.LE.10) GO TO 2
   15 TH=0.0
   25 M=-SIG(I)+.5+.5*COS(2.*TH)
      IF (M.EQ.0.0) GO TO 60
      Z=.214+.712*COS(2.*TH)
      P=-.534*COS(2.*TH)
      A=(Z*Z)-(P*M*4.)
      IF (A.LT.0.0) GO TO 60
      R11=(-Z+(A**.5))/(2.*M)
      IF (R11.LE.1.0) GO TO 60
      R1=R11**.5
      X=R1*SIN(TH)
      Y=R1*COS(TH)
      IF (X.GT.4.0) GO TO 60
      IF (X.LT.-4.0) GO TO 60
      IF (Y.GT.5.0) GO TO 60
      IF (Y.LT.-5.0) GO TO 60
      CALL PLOT (X,Y,3)
   71 TH=TH+GNC
   75 M=-SIG(I)+.5+.5*COS(2.*TH)
      IF (M.EQ.0.0) GO TO 80
      Z=.214+.712*COS(2.*TH)
      P=-.534*COS(2.*TH)
      A=(Z*Z)-(P*M*4.)
      IF (A.LT.0.0) GO TO 80
      R11=(-Z+(A**.5))/(2.*M)
      IF (R11.LE.1.0) GO TO 80
      R1=R11**.5
      X=R1*SIN(TH)
      Y=R1*COS(TH)
      IF (X.GT.4.0) GO TO 80
      IF (X.LT.-4.0) GO TO 60
      IF (Y.GT.5.0) GO TO 80
      IF (Y.LT.-5.0) GO TO 80
      CALL PLOT (X,Y,2)
      IF (TH.LE.2.*3.14159) GO TO 71
      CALL PLOT (0.0,0.0,3)
      I=I+1
      IF (I.LE.20) GO TO 15
      IF (I.GT.20) GO TO 90
   20 X=SIN(TH)


      Y=COS(TH)
      CALL PLOT (X,Y,3)
      TH=TH+GNC
      IF (TH.LE.2.*3.14159) GO TO 3
      CALL PLOT (0.0,0.0,3)
      I=I+1
      IF (I.LE.10) GO TO 2
      IF (I.GT.10) GO TO 15
   50 X=SIN(TH)
      Y=COS(TH)
      CALL PLOT (X,Y,3)
      TH=TH+GNC
      IF (TH.LE.2.*3.14159) GO TO 3
      CALL PLOT (0.0,0.0,3)
```

```
      I=I+1
      IF (I.LE.10) GO TO 2
      IF (I.GT.10) GO TO 15
60    X=SIN(TH)
      Y=COS(TH)
      CALL PLOT (X,Y,3)
      TH=TH+GNC
      IF (TH.LE.2.*3.14159) GO TO 25
      CALL PLOT (0.0,0.0,3)
      I=I+1
      IF (I.LE.20) GO TO 15
      IF (I.GT.20) GO TO 90
80    X=SIN(TH)
      Y=COS(TH)
      CALL PLOT (X,Y,3)
      TH=TH+GNC
      IF (TH.LE.2.*3.14159) GO TO 25
      CALL PLOT (0.0,0.0,3)
      I=I+1
      IF (I.LE.20) GO TO 15
90    CALL PLOT (0.0,0.0,999)
      STOP
      END
```

APPENDIX II

CALCULATION OF EXPERIMENTAL ERRORS IN MEASUREMENT OF G_{IC} & σ_F

i) Errors in G_{IC}:

From Chapter III (Section 3.3.3)

$$G_{IC} = \frac{1}{b}\left(\frac{9P_c^4Y_c^2}{4EI}\right)^{1/3} = \frac{1}{b}\frac{9^{1/3}P_c^{4/3}Y_c^{2/3}}{4^{1/3}E^{1/3}I^{1/3}}$$

The proportional error in G_{IC} is defined by $\frac{\delta G_{IC}}{G_{IC}}$ and this will be maximum when the individual errors have their maximum expected values and all conspire in the same sense, i.e. when the actual errors are $+\delta P_c$, δY_c, $-\delta b$, $-\delta E$ and δI are maximum. By the help of logarithmic differentiation we get the proportional error e in G_{IC}:

$$e = \left(\frac{\delta G_{IC}}{G_{IC}}\right)_{max} = \frac{4}{3}\frac{\delta P_c}{P_c} + \frac{2}{3}\frac{\delta Y_c}{Y_c} + \frac{\delta b}{b} + \frac{1}{3}\frac{\delta E}{E} + \frac{1}{3}\frac{\delta I}{I} \qquad (A)$$

It is clear that it is extremely necessary to measure P_c and Y_c accurately to minimize the proportional errors in G_{IC}. However, on the contrary a 10% error in measurement of E gives rise to only an error of 3% as seen from Equation (A). Proportional error 'e', when multiplied by 100 becomes percentage error.

If e is the proportional error in single measurements

then the error in the mean of n measurements would be.

$$e' \equiv \frac{e}{\sqrt{n}}$$

ii) Errors in σ_f:

From Chapter IV,

$$\sigma_f \equiv \frac{3P \times w}{bh^3}$$

where x ≡ distance between inner and outer knife edge and is constant.

The proportional error in σ_f is defined by $(\frac{\delta\sigma_f}{\sigma_f})$ and this will be maximum when the individual errors have their maximum expected values. By the help of logarithmic differentiation we get proportional error e in σ_f:

$$e \equiv (\frac{\delta\sigma_f}{\sigma_f})_{max} \quad \frac{\delta P}{P} + \frac{\delta W}{W} + \frac{\delta b}{b} + \frac{3\delta h}{h}$$

Hence accurate measurement of load P and thickness h is necessary to minimize proportional error in σ_f. For n measurements, the error in the mean of n measurements is:

$$e' \equiv \frac{e}{\sqrt{n}}$$

REFERENCES

1. A. A. Griffith, Phil. Trans. Roy. Soc., London, 221A, (1920), p.p. 163.

2. T. K. Gupta, J. Mat. Sci., 2 (1974), p.p. 1585.

3. J. Gluklich, J. Eng. Mech., Proc. ASCE, 89 (1962), p.p. 127.

4. J. N. Goodier, J. Appl. Mech., 1, (1933), p.p. 39.

5. J. Selsing, J. Amer. Ceram. Soc., 44, (1961), p.p. 419.

6. D. P. H. Hasselman and R. M. Fulrath, J.Am. Cer. Soc., Vol. 50, (8), (1967), p.p. 395.

7. F. F. Lange and K. C. Radford, J. Mat. Sc., 6, (1971), p.p. 197.

8. D. Brock, "Elementary Eng. Fracture Mechanics", Nordhoff, Leyden, (1974), The Netherlands.

9. D. J. Green, Ph.D. Thesis (1976), McMaster University, Hamilton, Ontario, Canada.

10. A. G. Evans, A. H. Heuer, D. L. Porter, Fracture 1977, Vol. 1, p.p. 529, ICF4, Waterloo, Ontario, Canada.

11. M. A. Stett, and R. M. Fulrath, J. Am. Ceram. Soc., 53, [1], (1970), p.p. 5.

12. W. Morris and M. E. Fine, J. Am. Ceram. Soc., 59, (1972), p.p. 189.

13. R. W. Davidge and J. J. Green, J. Mater. Sci., 3, (1968), p.p. 620.

14. J. J. Gilmann, J. App. Phys., 35, [3], (1964), 647.

15. W. H. Class and E. S. Machlin, J. Am. Ceram. Soc., 49, (1966), p.p. 306.

16. J. Cook and J. E. Gordon, Proc., Roy. Soc., (London), 282A, (1964), p.p. 508.

17. M. F. Kaplan, Proc. Int., Conf. on Struct. of Concrete, Paper D7, London, (1965).

18. A. R. Rosenfield, G. T. Hahn and R. G. Hoagland, J. Roch. Mech., 5, (1973), p.p. 77.

19. G. M. Bartener, Paper A-25, Ist. Int. Conf. Fracture, Vol. 1, Sendai, Japan, (1965).

20. D. J. Green, P. S. Nicholson and J. D. Embury, in Fracture Mechanics of Ceramics, Vol. 2, ed. R. C. Bradt et. al, Plenum Press, New York (1974).

21. J. A. Kuszyk and R. C. Bradl, J. Am. Ceram. Soc,, 56, [8], (1973), p.p. 420.

22. W. R. Buessem and F. F. Lange, Intreceram., 15, [3], (1966) 229.

23. N. E. Claussen, J. Am. Ceram. Soc., 59 [1-2], (1976), p.p. 49.

24. F. F. Lange and K. A. D. Lambe, Phil. Mag., 18, (1968), p.p. 129.

25. J. P. Berry in Fracture Processes in Polymeric Solids, ed. B. Rosen, P172, Wiley, New York, (1964).

26. E. Orowan, Reps., Prog. Phys. XII, (1948), p.p. 185.

27. P. J. Mallick and L. J. Broutman, Mat. Sc. & Eng., 18, (1975), pp. 63.

28. P. Hing, Proc. Brit. Ceram. Soc., No. 25, (1975), p. 13.

29. C. T. Forwood, Phil. Mag., 17, (1968), pp. 657.

30. A. R. Rosenfield, G. T. Hahn, R. G. Hoagland, J. Roch. Mech., 5, (1973), p.p. 77.

31. K. D. Kingory, "Introduction to Ceramics", Academic Press, New York, (1976), 3rd Edition.

32. R. G. Hoagland, J. D. Embury, D. J. Green, Scripta Metallurgica, Vol. 9, p.p. 907-909, 1975.

33. F. F. Lange, Phil. Mag., 16, (1967), 761.

34. S. M. Ohlberg, H. R. Gelob and C. M. Hallabagh, J. Am. Ceram. Soc., 45, (1962), 61.

35. F. F. Lange, J. Am. Ceram. Soc., Vol. 54, (1971), pp. 614.

36. F. F. Lange, Phil. Mag., 22, (1970), 983.

37. R. B. Thomson, Ann. Rev. Mater. Sci., 3, (1973), 31.

38. A. G. Evans, Phil. Mag., 26, (1979), p.p. 1327.

39. J. F. Knott, "Fracture Mechanics".

40. M. I. Mendelson and M. E. Fine, J. Am. Ceram. Soc., 57, [4], (1974), p.p. 154.

41. P. Hing and G. W. Groves, J. Mat. Sc., Vol. 7, (1972), p.p. 427.

42. F. F. Lange in Fracture Mechanics of Ceramics, Vol. 2, ed. R. C. Brdt et. al, P. 599, Plenum Press, New York, (1974).

43. S. Sahu and L. J. Broutman, Poly. Eng. and Sci., 12, (1972), P. 91.

44. N. I. Muskhelishvilli, "Some Basic Problems of the Mathematical Theory of Elasticity", Norordhoff, Leyden, (1975).

45. O. Tamate, Int. J. Fract. Mech., 4, (1968), p.p. 957.

46. J. Tirosh and A. S. Tetelman, Int. S. Fract. Mech., 12, (1976), p.p. 187.

47. A. K. Khaund, V. D. Krstic, and P. S. Nicholson, J. Mat. Sc., Vol. 12 (1977), p.p. 2269.

48. J. J. Gilmann, J. Appl. Phys., 31, (1966), p.p. 2208.

49. M. F. Kannien, Int. J. Fract., 9, (1), (1973), p.p. 83.

50. R. G. Hoagland, C. W. Marshall and A. R. Rosenfield, Materials Sc. & Eng., 15, (1974), p.p. 51.

51. (a) F. Kerkhof, "Bruchvorgange in Glasern, Deat. Glastech. Ges., Frankfort, A. M., (1970).
(b) F. Kerkhof, Proc. 3rd Int. Congress on High Speed Photography, London, p. 194, (1956).
(c) F. Kerkhof, Int. Conf. on Dynamic Crack Propagation, Leigh University, Bethlehem, (1972).

52. D. J. Green, P. S. Nicholson, and J. D. Embury, J. Mat. Sc., 12, (1977), p.p. 987.

53. A. G. Evans and D. P. Williams, Journal of Testing and Evaluation, Vol. 1, No. 4, (1973), p. 263.

54. D. P. H. Hasselman, D. A. Krohn, R. C. Bradt and J. A. Coppola in Fracture Mechanics of Ceramics, ed. R. C. Bradt, Plenum Press,

New York, (1974).

55. "Chemical Rubber Handbook", on Physical and Chemical Constants.

56. A. G. Evans in Fracture Mechanics of Ceramics, Vol. 1, ed. R. C. Bradt et. al, p. 17, Plenum Press, New York, (1974).

57. S. M. Widerhorn, A. M. Shorb and R. L. Moses, J. Appl. Phys., 39, (1968), p.p. 1572.

58. S. P. Timoshenko, and J. M. Gere, Strength of Materials, Van Nostrand, Reinhold, (1972).

59. B. Cotterell, Int. J. Fract. Mech., 6, [9], (1970), p. 189.

60. S. M. Wiederhorn, J. Am. Ceram. Soc., 52, (1969), p. 99.

61. R. C. Newham, Proc. Brit. Ceram. Soc., No. 25, (1975), p. 281.

62. D. G. Holloway, "The Physical Properties of Glass", Wykeham Science Series, (No. 94), Wykeham Publications, London, (1973).

63. J. E. Blitz, Ultrasonics.

64. R. H. Greaves and H. Wrighton, Practical Microscopical Metallography, p. 177, Chapman & Hall, London, (1971).

65. S. Yukawa and J. G. McMullin, J. Basic. Eng., 83, (1961), p. 877.

66. V. Weiss, ASME Paper No. 62, WA-270, (1962).

67. U. F. Kocks, Acta. Met., 14, (1966), 1629.

68. D. F. Weirauch, Am. Cer. Soc. Bull., Vol. 57, No. 4, (1978), p. 420.